Defect Chemical Investigations of the all-oxide $SrRuO_3|SrTiO_3$ Heterostructure

Von der Fakultät für Mathematik, Informatik und Naturwissenschaften der RWTH Aachen University zur Erlangung des akademischen Grades eines Doktors der Naturwissenschaften genehmigte Dissertation

vorgelegt von

Henning Schraknepper, M.Sc.

aus Braunschweig

Berichter: Privatdozent Dr. R. A. De Souza
Universitätsprofessor Dr. R.-A. Eichel
Universitätsprofessor Dr. U. Simon

Tag der mündlichen Prüfung: 12.08.2015

Abstract

Henning Schraknepper, M.Sc.

The behaviour of point defects in thin, epitaxial films of the oxide electrode $SrRuO_3$ was probed by means of diffusion measurements. Thin-film $SrRuO_3$ was deposited by means of pulsed laser deposition (PLD) on (100) oriented, undoped single crystal $SrTiO_3$ substrates. $^{16}O/^{18}O$ exchange anneals were employed to probe the behavior of oxygen vacancies. Anneals were performed in the temperature range $850 \leq T/\mathrm{K} \leq 1100$ at an oxygen partial pressure of $pO_2 = 500\,\mathrm{mbar}$. Samples were subsequently analyzed by means of Time-of-Flight Secondary Ion Mass Spectrometry (ToF-SIMS). The investigation yields that the measured oxygen isotope penetration profiles as well as the observed diffusion of Ti from the $SrTiO_3$ substrates into the $SrRuO_3$ thin films comprised, surprisingly, two features. A model is proposed — cation sublattice equilibration — that accounts for the appearance of two features in both anion and cation diffusion profiles. Further it is suggested that the observed complex behavior arises from the metastable defect structure of PLD thin films and the unusual defect structure of $SrRuO_3$.

To further investigate the point-defect chemistry in $SrRuO_3$, the metastable state of the thin film's defect structure was deliberately varied. This variation was achieved by depositing $SrRuO_3$ films at different frequencies, ranging from $f = 2\,\mathrm{Hz}$–$18\,\mathrm{Hz}$. Our results reveal that the deposition kinetics is decisively determining the film stoichiometry and the deposition frequency is the key parameter to vary the Sr:Ru ratio. Here the choice of a low deposition frequency results in a suppression of adatom interaction and thus a Sr:Ru ratio of one. The influence of Sr:Ru ratio on several physical properties is discussed. The measured tracer diffusion coefficients show a clear dependence with the Sr:Ru ratio, whereas the corresponding activation-enthalpies neither exhibit a dependence on the cation stoichiometry nor on the strain-state of the film. Conductivity measurements in the temperature range $2 \leq T/\mathrm{K} \leq 300$ on the deposition frequency and thus the Sr:Ru ratio. Further investigation of the conductivity data revealed a decrease in Curie-Temperature and an increase in disorder parameters such as T_{min} with increasing Ru deficiency.

In the here measured tracer diffusion profiles as well as in comparable studies two or sometimes three features can be discerned. In these cases the intriguing questions are: How are the point defects that mediate the diffusion process are distributed and is point defect migration uniform or do fast-diffusion pathways exist? To answer these questions, tracer diffusion profiles for two different cases — namely diffusion through a space-charge layer and fast diffusion along a grain-boundary with coupled bulk diffusion — were simulated and quantitative criteria to distinguish between these two cases were derived. In this context the impact of space-charge layers around dislocation loops was also investigated. Application of the theoretical considerations to experimental data revealed that it is these space-charge layers around dislocation loops depleted of oxygen vacancies that have a blocking effect on oxygen tracer diffusion in the near surface area of $SrTiO_3$ single crystals.

By applying the gained knowledge about the diffusion behaviour in $SrRuO_3$ as well as in $SrTiO_3$, interface potentials can be determined by interpreting oxygen tracer diffusion profiles measured on $SrRuO_3|SrTiO_3$ heterostructure samples. The derived interface potentials are in the order of $\phi_{\mathrm{i}} \approx 0.25\,\mathrm{V}$. A temperature dependent analysis in the range of of the obtained data yields a temperature independent Schottky barrier height of $\Phi^{\mathrm{p}}_{\mathrm{SB}} = 1\,\mathrm{eV}$ as a characteristic quantity describing the $SrRuO_3|SrTiO_3$ interface. This behaviour suggests that the Fermi level E_{f} at the interface is pinned relative to the valence band edge E_{v}. At low temperatures, however, the situation is different. Here interface states are of negligible importance and the Schottky barrier height is stipulated by by the difference in work functions of $SrRuO_3$ and electron affinity of $SrTiO_3$.

Parts of this work have already been published:

H. Schraknepper, C. Bäumer, R. Dittmann and R.A. De Souza *Physical Chemistry Chemical Physics* **17** (2015) 1060-1069

Contents

Nomenclature

Abbreviations

AFM	Atomic Force Microscopy
BHF	buffered hydrofluoric acid
GB	grain boundary
LMA	law of mass action
ORR	oxygen reduction reaction
PI	primary ions
PLD	pulsed laser deposition
RRR	residual resistivity ratio $\rho_{300\,\mathrm{K}}/\rho_{2\,\mathrm{K}}$
RSM	reciprocal space map
SBH	Schottky barrier height
SC	semiconductor
SCL	space charge layer
SI	secondary ions
XRD	X-ray diffraction
XRR	X-ray reflectometry

Symbols

$\alpha^{+/-}$	ionisation probability for positive (+) or negative (-) secondary ions
α_{GB}	grain boundary angle
$\mathrm{Acc}'_{\mathrm{Ti}}$	acceptor ion on a Ti site
a, b, c	lattice parameters of an orthorhombic unit cell
a_{pc}	pseudo cubic lattice constant
β	dimensionless grain boundary parameter
$\mathbf{b}$	Burgers vector
$\boldsymbol{C}$	scalar concentration field of the diffusant

$\boldsymbol{D}$ diffusion tensor (second rank tensor)

ϑ_{dew} dew-point measured in °C

D^{*}_{O} oxygen tracer diffusion coefficient

$d_{\mathrm{s-T}}$ substrate target distance in a PLD chamber

η_X combined transmission efficiency of the SIMS instrument for secondary ions

e' electron

Θ_X isotope abundance of element X

ϵ_0 vacuum permittivity

E_{gap} indirect optical band gap in $SrTiO_3$

ϵ_{r} relative static permittivity

E_{f} Fermi-level

E_{C} conduction band edge

E_{V} valence band edge

$F_{\mathrm{t-s}}$ tip-sample forces in an AFM

t_{G} Goldschmidt tolerance factor

$\mathrm{h}^{\bullet}$ electron hole

h, k, l Miller indices

i_X^{pI} primary ion intensity

i_X^{SI} secondary ion intensity

$\boldsymbol{J}$ diffusion flux

J_{L} laser fluence

k^{*}_{O} oxygen surface exchange coefficient

k_0 k' wave vector of the incident and diffracted X-rays in a diffraction experiment

$K^{\circ}_{\mathrm{Schottky}}$ pre-exponential factor of the temperature dependent defect reaction X

$K_{\mathrm{X}}(T)$ Equilibrium constant of the defect reaction X

k_{B} Boltzmann constant

ΔH_{X} Activation enthalpy of defect reaction X

aO_2 oxygen activity

$\widetilde{\mu}_i$ electrochemical potential of moiety i

μ_i chemical potential of moiety i

N_2O Acceptor dopant of higher valance to be introduced in the binary oxide MO

$n_{^{16}\mathrm{O}}$, $n_{^{17}\mathrm{O}}$, $n_{^{18}\mathrm{O}}$ percentance abundances of the different oxygen isotopes

$M\mathrm{O}$ binary oxide, with Mbeing a metal

χ_{SC} electron affinity of a semiconductor

ϕ electrical potential

$\Phi_{\mathrm{SB}}^{\mathrm{p}}$ Schottky barrier height for a p-type semiconductor

ϕ_{CNL} charge neutrality level of electronic states above the valence band edge on a semiconductor surface or at an interface

Φ_M workfunction of the metal M

$p\mathrm{O}_2$ oxygen partial pressure

Q vector of momentum transfer

ϕ_i interface potential

$\rho(x)$ charge carrier density

R_X Ionic radius of species X according to Shannon

$\mathbf{s}$ vector of the dislocation line

S slope parameter, a measure of the metal workfunction's influence on the SBH

Θ angle of incidence of X-rays onto a sample

T absolute temperature

T_{C} Schottky equilibrium constant

t_{ex} exchange time; the time a sample is exposed to the $^{18}\mathrm{O}_2$-gas)

t_{pre} pre-anneal time

T_{S} substrate temperature

$\mathrm{V}_{\mathrm{Ti}}^{''''}$ Ti vacancy

$\mathrm{V}_{\mathrm{Sr}}^{''}$ doubly charged strontium vacancy

$\mathrm{V}_{\mathrm{O}}^{\bullet\bullet}$ doubly charged oxygen vacancy

ω, ϕ, ψ axis of sample rotation in an XRD instrument

Y sputter yield

Chapter 1

Introduction

One of the grand challenges of the 21st century is the development of devices for data storage and processing that exceed the physical limits of conventional silicon based technology regarding size, power consumption and costs.

Up to today, the success of the material silicon in information technology has been fueled by the continuous advancement in engineering regarding the device size as well as the reduction of defect density.[1] It is this philosophy that soon reaches its fundamental physical limits.[2–4]

In order to overcome these limits, efforts are being made into exploring numerous different physical phenomena and design concepts regarding their potential as successors of silicon-based information technology.[5] One promising way is to employ defects as the functional unit to process and store data with.[6]

A class of materials this concept works particularly well with are perovskite oxides.[7,8] It has, for example, been shown that information can be stored in nanoscale filaments in $SrTiO_3$.[9]

In order to access and process the data stored in $SrTiO_3$, one needs, much like in conventional semiconductor technology, electrodes and interconnects. One of the materials that could serve this purpose is $SrRuO_3$.

Its chemical stability, low lattice mismatch with other perovskite oxides make it ideally suited for this purpose.[10] But $SrRuO_3$ cannot only be used for peripheral purposes, it can also serve as a functional unit to process and store data with.[11,12]

In order to exploit the full potential of potential devices employing $SrRuO_3$ as either a functional of peripheral material, a detailed understanding of the different defects occurring in $SrRuO_3$ is mandatory. Particularly if these defects are used as the functional unit. In the case of $SrRuO_3$, however, investigation of defects has hitherto received little attention.

The systematic study of imperfections in the solid state is conducted within the framework of defect-chemistry, a field established by Frenkel, Wagner and Schottky.[13,14] In this work the framework of defect-chemistry will provide a guideline for the investigation of some aspects of the defect behaviour in $SrRuO_3$. The bulk part of this work is devoted to studying diffusion, a process that is mediated by defects. A thorough analysis of the diffusion behaviour will enable the identification of the relevant defects and their influence on the properties of $SrRuO_3$. Furthermore the unique behaviour of defects at interfaces will be studied. Throughout this work thin film samples serve as model systems to investigate diffusion.

Thin film samples will be studied, not only because they are easier to fabricate in suitable geometries for diffusion experiments than single crystals, but also, and more importantly, because of the relevance of thin films in all-oxide electronic devices.[15]
In the first part of this work, the theoretical (Chapter 2) as well as the experimental background (Chapter 3) needed in this work, is introduced. In Chapter 4, the focus will be on investigating the diffusion behaviour in thin film $SrRuO_3$. Based on the here derived understanding, Chapter 5 will deal with how the sample preparation method pulsed laser deposition can be used to influence the defect chemistry of the prepared films. Theoretical considerations regarding the reliable investigation of the diffusion behaviour in complex heterostructures will be presented in Chapter 6. Here it will be shown how one can reliably discriminate between competing models of describing experimental diffusion data. Lastly (Chapter 7) results regarding the interface, particularly interface potentials existing between an $SrRuO_3$ film and the $SrTiO_3$ substrate will be discussed.

Bibliography

[1] G. E. Moore, *Electronics*, 1965, 114–117.
[2] M. Schulz, *Nature*, 1999, **399**, 729–730.
[3] K. Kim, Electron Devices Meeting (IEDM), 2010 IEEE International, 2010, pp. 1.1.1–1.1.9.
[4] M. Ieong, B. Doris, J. Kedzierski, K. Rim and M. Yang, *Science*, 2004, **306**, 2057–2060.
[5] R. Waser, *Nanoelectronics and information technology*, John Wiley & Sons, 2012.
[6] R. Waser, R. Dittmann, M. Salinga and M. Wuttig, *Solid-State Electron.*, 2010, **54**, 830 – 840.
[7] R. Waser, R. Dittmann, G. Staikov and K. Szot, *Adv. Mater.*, 2009, **21**, 2632–2663.
[8] P. Zubko, S. Gariglio, M. Gabay, P. Ghosez and J.-M. Triscone, *Annu. Rev. Condens. Matter Phys.*, 2011, **2**, 141–165.
[9] K. Szot, W. Speier, G. Bihlmayer and R. Waser, *Nat. Mater.*, 2006, **5**, 312–320.
[10] G. Koster, L. Klein, W. Siemons, G. Rijnders, J. S. Dodge, C.-B. Eom, D. H. A. Blank and M. R. Beasley, *Rev. Mod. Phys.*, 2012, **84**, 253–298.
[11] G. Herranz, B. Martinez, J. Fontcuberta, F. Sanchez, M. V. Garcia-Cuenca, C. Ferrater and M. Varela, *J. Appl. Phys.*, 2003, **93**, 8035–8037.
[12] E. Tsymbal, A. Gruverman, V. Garcia, M. Bibes and A. Bartholemy, *MRS Bulletin*, 2012, **37**, 138–143.
[13] J. Frenkel, *Z. Phys.*, 1926, **35**, 652–669.
[14] C. Wagner and W. Schottky, *Z. Phys. Chem. B*, 1930, **11**, 163–210.
[15] R. Ramesh and N. A. Spaldin, *Nat. Mater.*, 2007, **6**, 21–29.

Chapter 2

Fundamental Concepts

The purpose of this chapter is to give a brief introduction of the basic physicochemical background of the research presented in this dissertation. First the material class investigated in this work — that is perovskite oxides — is presented. Then the imperative to study the defect behaviour of the perovskite oxide $SrRuO_3$ is motivated by familiarizing the reader with some of the material's unique properties. Subsequently the concept of defect chemistry is presented. Due to the lack of systematic defect-chemical data for $SrRuO_3$, $SrTiO_3$ here serves as a prototype material to exemplify this concept. Not only the classically considered point-defects will be treated, but also extended defects are considered. In particular concepts to characterize interface properties are introduced. The tool employed in this work to investigate defects is diffusion. Hence the theory of diffusion will be presented for the two classic concepts of bulk diffusion and diffusion along extended defects.

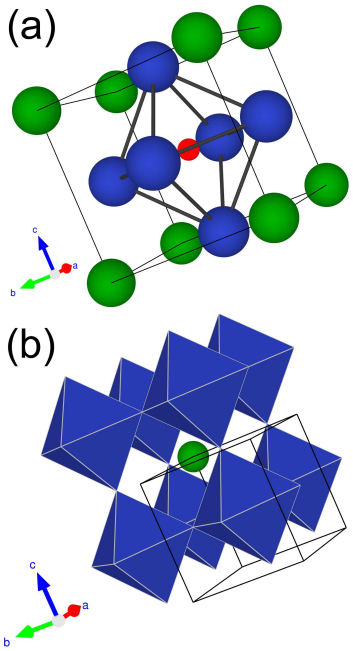

Figure 2.1: (a) Crystal structure of a cubic ABO_3 perovskite. The A-site cations (green) are arranged in a primitive cubic lattice with the oxygen anions (blue) on the octahedral sites on the cell edges. The B-site cation resides in the center of the cube. (b) Polyhedra representation of the perovskite structure. Here the universal building principle and the cuboctahedral coordination of the B-site cation are emphasized.

2.1 Perovskite Oxides

The mineral name "perovskite" — originally referring only to $CaTiO_3$ [1] — has become the eponym for a whole class of materials with the general formula ABO_3.[1] This class encompasses a large amount of oxides exhibiting a astonishing range of properties.[5,6] Electrically insulating,[7] semiconducting,[8] conducting[9] and superconducting[10]

[1] Although most commonly the term perovskite refers to oxides, there are also non-oxide compounds possesing perovskite structure. Among them are perovskite-fluorides[2], perovskite-hydrides[3] and more exotic compounds such as $MgCNi_3$[4].

perovskites can be found. Perovskites can be either ferroelectric,[11] ferrormagnetic[12] or multiferroic.[13] Furthermore ionic conduction in perovskites can be enabled by different species, the most common are O^{2-} [14,15], H^+ [16,17] and Li^+ [18–20]. Particularly the oxygen ion conductivity varies over orders of magnitude.[15,21,22]

It is this range of properties that makes perovskites interesting for a similarly widespread scope of applications stretching from energy conversion[23,24] over catalysis[5] to data storage and processing.[12,25,26] This versatility primarily stems from the perovskites' malleable crystal structure (shown in Fig. 2.1) which on the A and B site can accomodate with 100% substitution almost every element in the periodic table. From a structural point of view a pervoskite oxide is a network of cornershared BO_6 octahedra with the A site cation filling the 12-fold coordinated cavity centred in between eight of such octahedra.

Despite the common octahedra based-building principle, the crystal symmetry still varies between different compounds. It depends on the size ratio of the ions forming the structure. This size-ratio — the Goldschmidt[27] tolerance factor t_G — is defined as

$$t_G = \frac{R_A + R_O}{\sqrt{2}(R_B + R_O)} \tag{2.1}$$

with R_A,R_B and R_O being the radii of A, B and O ions[28] (in 12- and in 6-fold coordination respectively). In order for the octahedra based building principle to result in a stable perovskite structure, the tolerance factor has to take a value between $0.8 \leq t_G \leq 1$. In case of $0.89 \leq t_G \leq 1$ ideal cubic symmetry can be established with a unit cell containing one formula unit of ABO_3. For values of $0.8 \leq t_G < 0.89$ the BO_6 octahedra tilt so that the symmetry is reduced. This is the case for the here investigated $SrRuO_3$, but also for the eponymic $CaTiO_3$; both being orthorhombic. For $0.8 \leq t_G$ the Ilmenite structure is more stable, for $t_G > 1$ hexagonal structures with face-sharing octahedra are preferred. A comprehensive overview of these structural relations is given in Refs. [29,30].

2.2 The Perovskite Oxide $SrRuO_3$

$SrRuO_3$ is a ferromagnetic and metallic perovskite with orthorhombic unit cell parameters $a = 5.567\,\text{Å}$, $b = 5.530\,\text{Å}$, $c = 7.845\,\text{Å}$ (Fig. 2.2 (a)).[31,32] The perovskite character of $SrRuO_3$ is best illustrated by looking at its polyhedra representation depicted in Fig. 2.2 (b), where the building principle of corner sharing octahedra becomes evident. To further account for this building principle, often only the dimensions of one ABO_3 unit is compared. This is the pseudocubic representation. For $SrRuO_3$ the pseudo-cubic lattice constant is $a_{pc} = 3.93\,\text{Å}$ (see the dotted line in Fig. 2.2 (a)). At higher temperatures the tilted octahedra align. In that manner symmetry is increased from orthorhombic to tetragonal (at $T = 820\,\text{K}$) and eventually to cubic (at $T = 950\,\text{K}$).[33] In strained thin films on $SrTiO_3$ substrates the tetragonal symmetry is stabilized down to temperatures as low as $T = 553\,\text{K}$.[34]

Thin films have become the most commonly inverstigated form of $SrRuO_3$. This is because the ease of fabricating $SrRuO_3$ thin-films and integrating them into a variety of all-oxide

devices. In such devices $SrRuO_3$ either serves as a functional unit or the electrode material. Potential applications include resistive switches,[25,26] ferroelectric storage devices,[35–37] ferroelectric tunnel junctions[38] and multiferroic tunnel junctions.[39] Furthermore $SrRuO_3$ is probably the most wiedely employed electrode material in this field. A comprehensive review of $SrRuO_3$'s properties can be found in Ref. [40]. Here I will focus only on some of these properties to demonstrate the importance of a defect-chemical investigation of this material.

From an eletronic point of view $SrRuO_3$ is a highly compensated metal with both electron-like and hole-like bands contributing to its conductivity. The hole-like parts of the Fermi-surface dominate the conductivity at high temperatures and the electronlike parts at low temperatures.[41,42] At high temperatures ($T \geq 200\,\mathrm{K}$) the resistivity exhibits a linear temperature dependence without saturation. Applying the classic Drude model of electronic conduction to these data results in a mean free path for electronic charge carriers of less than the interatomic distances, implying the breakdown of Boltzmann transport theory. This characteristic is often refered to as "bad metal" behaviour.[43] A more recent definitions of bad metals extends the sole focus on resistivity and also takes the unusual behaviour of the thermopower, Hall resistance and optical conductivity into account.[44] A more detailed insight into the bad metallic behaviour can only be obtained by understanding the electronic structure. For $SrRuO_3$ it is known that the density of states on the Fermi-surface in is dominated by the O $2p$ and the Ru $4d(t_{2g})$ orbitals.[45–48] For this reason the electric behaviour is influenced a great deal by defects either in the cation[49,50] or in the oxygen-[51] sublattice. At low temperatures — that is the regime from 0 K to 30 K — defect-induced disorder decisively determines the nature of the metallic state. The influence of electron-electron scattering, for example, strongly depends on the degree of disorder introduced by defects.[52–55] A further important property of $SrRuO_3$ is its ferromagnetism. The Curie temperature is in bulk or single crystal samples is $T_C \approx 150\,\mathrm{K}$[56] and is typically somewhat lower in thin-films $T_C \approx 150\,\mathrm{K}$.[57] This ferromagnetism is due to the Ru $4d$ electrons and is generally classified as itinerant.[40] The degree of itineracy, however, can be changed by introducing either impurity or vacancy defects into the system.[58,59] In that manner the magnetic properties can be tuned by defects. Inspite of the vast amount of research devoted

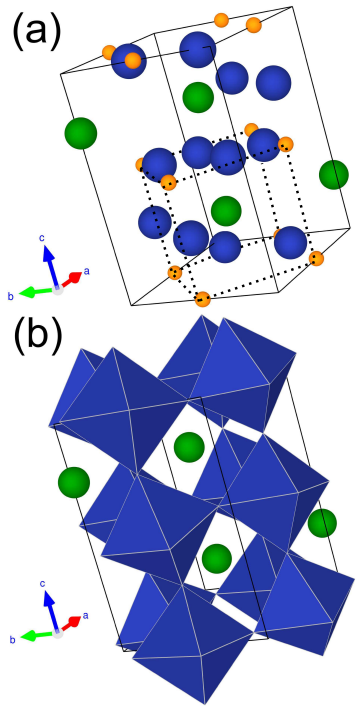

Figure 2.2: (a) Crystal structure of $SrRuO_3$ represented in its orthorhombic unit cell containing four formula units of $SrRuO_3$. A-site Sr (green), B-site Ru (orange) and oxygen anions (blue). The dotted line represents the pseudo-cubic unit cell comprising only one unit of $SrRuO_3$ (b) The polyhedra representation of the structure emphasises the perovskite building principle and thus the classification of $SrRuO_3$ as a perovskite.

to defects in $SrRuO_3$ a classical understanding of $SrRuO_3$'s defect chemistry is still lacking. With the term "defect-chemistry" one associates an understanding of the mutual dependence of all — ionic as well as electronic — defects on each other and their dependence on the thermodynamic functions of state, such as temperature T and oxygen partial pressure pO_2.

2.3 Defect Chemistry

Defects are all deviations from the perfect arrangement of atoms in a crystal . Generally defects in solids can be classified into two categories: point and extended defects. . In the first part of this section the concept of point defects in oxides is introduced and guidelines for their thermodynamic treatment are given. In the second part, a brief introduction into the concept of higher dimensional defects follows. The concept of point defect thermodynamics will then be illustrated using $SrTiO_3$ as the example system .

2.3.1 Point-defects in Oxides

The state of lowest energy in a crystal is always defined by two competing driving forces. On the one hand ordering interaction forces and on the other hand the general tendency to maximize entropy by increasing disorder. For 0-dimensional point defects the overall energy-decrease due to configurational entropy is larger than the energy needed to create these defects. Therefore point defects are an inherent feature of matter and their concentration is characteristic of its equilibrium state.[60] There are different ways defects in an otherwise perfect periodic arrangement of atoms can occur: As a vacancy, i.e. a missing atom on a regular lattice site; as an interstitial, i.e. an atom on a position unoccupied in the unperturbed lattice; or as an impurity or dopant, i.e. an atom of an element otherwise not present in the host lattice. In compound materials the different constituents each occupy a separate sublattice. An antisite defect occurs, if atoms of different species exchange lattice sites.

By the introduction of defects into a crystal charge neutrality of the system has to be preserved. For this reason in ionic crystals defects always occur in complementarily charged pairs. This constraint imposes three rules on the formulation of formation reactions of all defects: First, the mass of the ions has to be conserved. Second, the crystal has to stay electroneutral. Third, the structure of the crystal has to be preserved (the ratio of anion to cation sites has to be maintained)[61,62]. Defect pairs typical of a binary oxide system MO are depicted in Fig. 2.3. The corresponding defect reactions and equilibria will be described in the following.

Throughout this description the Kröger-Vink-Notation[63] is used: The general notation S_{site}^{charge} specifies an element in a crystal. S is the indicated species, whether an atom M/O or a vacancy V. The subscript describes the crystallogrpahic site in the lattice; either a regular lattice site or an interstitial position (M/O or i). The superscript indicates the charge with respect to the regular lattice site ($\times$ = neutral; $'$ = negative; $\bullet$ = positive) in units of the elementary charge.

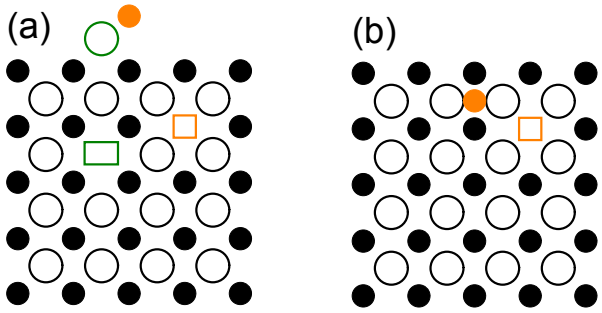

Figure 2.3: Common defect pairs in ionically bonded materials (a) Schottky disorder: a cation-anion vacancy pair with the corresponding spcies being exspelled to the sample surface (b) Frenkel disorder: a cation interstitial is formed leaving the corresponding regular lattice site vacant.

The Schottky-reaction (Eq. (2.2)) in a binary oxide MO generates anion and cation vacancies ($V_X^{\bullet\bullet}$ and V''_M) by expelling the corresponding entities to the sample surface and forming MO_s at the surface.

$$M_M^\times + O_O^\times \rightleftharpoons V''_M + V_O^{\bullet\bullet} + MO_s \tag{2.2}$$

The corresponding law of mass action (LMA) links the defect concentrations with an equilibrium constant $K_{\text{Schottky}}(T)$ specific for the material and depending only on temperature. The temperature dependence exhibits an Arrhenius type behaviour characterized by an activation enthalpy $\Delta H_{\text{Schottky}}$ and a preexponential factor $K^\circ_{\text{Schottky}}$.

$$K_{\text{Schottky}}(T) = K^\circ_{\text{Schottky}} \exp\left(\frac{-\Delta H_{\text{Schottky}}}{k_B T}\right) = \frac{[V''_M][V_O^{\bullet\bullet}][MO_s]}{[M_M^\times][O_O^\times]} \tag{2.3}$$

Here k_B is the Boltzmann constant and T the absolute temperature. A pair of Frenkel defects, consists of an interstitial ion $M_i^{\cdot\cdot}$ and a vacancy on a regular lattice site V''_M:

$$M_M^\times + V_i^\times \rightleftharpoons V''_M + M_i^{\bullet\bullet} \tag{2.4}$$

The corresponding law of mass action for the Frenkel equilibrium with the corresponding constants can be formulated as

$$K_{\text{Frenkel}}(T) = K^\circ_{\text{Frenkel}} \exp\left(\frac{-\Delta H_{\text{Frenkel}}}{k_B T}\right) = \frac{[V''_M][M_i^{\bullet\bullet}]}{[M_M^\times][V_i^\times]}. \tag{2.5}$$

In the crystallographically densely packed lattice of perovskites the formation enthalpy $\Delta H_{\text{Frenkel}}$ of the Frenkel equilibrium is high. Thus neither cation nor anion interstitials are expected to be present in noteworthy amounts.[64–67] For this reason defect equilibria involving interstitials will receive no further attention in this context. Impurity defects on the other hand are far more common, whether intentionally added to the crystal as dopants or unintentionally present as impurities.

A dopant replaces an ion on a anion or cation site and possesses either a higher, lower or

the same valence state as the substituted moiety. In the latter case of isovalent doping no influence on the defect concentrations is expected, as long as all defects can be considered as dilute non-interacting species. In the two former cases, however, the aliovalent dopant carries a positive or negative excess charge compared to the unperturbed lattice which needs to be compensated for by an complementarily charged defect.
The introduction of an acceptor dopant N_2O into the binary oxide can, for instance, be formulated as follows:

$$N_2O + 2M_M \longrightarrow 2N'_M + V_O^{\bullet\bullet} + 2MO \tag{2.6}$$

Here the negative excess charge N'_M is compensated for by positively charged oxygen vacancies $V_O^{\bullet\bullet}$. It is important to note that Eq. (2.6) represents an incorporation reaction and not an equilibrium process. Hence doping — intentional or not — is a powerful tool to influence material properties permanently.
Not only doping can be regarded as a means to extrinsically influence the defect behaviour. At a given temperature and partial pressure, the component activities can also determine the degree of deviation from ideal stoichiometry: The interaction of the compound MO with a surrounding gas athmosphere can be formulated according to Eq. (2.7): The incorporation of O as O^{2-} onto a vacancy site accompanied by the generation of electron holes $h^\bullet$. (Eq. (2.7) could also be formulated as a reduction reaction, then electrons e' would be the compensating defects that would annihilated).

$$\frac{1}{2}O_2 + V_O^{\bullet\bullet} \rightleftharpoons O_O^X + 2h^\bullet \tag{2.7}$$

with the corresponding LMA linking the oxygen activity aO_2 outside of the compound with the defect concentrations.

$$K_{\text{incorp}}(T) = K^\circ_{\text{incorp}} \exp\left(\frac{-\Delta H_{\text{incorp}}}{k_B T}\right) = \frac{[O_O^\times][h^\bullet]}{[V_O^{\bullet\bullet}]aO_2{}^{1/2}} \tag{2.8}$$

Comparing above equations, we see that they are not linearly independent. In order to solve above equations for the individual defect concentrations, we however need an equal amount of unknowns and equations. The missing condition is global charge neutrality:

$$\sum n[S_{\text{site}}^{n\bullet}] \stackrel{!}{=} \sum n[S_{\text{site}}^{n'}] \tag{2.9}$$

The total charge of all positive defects has to equal the total charge of all negatively charged defects present in the material. n indicates the number of positive ($\bullet$) of negative ($'$) units of the elementary charge. Eq. (2.9) thus provides the connection between all possible defect formation reactions. In many cases not only the above mentioned equilibria have to be considered, but also electronic defects and reactions of defects with each other. A detailed example of possible defect reactions and the corresponding equilibria is given in Sec. (2.3.3) for $SrTiO_3$, a material whose defect chemistry has been comprehensively investigated.[68–77] For most oxides the incorporation reaction Eq. (2.7) and the corresponding LMA

Eq. (2.8) are used as the starting point for these defect chemical investigations. This is because aO_2 can easily be varied experimentally and thus the concentrations of all other defects are adjusted accordingly and can be measured by suitable means, e.g. by conductivity or diffusion measurements. Comprehensive reviews of these defect-chemical principles can be found in Refs. [61,62,78–81].

2.3.2 Extended defects

"Extended defects" are all permanent deviations from structural perfection of higher dimensionality than zero.

Extended defects in the bulk of a solid only occur due to deviations from thermodynamic equilibrium, as the gain in configurational entropy due to their formation does not compensate for the energy needed to generate them. For this reason higher order defects are always a consequence of instabilities during growth and processing. In other words the concentration of extended defects is stipulated by the sample's history rather than the thermodynamic conditions the sample is exposed to.[2]

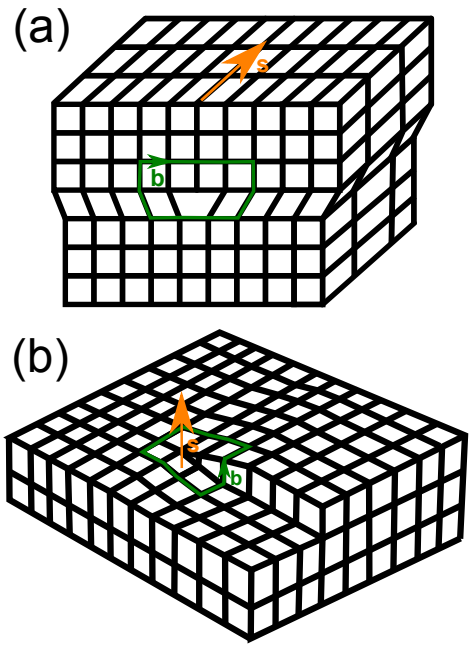

Figure 2.4: Schematic representation of (a) an edge dislocation in a crystal. The Burgers vector **b** indicting direction and magnitude of the lattice distortion is perpendicular to the direction of the dislocation **s** (b) a screw dislocation. Here the Burgers vector is parallel to the dislocation line.

Extended defects are classified by the number of dimensions the defect extends in. 1-dimensional defects are dislocations, which are represented by two ideal cases depicted in Fig. 2.4 (a) and (b): Edge dislocations can be visualized (Fig. 2.4 (a)) as an additional half lattice plane inserted into the crystal and thereby distorting the surrounding structure. The dislocation line is the line represented by the end of this additional lattice plane. A further characteristic of the dislocation is its Burgers vector **b**, which specifies the direction and quantifies the magnitude of lattice distortion exerted by the dislocation. The Burgers vector can be obtained by drawing a closed circuit around the dislocation and comparing it with the same circuit drawn in the undistorted lattice; the difference is the Burgers vector **b** (see Fig. 2.4). The defining characteristic of an edge dislocation is that the Burgers vector **b** is always perpendicular to the dislocation line **s**. The opposite holds true for a screw dislocation shown in Fig. 2.4 (b). Here the Burgers vector is always parallel to the dislocation line. In most cases dislocations have a mixed screw- and edge- type character. An important implication of the above description is that the dislocation line of neither a screw nor an edge dislocation can abruptly end in the crystal

[2] The thermodynamics of crystal surfaces is treated within a separate framework, which includes surface point defects as well as surface relaxation phenomena. [82,83]

lattice. For this reason dislocations either terminate at crystal surfaces, internal interfaces or interconnect and form dislocation networks and dislocation loops.
2-dimensional or planar defects in a crystal occur in three different ways: As the crystal's free surface, the area where the periodic arrangement of atoms terminates at either a vapour or liquid; as intercrystalline interfaces separating grains or phases in a crystal; internal interfaces disrupting the periodicity of the atomic arrangement such as stacking faults or antiphase boundaries. In this context intercrystalline interfaces between crystal grains of different orientation, grain boundaries (GB) , are most important. The grain boundary structure depends on the degree of misorientation between the individual grains. As long as the differences in orientation between adjacent grains are small, grain-boundaries can be considered as arrays of individual dislocations. Larger misorientations result in more perturbed areas between grains. What is common to both dislocations and grain-boundaries, is that their presence influences many material properties such as plasticity, electric resistivity and most important the diffusion behaviour. In Sec. (2.5.2) some theoretical aspects of diffusion in the presence of extended defects will be discussed. 3-dimensional lattice defects such as voids and precipitates can also occur and have a variety of functions in a material. In this work however due care is taken to avoid these kind of defects, hence they will not be discussed here. In writing this section, Refs. [78,84–86] were consulted as references and shall be referred to as more detailed references.

2.3.3 Defects in $SrTiO_3$

The point-defect behaviour of $SrTiO_3$ has been extensively investigated [70–77] and is nowadays understood to a remarkable degree. [68,69] This knowledge can be used to predict the concentrations of any defect present at a given temperature T and surrounding oxygen activity aO_2 under the assumption of a certain a acceptor dopant concentration $[\mathrm{Acc}'_{\mathrm{Ti}}]$ in the sample. The prerequisite for a defect reaction to take place is the mobility of the participating moieties. For the calculation of defect concentration it is therefore mandatory that the considered reactions are not kinetically inhibited. For $SrTiO_3$ the kinetic activation of the different defect reactions can be used to classify the behaviour into three regimes (cf. Ref. [81,87–89]):

Low-temperature regime $T \leq 550\,\mathrm{K}$

The low temperature regime is defined as the regime where no exchange of oxygen between sample and the surrounding atmosphere occurs. Electronic defects, that is electrons e' and holes $\mathrm{h}^\bullet$, are generated by thermal exitation of electrons above the band-gap.

$$nil \rightleftharpoons \mathrm{h}^\bullet + \mathrm{e}' \tag{2.10}$$

with the corresponding law of mass action (LMA)

$$[\mathrm{e}'][\mathrm{h}^\bullet] = N_{\mathrm{VB}} N_{\mathrm{C}} \exp\left(\frac{-E_{\mathrm{g}}(T)}{k_{\mathrm{B}} T}\right) \tag{2.11}$$

Here N_{VB} and N_{C} are the effective densities of states at the valance-band and at the conduction-band edge. $E_g(T)$ is the temperature-dependent band-gap, k_{B} the Boltmann constant and T the absolute temperature.

In ionic crystals not only band-excitation generates electronic charge carriers. The ionisation of oxygen vacancies, for instance, also contributes to the generation of electronic charge carriers: Oxygen vacancies can be either singly (see Eq. (2.12)) or doubly (see Eq. (2.13)) ionized:

$$\mathrm{V}_{\mathrm{O}}^{\times} \rightleftharpoons \mathrm{V}_{\mathrm{O}}^{\bullet} + \mathrm{e}' \tag{2.12}$$

$$\mathrm{V}_{\mathrm{O}}^{\bullet} \rightleftharpoons \mathrm{V}_{\mathrm{O}}^{\bullet\bullet} + \mathrm{e}' \tag{2.13}$$

The corresponding LMAs are:

$$\frac{[\mathrm{e}'][\mathrm{V}_{\mathrm{O}}^{\bullet}]}{[\mathrm{V}_{\mathrm{O}}^{\times}]} = K^{\circ}_{\mathrm{V}_{\mathrm{O}}^{0/1}} \exp\left(\frac{-\Delta H_{\mathrm{V}_{\mathrm{O}}^{0/1}}}{k_{\mathrm{B}}T}\right) \tag{2.14}$$

$$\frac{[\mathrm{e}'][\mathrm{V}_{\mathrm{O}}^{\bullet\bullet}]}{[\mathrm{V}_{\mathrm{O}}^{\bullet}]} = K^{\circ}_{\mathrm{V}_{\mathrm{O}}^{1/2}} \exp\left(\frac{-\Delta H_{\mathrm{V}_{\mathrm{O}}^{1/2}}}{k_{\mathrm{B}}T}\right) \tag{2.15}$$

With $\Delta H_{\mathrm{V}_{\mathrm{O}}^{0/1}}/\Delta H_{\mathrm{V}_{\mathrm{O}}^{1/2}}$ and $K_{\mathrm{V}_{\mathrm{O}}^{0/1}}/K_{\mathrm{V}_{\mathrm{O}}^{1/2}}$ the respective activation enthalpies and preexponential factors for single and double ionization of oxygen vacancies. Both ionization enthalpies are very small,[68,90,91] hence oxygen vancancies can be considered as doubly charged moieties over the entire temperature range considered in this work.

If we consider oxygen vacancies as shallow donors with an energy level very close to the conduction band, cation vacanciescan analogously be classified as shallow donors with energy levels close to the valence band. This particularly holds for strontium vacancies:

$$\mathrm{V}_{\mathrm{Sr}}^{\times} \rightleftharpoons \mathrm{V}'_{\mathrm{Sr}} + \mathrm{h}^{\bullet} \tag{2.16}$$

$$\mathrm{V}'_{\mathrm{Sr}} \rightleftharpoons \mathrm{V}''_{\mathrm{Sr}} + \mathrm{h}^{\bullet} \tag{2.17}$$

The corresponding LMAs are

$$\frac{[\mathrm{V}'_{\mathrm{Sr}}][\mathrm{h}^{\bullet}]}{[\mathrm{V}_{\mathrm{Sr}}^{\times}]} = K^{\circ}_{\mathrm{V}_{\mathrm{Sr}}^{0/1}} \exp\left(\frac{-\Delta H_{\mathrm{V}_{\mathrm{Sr}}^{0/1}}}{k_{\mathrm{B}}T}\right) \tag{2.18}$$

$$\frac{[\mathrm{V}''_{\mathrm{Sr}}][\mathrm{h}^{\bullet}]}{[\mathrm{V}'_{\mathrm{Sr}}]} = K^{\circ}_{\mathrm{V}_{\mathrm{Sr}}^{1/2}} \exp\left(\frac{-\Delta H_{\mathrm{V}_{\mathrm{Sr}}^{1/2}}}{k_{\mathrm{B}}T}\right) \tag{2.19}$$

.

Compared to their donor counterparts, the acceptor ionisation enthalpies are much higher and hence differently charged strontium vacancies can be present in the material at the considered

temperatures.[68,91] Titanium vacancies, since their existence is energetically unfavorable, are of negligible importance in $SrTiO_3$. Besides intrinsic cationic defects, also the majority of impurities in the cation sublattice act as acceptors . Here the ionization reaction can be formulated by Eq. (2.20), with Acc_{Ti}^{X} being an acceptor impurity residing on a Ti lattice site:

$$Acc_{Ti}^{\times} \rightleftharpoons Acc'_{Ti} + h^{\bullet} \tag{2.20}$$

The LMA is given by

$$\frac{[Acc'_{Ti}][h^{\bullet}]}{[Acc_{Ti}^{\times}]} = K_{ion}^{\circ} \exp\left(\frac{-\Delta H_{ion}}{k_B T}\right). \tag{2.21}$$

A further reaction taking place at low temperatures is the association of acceptor dopants with oxygen vacancies:

$$Acc'_{Ti} + V_O^{\bullet\bullet} \rightleftharpoons \{Acc'_{Ti} - V_O^{\bullet\bullet}\}^{\bullet} \tag{2.22}$$

and the LMA

$$\frac{\{Acc'_{Ti} - V_O^{\bullet\bullet}\}^{\bullet}}{[Acc'_{Ti}][V_O^{\bullet\bullet}]} = K_{Acc}^{\circ} \exp\left(\frac{-\Delta H_{Acc}}{k_B T}\right) \tag{2.23}$$

The association of acceptor ions alters the amount of acceptors needed to be charge compensated, which influences the concentration of all other defects. This has to be accounted for by considering that the total amount of dopant is divided among neutral, charged and associated acceptor ions:

$$[Acc_{Ti}] = [Acc_{Ti}^{\times}] + [Acc'_{Ti}] + [\{Acc'_{Ti} - V_O^{\bullet\bullet}\}^{\bullet}] \tag{2.24}$$

Intermediate-temperature regime $750 \leq T/\mathrm{K} \leq 1300$

The intermediate-temperature regime is defined by the oxygen incorporation reaction becoming active, but cationic defects still being immobile.
Oxygen incorporation into the lattice enables the oxygen sublattice to establish equilibrium with the surrounding gas-phase. Which means that defect concentration can be deliberately tuned by establishing a defined oxygen activity aO_2 surrounding the sample.
This tuning of defect concentrations can be formulated as an oxidation reaction:

$$\frac{1}{2}O_2(g) + V_O^{\bullet\bullet} \rightleftharpoons O_O^{\times} + 2h^{\bullet} \tag{2.25}$$

The equilibrium of the reduction reaction is again defined by the corresponding LMA

$$\frac{[O_O^{\times}][h^{\bullet}]^2}{[V_O^{\bullet\bullet}]aO_2^{1/2}} = K_{red}^{\circ} \exp\left(\frac{-\Delta H_{red}}{k_B T}\right) \tag{2.26}$$

In this context it has to be mentioned that oxygen vacancies in the lattice react not only with molecular oxygen, but also with water.[16,92] In this work due care was taken to avoid the

presence of water in the experimental setup (see Sec. 3.3). Therefore any hydration reaction and incorporation of hydroxyde groups will be neglected.

High-temperature regime $T \geq 1300\,\mathbf{K}$

At temperatures above $T \geq 1300\,\mathrm{K}$ the cations are mobile as well and the Schottky equilibrium becomes active. This means that an entire formula unit of $SrTiO_3$ gets expelled from the lattice and vacancies of the corresponding entities are formed (Eq. (2.27)).

$$\mathrm{Sr}_{\mathrm{Sr}}^{\times} + \mathrm{Ti}_{\mathrm{Ti}}^{\times} + 3\mathrm{O}_{\mathrm{O}}^{\times} \rightleftharpoons \mathrm{V}_{\mathrm{Sr}}'' + \mathrm{V}_{\mathrm{Ti}}'''' + 3\mathrm{V}_{\mathrm{O}}^{\bullet\bullet} + \mathrm{SrTiO_3(surf.)} \tag{2.27}$$

In $SrTiO_3$the full Schottky reaction as formulated in Eq. (2.27) is negligible, because the perovskite structure restricts the amount of Ti vacancies. [91,93] For this reason cation vacancies are primarily formed in the Sr sublattice and the partial Schottky-equilibrium dominates the behaviour:

$$\mathrm{Sr}_{\mathrm{Sr}}^{\times} + \mathrm{O}_{\mathrm{O}}^{\times} \rightleftharpoons \mathrm{V}_{\mathrm{Sr}}'' + \mathrm{V}_{\mathrm{O}}^{\bullet\bullet} + \mathrm{SrO}(surf.) \tag{2.28}$$

The corresponding LMA is

$$\frac{[\mathrm{V}_{\mathrm{Sr}}''][\mathrm{V}_{\mathrm{O}}^{\bullet\bullet}]a\mathrm{SrO}}{[\mathrm{O}_{\mathrm{O}}^{\times}][\mathrm{Sr}_{\mathrm{Sr}}^{\times}]} = K_{\mathrm{Sch}}^{\circ} \exp\left(\frac{-\Delta H_{\mathrm{Sch}}}{k_{\mathrm{B}}T}\right) \tag{2.29}$$

Experimentally determined values of the equilibrium constants are$\Delta H_{\mathrm{Sch}} = 2.5\,\mathrm{eV}$ and $K_{\mathrm{Sch}}^{\circ} = 3 \times 10^{44}\,\mathrm{cm}^{-6}$.[68]

Calculating defect concentrations

In Section 2.3.1 it was emphasised that the tool linking all defect equations discussed above is the charge neutrality condition. In the case of $SrTiO_3$ there are eight charged defects that have to be considered: electrons and holes, charged acceptor dopans, singly and doubly charged oxygen and strontium vacancies and dopand vacancy associates. Thus the full charge neutrality condition reads:

$$[\mathrm{e}'] + [\mathrm{Acc}_{\mathrm{Ti}}'] + 2[\mathrm{V}_{\mathrm{Sr}}''] + [\mathrm{V}_{\mathrm{Sr}}'] = [\mathrm{h}^{\bullet}] + 2[\mathrm{V}_{\mathrm{O}}^{\bullet\bullet}] + [\mathrm{V}_{\mathrm{O}}^{\bullet}] + \{\mathrm{Acc}_{\mathrm{Ti}}' - \mathrm{V}_{\mathrm{O}}^{\bullet\bullet}\}^{\bullet} \tag{2.30}$$

In addition also the neutral moieties in the oxygen and strontium sublattices and neutral acceptor dopants have to be considered. This means there are 11 unknowns. Hence 11 equations must be solved simultaneously for defined thermodynamic conditions (T, $a\mathrm{O}_2$).
The defects are, however, not all of equal significance, as the equilibrium constants of the respective equilibria differ. In the intermediate temperature regime for instance, all defects can be regarded as fully ionized and the partial-Schottky equilibrium (Eq. (2.28)) will be inactive. This means that the concentration of strontium vacancies is frozen in and these defects can be considered as additional acceptors. In total the acceptor concentration thus increases and only an effective acceptor concentration with $[\mathrm{Acc}_{\mathrm{Ti}}']_{\mathrm{eff}}=[\mathrm{Acc}_{\mathrm{Ti}}']+2[\mathrm{V}_{\mathrm{Sr}}'']$ has to

be considered. Typically $[\mathrm{Acc}'_{\mathrm{Ti}}]_{\mathrm{eff}} \approx 7 \times 10^{17}\,\mathrm{cm}^{-3}$ holds for commercially available $SrTiO_3$ single crystals.[69] In that way the charge neutrality condition simplifies to the following expression:

$$[\mathrm{e}'] + [\mathrm{Acc}'_{\mathrm{Ti}}]_{eff} \approx [\mathrm{h}^{\bullet}] + 2[\mathrm{V}_{\mathrm{O}}^{\bullet\bullet}]. \tag{2.31}$$

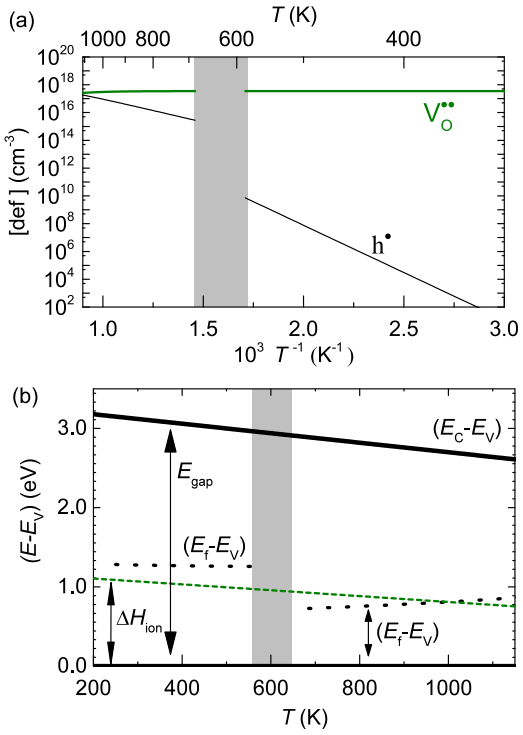

Figure 2.5: (a) Electron hole [$\mathrm{h}^{\bullet}$] and oxygen vacancy [$\mathrm{V}_{\mathrm{O}}^{\bullet\bullet}$] concentrations in the temperature range considered in this work. Oxygen incorporation freezes in at $T = 523\,\mathrm{K}$ and is kinetically inhibited in the grey shaded area (see text) (b) The position of he Fermi-level E_{f} with respect to the valance band edge E_{V}. The level of acceptor impurities as well as the distance to the conduction band edge E_{C} (band gap E_{gap}) are shown.

This is the reason why in the intermediate temperature regime one has to solve the set of {Eq. (2.11), Eq. (2.26), Eq. (2.31)} for the three unknown defect concentrations of interest ([e′], [$\mathrm{h}^{\bullet}$] and [$\mathrm{V}_{\mathrm{O}}^{\bullet\bullet}$]). Upon further reduction of the temperature the oxygen vacancy concentration [$\mathrm{V}_{\mathrm{O}}^{\bullet\bullet}$] freezes, too. Only electronic charge carriers remain mobile. We assume that due to the low concentration of acceptor dopants and the small association enthalpy of the reaction described in Eq. (2.23) the concentration of dopant-vacancy associates is negligible, too.

The acceptor ionization reaction Eq. (2.20), however, still has to be taken into account. Hence one now has to solve a set of four equations {Eq. (2.11), Eq. (2.21), Eq. (2.24), Eq. (2.31)} for the four unknowns, which are [e′], [$\mathrm{h}^{\bullet}$], [$\mathrm{Acc}'_{\mathrm{Ti}}$] and the unionized acceptor concentration [$\mathrm{Acc}^{\times}_{\mathrm{Ti}}$]. Fig. 2.5 depicts the electron-hole [$\mathrm{h}^{\bullet}$] and oxygen-vacancy concentrations [$\mathrm{V}_{\mathrm{O}}^{\bullet\bullet}$] in the intermediate and low temperature regime. The constants needed to solve the relevant equations are tabulated in Table 2.1.

For temperatures in the regime between $550 \leq T/\mathrm{K} \leq 650$ no concentrations are shown. Here the surface reaction is still active, but so slow that for a macroscopic sample it would take unreasonably long times (months to years) to reach thermodynamic equilibrium.

A further physical property of major importance is the electrochemical potential for electrons and holes, the Fermi-level E_{f}. Its position above the valence band edge E_{V} can be calculated

as follows:

$$(E_\mathrm{f} - E_\mathrm{V})(T) = k_\mathrm{B} T \ln\left(\frac{[\mathrm{h}^\bullet](T)}{N_\mathrm{V}(T)}\right) \tag{2.32}$$

The development of E_f with temperature is depicted in Fig. 2.5 (b). It is of particular interest to note that freezing the oxygen incorporation reaction (Eq. (2.25)) and the activation of the acceptor ionization reaction (Eq. (2.20)) result in a significant shift of the Fermi-level. Whereas the position of the Fermi-level might be of subordinate interest in the discussion of bulk-defect chemistry, it is of pivotal importance when discussing interface phenomena.

Constant	Value	Reference
N_V	$3.5 \times 10^{16}\,\mathrm{cm}^{-3}(T/\mathrm{K})^{3/2}$	[68]
N_C	$4.1 \times 10^{16}\,\mathrm{cm}^{-3}(T/\mathrm{K})^{3/2}$	[68]
E_gap	$(3.3\text{-}6 \times 10^{-4}\ T/\mathrm{K})\,\mathrm{eV}$	[94]
K°_ion	$=N_V$	-
ΔH_ion	$1.4\,\mathrm{eV}$	[95]
K°_red	$6.624 \times 10^{68}\,\mathrm{cm}^{-9}\,\mathrm{bar}^{0.5}$	[95]
ΔH_red	$5.581\,\mathrm{eV}$	[95]

Table 2.1: Thermodynamic constants employed for defect chemical calculation in $SrTiO_3$.

2.4 Perovskite Oxide Interfaces

In the preceding section the defect behaviour of bulk perovskites was described.
In order to exploit the properties induced by these defects, interfaces are needed to enable the interaction of the bulk material with its environment, whether this is other materials or the ambient atmosphere.
In any case the material seeks to be in equilibrium with the surrounding. A measure of this equilibrium is the electrochemical potential $\widetilde{\mu}_i$, which is specific for each chemical moiety i:

$$\widetilde{\mu}_i = \mu_i + z_i e k_\mathrm{B} \phi \tag{2.33}$$

here μ_i is the chemical potential and z_i the charge of moiety i. ϕ is the electric potential in the system considered. Thermodynamic equilibrium is characterized by $\widetilde{\mu}_i$ being constant for each moiety across the entire system considered. This means that at interfaces the electrochemical potential aligns in such manner that initially present spatial gradients in the electrochemical potential are eliminated.
In order to eliminate these gradients, mobile charge carriers will redistribute . This redistribution process results in local deviations from electro neutrality. The region in which these deviations occur is the globally neutral space charge layer (SCL). The existence of space charge layers in ionic crystals, especially at their surfaces, was predicted by Frenkel [96] and Lehovec [97]. A comprehensive and extended treatment of defect redistribution in perovskite oxides with focus on 2-dimensional defects (surfaces and grain-boundaries) is given

in Refs. [98,99]. In the following two features characterizing such interfaces will be discussed in more detail. First, details of calculating the extend of the space charge layer in a material will be given. This is followed by a brief discussion of models existing to estimate the magnitude of the difference in electric potential between two materials. Here the focus is on metal-semiconductor interfaces.

2.4.1 Charge Carrier Distribution in Space Charge Layers

In a space charge layer (SCL) all mobile charge carriers redistribute such that initial differences in the electrochemical potential are compensated. This gives rise to a difference in the electric potential across the interface Fig. 2.6. The distribution of the charge carriers is connected to that of the electric potential via Poission's equation:

$$\frac{\partial^2\phi(x)}{\partial x^2} = -\frac{\rho(x)}{\epsilon_\mathrm{r}\epsilon_0} \tag{2.34}$$

with $\phi_i(x)$ the electric potential; $\rho(x)$ the charge carrier density; ϵ_r the relative static and ϵ_0 the vacuum permittivity. Here it is sufficient to consider just one dimension with the spatial coordinate x.

Taking again the canonical example $SrTiO_3$ in the intermediate and low temperature regime, the mobile charge carriers are electrons, holes and oxygen vacancies. The major compensating defect are the immobile, but negatively charged accetor cations $[\mathrm{Acc}^{'}]$. Using the zero space-charge condition for the bulk of the material, that is the electroneutrality condition formulated in Eq. (2.31), the spatial variation of defects reads

$$\rho(z) = -e\left([\mathrm{Acc}^{'}] - 2[\mathrm{V}_\mathrm{O}^{\bullet\bullet}]_{(x)} - [\mathrm{h}^{\bullet}]_{(x)} + [\mathrm{e}']_{(x)}\right) \tag{2.35}$$

Assuming that all defects can still be treated as dilute, non-interacting species the charge carrier concentrations can be expressed by a Boltzmann-type expression. Thus the following Poisson-Boltzmann equation is obtained:

$$\begin{aligned}\frac{\partial^2\phi(x)}{\partial x^2} = -\frac{e}{\epsilon_\mathrm{r}\epsilon_0}\Big([\mathrm{Acc}^{'}] - 2[\mathrm{V}_\mathrm{O}^{\bullet\bullet}]_{(\infty)}\exp\left(\frac{-2e\phi(x)}{\mathrm{k_B}T}\right) \\ - [\mathrm{h}^{\bullet}]_{(\infty)}\exp\left(\frac{-e\phi(x)}{\mathrm{k_B}T}\right) + [\mathrm{e}']_{(\infty)}\exp\left(\frac{e\phi(x)}{\mathrm{k_B}T}\right)\Big)\end{aligned} \tag{2.36}$$

With $[\mathrm{V}_\mathrm{O}^{\bullet\bullet}]_{(\infty)}$, $[\mathrm{h}^{\bullet}]_{(\infty)}$ and $[\mathrm{e}']_{(\infty)}$ being the defect concentrations far away from the interface, where no space charge is present. The two boundary conditions neccessary to solve Eq. (2.36) are:

$$\frac{\partial\phi(\infty)}{\partial x} = 0 \tag{2.37}$$

and

$$\phi_i = \phi(\infty) - \phi(x=0) \tag{2.38}$$

ϕ_i is the so called interface potential, sometimes also refered to as built-in voltage (cf.Fig. 2.6).

ϕ_i can be considered as a characteristic value of an interface that strongly depends on its electronic structure. Measuring ϕ_i thus provides insight into the unique propterties of oxide interfaces. As ϕ_i strongly influences the defect distribution at an interface (cf. Eq. (2.36)) a measurement of for instance $[V_O^{\bullet\bullet}](x)$ provides indirect information of ϕ_i. To further emphasize the importance of ϕ_i for semiconductor and in particular perovskite oxide interfaces, models predicting its magnitude will be discussed in the following section.

2.4.2 Interface Potentials

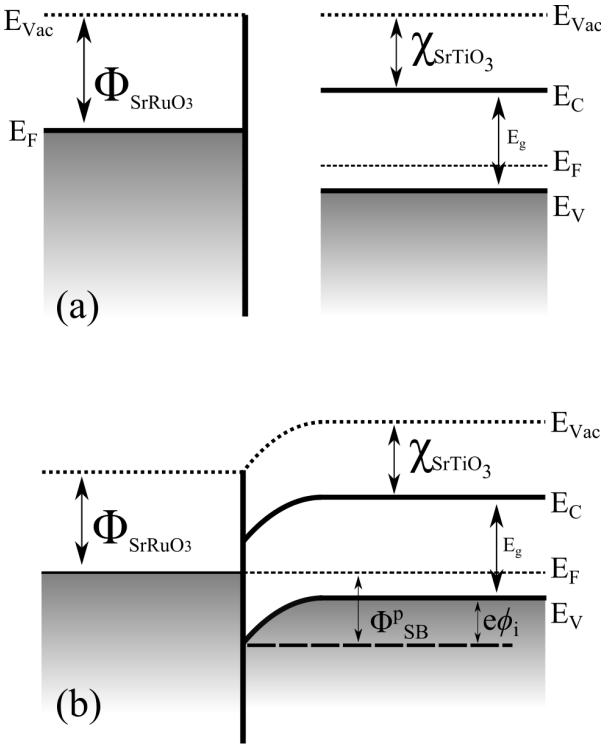

Figure 2.6: Band diagram of (a) $SrTiO_3$ and $SrRuO_3$ with $\Phi_{SrRuO_3} = (5.2 \pm 0.1)\,\mathrm{eV}$ [100] the metal-workfunction; $\chi_{SrTiO_3} = 4.1\,\mathrm{eV}$ [101,102] the electron affinity of the semiconductor; $E_g = (3.3 - 6 \times 10^{-4} T/\mathrm{K})\mathrm{eV}$ [94] the temperature dependend optical bandgap and (b) the $SrRuO_3|SrRuO_3$ Schottky junction characterized by the Schottky barrier height Φ_{SB} and the built-in voltage ϕ_i

As stated above, the electrochemical potential — in case of electronic charge carriers called Fermi-level E_f — is an inherent property of a material and by contacting two materials their respective electrochemical potentials align such that E_f is constant over the entire system. In Fig. 2.6 this alignment process is schematically illustrated for a metal-semiconductor contact comprised of the metallic $SrRuO_3$ and semiconducting $SrTiO_3$. As $SrRuO_3$ is a metal, the electrostatic potential in the interior is constant. For this reason electronic as well as ionic charge carrier redistribution compensating for the charge present at the interface is only expected to occur in $SrTiO_3$.

This situation thus corresponds to that of the gas-solid interface or of a charged grain-boundary core with adjacent bulk. Thus the same model as described in Sec. 2.4.1 can be used to calculate the defect redistribution.

As the interface potential ϕ_i determines this defect redistribution, being able to predict its magnitude is of particular interest.

In the most simple picture knowlegde of the metal work function Φ_M, the electron-affinity of the semiconductor χ_{SC} and band-gap E_g of the semiconductor would be sufficient to predict the Schottky barrier height (SBH). For a p-type semiconductor one gets (Schottky limit (cf. Fig. 2.6)):

$$\Phi_{SB}^{p} = E_g + \chi_{SC} - \Phi_M \tag{2.39}$$

The exclusive dependence of Φ_{SB}^{p} on the metal work function Φ_M receives, however, little support from experiment. The main reason for this discrepancy was identified to be the non-consideration of interface-states.

Because of the lack of knowledge about these interface states Bardeen assumed that the surface states of the semiconductor persist at the interface and pin the Fermi level (Eq. (2.40)). The ϕ_{SB}^{p} is in this case the position of the charge-neutrality level (CNL) above the valance band edge ϕ_{CNL}.

$$\phi_{SB}^{p} = \phi_{\mathrm{CNL}} \tag{2.40}$$

It is however unreasonable to assume that suface states remain unaltered upon contact with a metal. Therefore the salient question is how strong the metal influences the inferface/surface states. The degree of influence is taken into account by introducing the so called slope parameter S. For strong influence of the interface states the Fermi-level is pinned and $S = 0$, in case interface states are negligible the Schottky limit is valid and $S = 1$.

$$\Phi_{SB}^{p} = \phi_{\mathrm{CNL}} - S(\Phi_{\mathrm{M}} - E_{\mathrm{g}} - \chi_{\mathrm{SrTiO_3}} + \phi_{\mathrm{CNL}}) \tag{2.41}$$

From Eq. (2.41) it is evident that S can be determined by measuring ϕ_{SB}^{p} of different metals on the same material; $S = \frac{\partial \phi_{\mathrm{SB}}^{\mathrm{p}}}{\partial \Phi_{\mathrm{M}}}$, with ϕ_M being the metal workfunktion. Comparison of experimental data with predictions employing Eq. (2.41) yields good aggreement with experiments for a variety of systems.[103,104] In many cases the Schottky-barrier height $\Phi_{\mathrm{SB}}^{\mathrm{p}}$ rather than the interface potential ϕ_{i} is used to characterize the interface. Both values are connected via Eq. (2.42), with being the valence band offset $E_{\mathrm{f}} - E_{\mathrm{v}}$ as calculated in Sec. . (cf. also Fig. 2.6)

$$\Phi_{\mathrm{SB}}^{\mathrm{p}} = e\phi_{\mathrm{i}} + (E_{\mathrm{f}} - E_{\mathrm{v}}) \tag{2.42}$$

2.5 Diffusion in Solids

2.5.1 General Diffusion

"Diffusion is the transport of matter from one point to another by thermal motion of atoms or molecules"[105]. A continuum description of diffusion in solids is based on Fick's laws. Ficks first law (Eq. (2.43)) states that a species is transported with a flux $\boldsymbol{J}$ opposing the direction of its concentration gradient $\nabla \boldsymbol{C}$, with $\boldsymbol{C}$ being the scalar concentration field of the diffusant. Proportionality between the two variables is expressed by the diffusion constant $\boldsymbol{D}$, which is a symmetric, second rank tensor that reduces to a scalar quantity in isotropic media.

$$\boldsymbol{J} = -\boldsymbol{D}\nabla \boldsymbol{C} \tag{2.43}$$

In the absence of sources or sinks for the diffusing species, the amount of diffusant is conserved. Thus the continuity equation takes the form

$$-\nabla \boldsymbol{J} = \frac{\partial \boldsymbol{C}}{\partial t} \tag{2.44}$$

A combination of Fick's first law (Eq. (2.43)) with the continuity equation (Eq. (2.44)) yields Eq. (2.45) - Fick's second law - connecting the spatial and time dependence of the diffusant's concentration. This second order partial differential equation is also known as the diffusion equation.

$$\frac{\partial \boldsymbol{C}}{\partial t} = \nabla(\boldsymbol{D}\nabla \boldsymbol{C}) \tag{2.45}$$

Here the time dependence and spatial distribution of the diffusant in the sample is connected via its diffusion coefficient $\boldsymbol{D}$.

In many practical cases the coordinate system of the diffusion problem described by Eq. (2.45) can be chosen such that finding a solution is alleviated. Often the diffusion tensor D is spatially invariant and concentration independent and diffusion occurs only in one direction thus only one dimension with a constant D in Eq. (2.45) has to be considered. This simplifies Eq. (2.45) which then can be solved analytically under the constraints of appropriate initial and boundary conditions. In the following the one dimensional case is assumed, which is indicated by using the lower case c as the diffusant's concentration and x as a spatial variable.

In many cases initial and boundary conditions can be assigned to one of two types resulting in fundamentally different solutions: instantaneous or constant source conditions. In both cases it is assumed that the diffusant diffuses from its source into an infinitely extending medium (semi-infinite medium conditions).

Instantaneous source then implies that only a limited amount of diffusant is present at the starting point of the diffusion process. The solution to the diffusion equation under this constraint results in a Gaussian function. This is the case for example when taking a limited amount of tracer in gaseous form or as a very thin-film as diffusant source. In the case of a constant source, no depletion of the diffusant at the starting point of the diffusion process occurs. Here the solution to the diffusion equation takes the form of a complementary error-function. In most cases the conditions realized in an isotope-exchange experiment can be approximated as constant source-conditions.

In this case, however, a further aspect has to be taken into account: Transfer of the diffusing species into the medium where diffusion takes place can be hindered and thus the medium's surface is initially not in equilibrium with the surrounding diffusant source. In this case one has to consider an additional exchange reaction at the boundary. In the simplest case one often assumes a linear rate-exchange between sample and diffusion source expressed by

$$-D\frac{\partial c}{\partial x} = k(c_0 - c(x = 0, t)) \tag{2.46}$$

Here c_0 is the concentration the surface would have in equilibrium with its surrounding and $c(x = 0, t)$ the time dependent diffusant concentration at the surface. k is the constant of

rate exchange.
Under these constraints and the assumption of semi-infinite medium, solving Eq. (2.45) by Laplace transformation as shown in Refs. [106,107] yields

$$\frac{c(x,t) - c_{\mathrm{bg}}}{c_{\mathrm{gas}} - c_{\mathrm{bg}}} = \mathrm{erfc}(x') - \exp(h'x' + h'^2) \cdot \mathrm{erfc}(x' + h') \tag{2.47}$$

With $x' = x/\sqrt{4Dt}$ and $h' = (k/D)\sqrt{Dt}$ and c_{bg} the background concentration of the diffusing species in the sample. t is the variable diffusion time. A comprehensive overview of techniques how to solve Eq. (2.45) under various constraints and many solutions to the diffusion equation of practical relevance are compiled in Refs. [106,107]. In solids diffusion is enabled by defects. Since there are different types of defects, there are also different diffusion mechanisms. [108] In perovskites oxides only vacancies have been observed to mediate anion- as well as cation-diffusion. Solutions to Eq. (2.47) can thus serve as the mathematical framework to gain knowledge about the behaviour of vacancies in perovskites. To correctly interpret the diffusion parameter obtained, one has to distinguish two physical fundamentally different diffusion processes discriminated by their inherent driving forces:

Tracer diffusion

Tracer diffusion is characterized by the absence of any gradients in the chemical potential of the diffusing species i. Its movement is purely entropic in origin. Tracer diffusion can be measured by following the movement of a chemical identical, but physically different isotope i^*. This means that only gradients in tracer concentration are equilibrated by the random movement of atoms. Since this movement is in case of oxygen facilitated by oxygen vacancies, the corresponding tracer diffusion coefficient D^* can be expressed as

$$D^* = f^* D_V [\mathrm{V}_{\mathrm{O}}^{\bullet\bullet}] \tag{2.48}$$

Here f^* is the tracer correlation factor, a constant in the order of 1 taking deviations from pure random walk into account. D_{V} is the diffusivity of oxygen vacancies and $[\mathrm{V}_{\mathrm{O}}^{\bullet\bullet}]$ their concentration. As both D_V and $[\mathrm{V}_{\mathrm{O}}^{\bullet\bullet}]$ may possess Arrhenius-type temperature dependencies, both the activation enthalpy for the generation (ΔH_{gen}) as well as for the migration (ΔH_{mig}) of oxygen vacancies is part of the activation enthalpy of oxygen tracer diffusion:

$$D_O^*(T) = f^* [\mathrm{V}_{\mathrm{O}}^{\bullet\bullet}]^\circ \exp(\frac{-\Delta H_{\mathrm{gen}}}{\mathrm{k_B} T}) D_{\mathrm{V}}^\circ \exp(\frac{-\Delta H_{\mathrm{mig}}}{\mathrm{k_B} T}) \tag{2.49}$$

With $[\mathrm{V}_{\mathrm{O}}^{\bullet\bullet}]^\circ]$ and D_{V}° being the pre-exponential factors of the respective Arrhenius dependencies generation and migration.

$$\Delta H_{\mathrm{D}^*} = \Delta H_{\mathrm{mig}} + \Delta H_{\mathrm{gen}} \tag{2.50}$$

For many perovskites $[\mathrm{V}_{\mathrm{O}}^{\bullet\bullet}]$ (cf. Fig. 2.5) is constant over a large temperature range(cf. Fig. 2.5 for $SrTiO_3$), which allows for measuring ΔH_{mig} by means of tracer diffusion experiments.

Another consequence of Eq. (2.48) is the dependence of D^* on the oxygen activity. According to Eq. (2.25) oxygen is in- or excorporated from the sample and thereby altering the oxygen vacancy concentration. This enables gaining knowledge about a material's defect chemistry by conducting tracer-diffusion experiments as a function of oxygen partial pressure. Not only enables the dependence D^* on $[V_O^{\bullet\bullet}]$ to gain knowledge about global defect properties, it also facilitates the ability to resolve laterally varying distributions of $[V_O^{\bullet\bullet}]$ and thus uncovering of for instance space charge layers. [69]

Chemical diffusion

Chemical diffusion occurs only in the presence of gradients in the chemical potential of species. For this reason the diffusion process always results in a change in composition of a sample. In order to preserve charge neutrality in the case chemical diffusion occurs in an ionic solids, it is imperative that the diffusion of one charged species is compensated for by an accompanying process involving an oppositely charged moiety.

2.5.2 Diffusion and extended defects

Diffusion along the open structure of extended defects is generally believed to be faster than in the densely packed lattice of bulk material. This view is supported by experiment primarily conducted on metallic systems, the first of which were conducted by R.S. Barnes in the 1950. [109] Initiated by these experiments a theoretical framework for both diffusion along dislocations [110,111] as well as diffusion in the presence of grain-boundaries [112,113] has been established.
Both concepts have the classification into three characteristic regimes according to Harrison [114] in common:

Harrison Type A This regime is characterized by the fact that "every diffusing particle has wandered sufficiently far to have entered, migrated in, and left a large number of dislocations before any experimental measurement is made" [114]. This is the case for long diffusion times or lengths and when diffusion coefficients in the bulk and the defect have similar values. In measured tracer diffusion profiles the influence of extended defects is not recognizable, because the diffusion length in the defect and the bulk are of similar magnitude (Fig. 2.8).

Harrison Type B Harrison type B behaviour is observed when the diffusion length is of the same order as the dislocation network's scale. In this cases the tracer concentration distribution is not uniform and complex diffusion profiles will be observed. In most cases two distinct parts can be observed in the resulting diffusion profiles, one corresponding to classical Fickian diffusion, the other resulting from coupled bulk and grain boundary diffusion (see Fig. 2.7).

Harrison Type C In the case of short diffusion times or the diffusion coefficient in the grain boundary being much larger than in the adjacent bulk material, diffusion in the

indisturbed crystal lattice can be regarded as frozen in. Then diffusion only occurs along extended defects and only one diffusion coefficient is observed, in this case describing diffusion along the extended defect.

In tpye A and type C regime, the influence of extended defects is not obvious and profiles can be interpreted with solution to Ficks second law. Only knowledge about the existence and the influence of extended defects leads to the correct interpretation of diffusiond data in these cases. Only for specific combinations of diffusion coefficients in the bulk- and grain-boundary part of the material and certain diffusion times, the influence of extended defects is directly visible in the diffusion profiles. This is the type B regime. For fast diffusion along dislocation pipes as well as for grain-boundary diffusion there exist separate frameworks to evaluate experimental data corresponding to Harrison type B diffusion. In that manner lattice as well as defect diffusion coefficients can be reliably determined. The starting point of the evaluation of grain-boundary diffusion profiles is a plot of the measured intensity of the diffusing species [diff.] versus the diffusion depth $x^{6/5}$. In the case of dislocation pipe diffusion the intensity is plotted linearly versus x. Experimentally observed diffusion tails however cannot always be assigned to one or the other type of behaviour with a 100% certainty. This ambiguity in interpretation can be resolved by looking at the characteristic time dependencies of the diffusion tail's slopes in both cases.

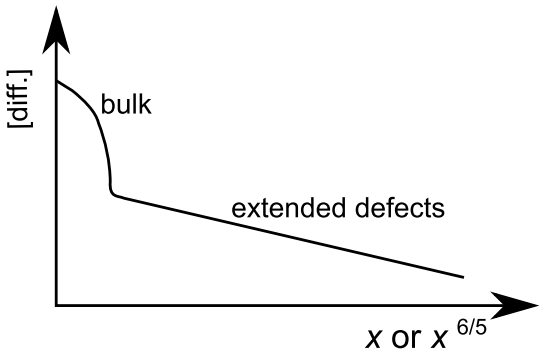

Figure 2.7: Schematic diffusion profile for either grain-boundary ($\propto x^{6/5}$) or dislocation pipe ($\propto x$) diffusion in the Harrison-type B regime.

For grain-boundary diffusion the slope is a function of diffusion time and should follow Eq. (2.51). For dislocation pipe diffusion on the other hand, the slope $\frac{\partial[\text{diff.}]}{\partial x}$ versus t should remain constant. In Eq. (2.51) D_{bulk} is the bulk diffusion coefficient and D_{GB} the respective value in the grain-boundary, t is the diffusion time. δ is the grain-boundary width, typically in the order of $\delta = 1\,\text{nm}$

$$\frac{\partial[\text{diff.}]}{\partial x^{6/5}} = \left(\frac{1.322}{\delta} \cdot \frac{\sqrt{D_{\text{bulk}}}}{D_{\text{GB}}}\right) t^{-0.3} \tag{2.51}$$

A further difficulty afflicted with the interpretation of diffusion data is the distinction of Harrison type B against the A and C regime. In the case of grain-boundary diffusion one condition for Harrison type B is that the dimensionless parameter β is large enough, typically $\beta > 10$ has to hold.

$$\beta = \frac{D_{\text{GB}}}{D_{\text{bulk}}} \frac{\delta}{2\sqrt{D_{\text{bulk}} t}} \tag{2.52}$$

The physical meaning of β is best illustrated in connection with the grain-boundary angle

α_{GB}. α_{GB} is defined as the angle between the grain-boundary and a the tangent to a contour of constant concentration (see Fig. (2.8)). Le Claire[112] derived the following connection between β and α_{GB}:

$$\cot(\alpha_{GB}) = \frac{\sqrt{\beta}}{\pi^{1/4}} \tag{2.53}$$

With increasing diffusion time, the grain boundary angle α_{GB} becomes less acute and thus β smaller. At long diffusion times or small differences between grain-boundary and bulk diffusion coefficients the grain-boundary angle becomes obtuse and bulk and grain-boundary diffusion can no longer be discernined. The practical condition of $\beta > 10$ suggests a $\alpha_{GB} < 68°$. Thus both values α_{GB} and β can be used to validate an analysis of diffusion data according to the above described model of grain-boundary diffusion.

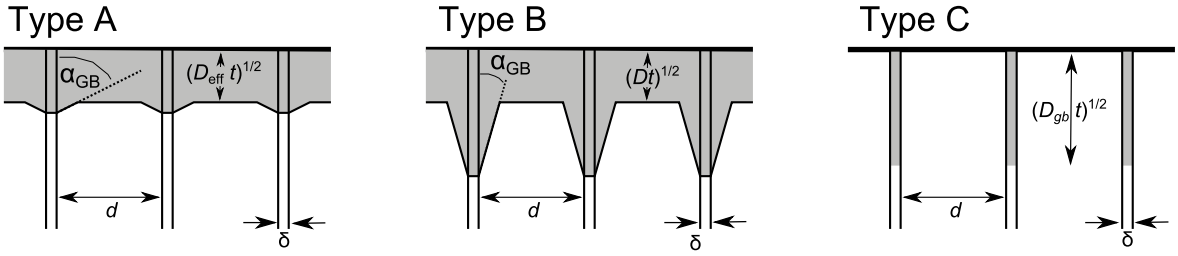

Figure 2.8: Visualisation of the different regimes for grain-boundary diffusion as classified by Harrison. In the Type A regime, the grain-boundary angle α_{GB} is large. This is either because bulk- and grain-boundary diffusion coefficients are similar or diffusion times are very long. In either case both processes can hardly be distinguished. In the Type B regime α_{GB} is small, because the diffusion process in the bulk is much slower than in the grain-boundary or the diffusion time is sufficiently short. In Type C regime bulk-diffusion is considered to be negligible. Hence not grain-boundary angle can be defined.

Bibliography

[1] G. Rose, *De novis quibusdam fossilibus quae in montibus Uraliis inveniuntur*, typis AG Schadii, 1839.
[2] K. Knox, *Acta Crystallogr.*, 1961, **14**, 583–585.
[3] T. Sato, D. Noreus, H. Takeshita and U. Häussermann, *J. Solid State Chem.*, 2005, **178**, 3381 – 3388.
[4] T. He, Q. Huang, A. Ramirez, Y. Wang, K. Regan, N. Rogado, M. Hayward, M. Haas, J. Slusky, K. Inumara *et al.*, *Nature*, 2001, **411**, 54–56.
[5] M. Pena and J. Fierro, *Chem. Rev.*, 2001, **101**, 1981–2018.
[6] A. Bhalla, R. Guo and R. Roy, *Mater. Res. Innov.*, 2000, **4**, 3–26.
[7] S.-G. Lim, S. Kriventsov, T. N. Jackson, J. Haeni, D. Schlom, A. Balbashov, R. Uecker, P. Reiche, J. Freeouf and G. Lucovsky, *J. Appl. Phys.*, 2002, **91**, 4500–4505.
[8] G. Jonker, *Physica*, 1954, **20**, 1118–1122.
[9] K. Sreedhar, J. M. Honig, M. Darwin, M. McElfresh, P. M. Shand, J. Xu, B. C. Crooker and J. Spalek, *Phys. Rev. B*, 1992, **46**, 6382–6386.
[10] J. G. Bednorz and K. A. Müller, *Angew. Chem.*, 1988, **100**, 757–770.
[11] S.-E. Park and T. R. Shrout, *J. Appl. Phys.*, 1997, **82**, 1804–1811.
[12] J. M. D. Coey, M. Viret and S. von Molnar, *Adv. Phys.*, 1999, **48**, 167–293.
[13] J. Wang, J. Neaton, H. Zheng, V. Nagarajan, S. Ogale, B. Liu, D. Viehland, V. Vaithyanathan, D. Schlom, U. Waghmare *et al.*, *Science*, 2003, **299**, 1719–1722.
[14] S. J. Skinner and J. A. Kilner, *Mater. Today*, 2003, **6**, 30–37.
[15] T. Ishihara, H. Matsuda and Y. Takita, *J. Am. Chem. Soc.*, 1994, **116**, 3801–3803.
[16] K. Kreuer, *Solid State Ionics*, 1999, **125**, 285 – 302.
[17] K. Kreuer, *Annu. Rev. Mater. Res.*, 2003, **33**, 333–359.
[18] S. Stramare, V. Thangadurai and W. Weppner, *Chem. Mater.*, 2003, **15**, 3974–3990.
[19] Y. Inaguma, L. Chen, M. Itoh and T. Nakamura, *Solid State Ionics*, 1994, **70-71, Part 1**, 196 – 202.
[20] H. Kawai and J. Kuwano, *J. Electrochem. Soc.*, 1994, **141**, L78–L79.
[21] K. R. Kendall, C. Navas, J. K. Thomas and H.-C. zur Loye, *Solid State Ionics*, 1995, **82**, 215 – 223.
[22] F. W. Poulsen and N. van der Puil, *Solid State Ionics*, 1992, **53-56, Part 2**, 777 – 783.
[23] *Perovskite Oxide for Solid Oxide Fuel Cells*, ed. T. Ishihara, Springer, 2009.
[24] B. V. Lotsch, *Angew. Chem. Int. Ed.*, 2014, **53**, 635–637.
[25] A. Sawa, *Mater. Today*, 2008, **11**, 28 – 36.
[26] R. Waser, R. Dittmann, G. Staikov and K. Szot, *Adv. Mater.*, 2009, **21**, 2632–2663.
[27] V. M. Goldschmidt, F. Ulrich and T. Barth, *Norsk. Vid. Akad., Math.-Naturvid. Kl*, 1925, **5**, 1–24.
[28] R. D. Shannon and C. T. Prewitt, *Acta Crystallogr., Sect. B: Struct. Sci*, 1969, **25**, 925–946.
[29] F. Galasso, R. Smoluchowski and N. Kurti, *Structure, Properties and Preparation of Perovskite-Type Compounds: International Series of Monographs in Solid State Physics*, Elsevier Science, 2013.
[30] R. S. Roth, *J. Res. Nat. Bur. Stand*, 1957, **58**, 75–88.
[31] J. J. Randall and R. Ward, *J. Am. Chem. Soc.*, 1959, **81**, 2629–2631.
[32] C. W. Jones, P. D. Battle, P. Lightfoot and W. T. A. Harrison, *Acta Crystallogr., Sect. C: Cryst. Struct. Commun.*, 1989, **45**, 365–367.
[33] B. J. Kennedy and B. A. Hunter, *Phys. Rev. B*, 1998, **58**, 653–658.
[34] K. J. Choi, S. H. Baek, H. W. Jang, L. J. Belenky, M. Lyubchenko and C.-B. Eom, *Adv. Mater.*, 2010, **22**, 759–762.
[35] J. Junquera and P. Ghosez, *Nature*, 2003, **422**, 506–509.
[36] V. Nagarajan, J. Junquera, J. Q. He, C. L. Jia, R. Waser, K. Lee, Y. K. Kim, S. Baik, T. Zhao, R. Ramesh, P. Ghosez and K. M. Rabe, *J. Appl. Phys.*, 2006, **100**, –.
[37] Y. S. Kim, J. Y. Jo, D. J. Kim, Y. J. Chang, J. H. Lee, T. W. Noh, T. K. Song, J.-G. Yoon, J.-S. Chung, S. I. Baik, Y.-W. Kim and C. U. Jung, *Appl. Phys. Lett.*, 2006, **88**, 072909.
[38] E. Y. Tsymbal and H. Kohlstedt, *Science*, 2006, **313**, 181–183.
[39] J. P. Velev, C.-G. Duan, J. D. Burton, A. Smogunov, M. K. Niranjan, E. Tosatti, S. S. Jaswal and E. Y. Tsymbal, *Nano Lett.*, 2009, **9**, 427–432.
[40] G. Koster, L. Klein, W. Siemons, G. Rijnders, J. S. Dodge, C.-B. Eom, D. H. A. Blank and M. R. Beasley, *Rev. Mod. Phys.*, 2012, **84**, 253–298.
[41] S. C. Gausepohl, M. Lee, L. Antognazza and K. Char, *Appl. Phys. Lett.*, 1995, **67**, 1313–1315.
[42] T. Maekawa, K. Kurosaki, H. Muta, M. Uno and S. Yamanaka, *J. Alloys Compd.*, 2005, **387**, 56–59.
[43] V. J. Emery and S. A. Kivelson, *Phys. Rev. Lett.*, 1995, **74**, 3253–3256.
[44] J. Merino and R. H. McKenzie, *Phys. Rev. B*, 2000, **61**, 7996–8008.
[45] K. Fujioka, J. Okamoto, T. Mizokawa, A. Fujimori, I. Hase, M. Abbate, H. J. Lin, C. T. Chen, Y. Takeda and M. Takano, *Phys. Rev. B*, 1997, **56**, 6380–6383.
[46] P. B. Allen, H. Berger, O. Chauvet, L. Forro, T. Jarlborg, A. Junod, B. Revaz and G. Santi, *Phys. Rev. B*, 1996, **53**, 4393–4398.

[47] D. J. Singh, *J. Appl. Phys.*, 1996, **79**, 4818–4820.
[48] I. I. Mazin and D. J. Singh, *Phys. Rev. B*, 1997, **56**, 2556–2571.
[49] W. Siemons, G. Koster, A. Vailionis, H. Yamamoto, D. H. A. Blank and M. R. Beasley, *Phys. Rev. B*, 2007, **76**, 075126.
[50] B. Dabrowski, O. Chmaissem, P. W. Klamut, S. Kolesnik, M. Maxwell, J. Mais, Y. Ito, B. D. Armstrong, J. D. Jorgensen and S. Short, *Phys. Rev. B*, 2004, **70**, 014423.
[51] W. Lu, K. He, W. Song, C.-J. Sun, G. Moog Chow and J.-s. Chen, *J. Appl. Phys.*, 2013, **113**, –.
[52] G. Herranz, V. Laukhin, F. Sánchez, P. Levy, C. Ferrater, M. V. García-Cuenca, M. Varela and J. Fontcuberta, *Phys. Rev. B*, 2008, **77**, 165114.
[53] G. Herranz, B. Martínez, J. Fontcuberta, F. Sánchez, C. Ferrater, M. V. García-Cuenca and M. Varela, *Phys. Rev. B*, 2003, **67**, 174423.
[54] J.-P. Maria, S. Trolier-McKinstry, D. G. Schlom, M. E. Hawley and G. W. Brown, *J. Appl. Phys.*, 1998, **83**, 4373–4379.
[55] C. L. Chen, Y. Cao, Z. J. Huang, Q. D. Jiang, Z. Zhang, Y. Y. Sun, W. N. Kang, L. M. Dezaneti, W. K. Chu and C. W. Chu, *Appl. Phys. Lett.*, 1997, **71**, 1047–1049.
[56] A. Kanbayasi, *J. Phys. Soc. Jpn.*, 1976, **41**, 1876–1878.
[57] C. Eom, R. Cava, R. Fleming, J. M. Phillips, J. Marshall, J. Hsu, J. Krajewski and W. Peck, *Science*, 1992, **258**, 1766–1769.
[58] G. Cao, S. McCall, J. Bolivar, M. Shepard, F. Freibert, P. Henning, J. E. Crow and T. Yuen, *Phys. Rev. B*, 1996, **54**, 15144–15148.
[59] Z. Sefrioui, D. Arias, M. A. Navacerrada, M. Varela, G. Loos, M. Lucía, J. Santamaría, F. Sánchez-Quesada and M. A. López de la Torre, *Appl. Phys. Lett.*, 1998, **73**, 3375–3377.
[60] H. Schmalzried and A. Navrotsky, *Festkörperthermodynamik. Chemie des festen Zustands*, Verlag Chemie GmbH, 1975.
[61] J. Maier, *Angew. Chem.*, 1993, **105**, 333–354.
[62] H. Tuller and S. Bishop, *Annu. Rev. Mater. Sci.*, 2011, **41**, 369–398.
[63] F. Kröger and H. Vink, *Solid state physics*, 1956, **3**, 307–435.
[64] R. A. De Souza, S. M. Islam and E. Ivers-Tiffee, *J. Mater. Chem.*, 1999, **9**, 1621–1627.
[65] N. Eror and U. Balachandran, *J. Solid State Chem.*, 1981, **40**, 85–91.
[66] B. Tofield and W. Scott, *J. Solid State Chem.*, 1974, **10**, 183 – 194.
[67] Q. Huang, A. Santoro, J. W. Lynn, R. W. Erwin, J. A. Borchers, J. L. Peng and R. L. Greene, *Phys. Rev. B*, 1997, **55**, 14987–14999.
[68] R. Moos and K. Hardtl, *J. Am. Ceram. Soc.*, 2005, **80**, 2549–2562.
[69] R. A. De Souza, V. Metlenko, D. Park and T. E. Weirich, *Phys. Rev. B*, 2012, **85**, 174109.
[70] L. Walters and R. Grace, *J Phys. Chem. Solids*, 1967, **28**, 239 – 244.
[71] A. Paladino, L. Rubin and J. Waugh, *J. Phys. Chem. Solids*, 1965, **26**, 391 – 397.
[72] I. Denk, W. Münch and J. Maier, *J. Am. Ceram. Soc.*, 1995, **78**, 3265–3272.
[73] I. Denk, F. Noll and J. Maier, *J. Am. Ceram. Soc.*, 1997, **80**, 279–285.
[74] M. Leonhardt, J. Jamnik and J. Maier, *Electrochem. Solid-State Lett.*, 1999, **2**, 333–335.
[75] M. Leonhardt, R. De Souza, J. Claus and J. Maier, *J. Electrochem. Soc.*, 2002, **149**, J19.
[76] C.-J. Shin, H.-I. Yoo and C.-E. Lee, *Solid State Ionics*, 2007, **178**, 1081 – 1087.
[77] M. J. Rozenberg, M. J. Sánchez, R. Weht, C. Acha, F. Gomez-Marlasca and P. Levy, *Phys. Rev. B*, 2010, **81**, 115101.
[78] J. Maier, *Physical chemistry of ionic materials: ions and electrons in solids*, John Wiley & Sons, 2004.
[79] J. Maier, *Angew. Chem.*, 1993, **105**, 558–571.
[80] D. Smyth, *The Defect Chemistry of Metal Oxides*, Oxford University Press, 2000.
[81] S. Hoffmann-Eifert, in *Electronic Oxides — Correlation Phenomena, Exotic Phases and Novel Functionalities*, ed. S. Blügel, T.Brückel, R. Waser and C. M. Schneider, Forschungszentrums Jülich GmbH, 2010, ch. A12, pp. A12.1–A12.27.
[82] J. M. Blakely, *Introduction to the Properties of Crystal Surfaces*, Pergamon Press, 1973.
[83] A. W. Adamson and A. P. Gast, *Physical Chemistry of Surfaces*, John Wiley & Sons, 1967.
[84] C. Kittel, *Einführung in die Festkörperphysik*, Oldenbourg Verlag, 2013.
[85] G. Gottstein, *Physical foundations of materials science*, Springer Berlin, 2004.
[86] J. P. Hirth and J. Lothe, *Theory of dislocations*, John Wiley & Sons, 1982.
[87] R. Meyer, *Modellierung transienter Vorgänge in donatordotiertem Strontiumtitanat*, VDI-Verlag, 2002.
[88] F. Gunkel, *The role of defects at functional interfaces between polar and non-polar perovskite oxides*, Forschungszentrum Jülich, 2013.
[89] R. A. De Souza, to be published.
[90] R. Moos, W. Menesklou and K. Härdtl, *Appl. Phys. A*, 1995, **61**, 389–395.
[91] T. Tanaka, K. Matsunaga, Y. Ikuhara and T. Yamamoto, *Phys. Rev. B*, 2003, **68**, 205213.
[92] R. Waser, *Z. Naturforschung A*, 1987, **42**, 1357–1365.

[93] M. J. Akhtar, Z.-U.-N. Akhtar, R. A. Jackson and C. R. A. Catlow, *J. Am. Ceram. Soc.*, 1995, **78**, 421–428.
[94] T. Bieger, J. Maier and R. Waser, *Solid State Ionics*, 1992, **53-56, Part 1**, 578 – 582.
[95] R. A. De Souza, F. Gunkel, S. Hoffmann-Eifert and R. Dittmann, *Phys. Rev. B*, 2014, **89**, 241401.
[96] J. Frenkel, *Kinetic Theory of Liquids*, Dover, 1955.
[97] K. Lehovec, *J. Chem. Phys.*, 1953, **21**, 1123–1128.
[98] R. A. De Souza, *Phys. Chem. Chem. Phys.*, 2009, **11**, 9939–9969.
[99] R. A. De Souza and M. Martin, *Phys. Chem. Chem. Phys.*, 2008, **10**, 2356–2367.
[100] M. Minohara, I. Ohkubo, H. Kumigashira and M. Oshima, *Appl. Phys. Lett.*, 2007, **90**, –.
[101] V. E. Henrich, G. Dresselhaus and H. J. Zeiger, *Phys. Rev. B*, 1978, **17**, 4908–4921.
[102] G. W. Dietz, W. Antpöhler, M. Klee and R. Waser, *J. Appl. Phys.*, 1995, **78**, 6113–6121.
[103] E. H. Rhoderick and R. Williams, *Metal-semiconductor contacts*, Clarendon Press Oxford, 1988, vol. 2.
[104] H. Lüth, *Solid surfaces, interfaces and thin films*, Springer, 2001, vol. 4.
[105] H. Mehrer, *Diffusion in solids: fundamentals, methods, materials, diffusion-controlled processes*, Springer, 2007, vol. 155.
[106] J. Crank, *The Mathematics Of Diffusion*, Claredon Press, Second Edition edn., 1975.
[107] H. Carslaw and J. Jaeger, *Conduction of Heat in Solids*, Clarendon Press, 1986.
[108] *Diffusion in Condensed Matter*, ed. P. Heitjans and J. Kärger, Springer, 2005.
[109] R. S. Barnes, *Nature*, 1950, 1032–1033.
[110] A. Le Claire and A. Rabinovitch, *J. Phys. C Solid State*, 1981, **14**, 3863.
[111] A. D. Le Claire and A. Rabinovitch, *J. Phys. C Solid State*, 1982, **15**, 3455.
[112] A. Le Claire, *Philos. Mag.*, 1951, **42**, 468–474.
[113] A. D. Le Claire, *Br. J. Appl. Phys.*, 1963, **14**, 351.
[114] L. G. Harrison, *Trans. Faraday Soc.*, 1961, **57**, 1191–1199.

Chapter 3

Experimental Methods

In this section, the different experimental techniques employed in this work are presented. First, the methods used to characterise thin film heterostructures are depicted. Subsequently the routine utilised to produce these heterostructure samples is introduced. In this context the characterisation techniques will be applied to assess the the success of the preparation routine. This assessment is based on benchmarks derived from literature data.
As a setup to conduct isotope exchange experiments was constructed as part of this work, this technique and the corresponding "isotope exchange rig" is addressed in the second part of this chapter in a more detailed fashion. In the same section the technique of secondary ion mass spectrometry (SIMS) is also introduced with the main focus on depth profiling of oxide heterostructures. Lastly, in this chapter, different methods used only occasionally in this work are presented.

3.1 Characterization Methods

To ensure that the prepared samples possess the desired properties, certain benchmarks for reliable comparison with literature data. Typical criteria are the sample's surface morphology — characterized by means of atomic force microscopy (AFM) — and the sample's crystal structure — evaluated by means of X-ray diffraction (XRD). The working principle of those techniques is described in the following.

3.1.1 Atomic Force Microscopy (AFM)

In an atomic force microscope the displacement of a spring is employed to probe interatomic forces.[1] Typically an atomically sharp scanning tip attached to an elastic cantilever serves as a spring. Forces acting between scanning tip and sample ($F_{\mathrm{t-s}}$) (or some derivative thereof) can be used as the imaging information upon scanning the tip over the sample surface.
During this scan, the tip-sample distance is controlled with a feedback-loop and a piezo-element such that a force of constant magnitude acts between the two partners (see Fig. 3.1). In that manner a sample's topography can be probed with ultra-high precision. In many cases atomic resolution is possible.[2]

Generally the tip-sample interaction can be classified into two regimes: Repulsive forces that dominate at small and attractive forces that dominate at large tip-sample distances.

To probe the repulsive interactions, the scanning tip is brought into contact with the sample surface ("contact mode"). While moving the tip over the surface, variations in magnitude of the cantilever bending are taken as a measure of the acting force. In order to keep this force at a constant level, the tip-sample distance is varied. This variation in tip-sample distance provides the imaging information of the sample's topography.

One unfortunate disadvantage of the contact mode is that a lot of samples are susceptible to damage induced by the cantilever tip. Furthermore frictional forces might impair the information obtained. [3]

These are compelling reasons to probe the attractive forces dominating at larger tip-sample distances in the "non-contact mode". To do this, the cantilever is excited to oscillations with a frequency f close to its resonance frequency with a small amplitude ($A \approx 5\,\mathrm{nm}$). Both, f and A, are perturbed when the tip is brought in proximity to the sample surface such that long-range tip-sample interaction is enabled, but the tip does not touch the sample.

Controlling the tip-sample distance such that a constant oscillation amplitude or frequency is maintained while scanning over the sample surface then provides the desired imaging information.

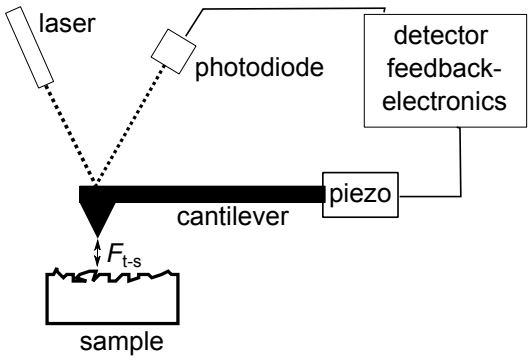

Figure 3.1: Schematic representation of an atomic force microscope. The sample's surface topography is probed by rastering a cantilever-tip its surface. A laser-photodiode system monitors changes in cantilever properties. Based on these changes a control element adjusts the tip-sample distance via a piezo element.

A major concern with this operation mode, however, is the scanning tip's sensitivity to "snapping" into contact with the sample surface. Especially under ambient conditions this poses a problem, because a typically present wetting layer of condensed water facilitates this phenomenon. [2,3]

In order to probe a surface topography under ambient conditions without damaging the sample and avoiding the cantilever tip "snapping" into contact with the sample surface, a modified version of the "non-contact mode", the so called "tapping-mode" is used: [3]

The cantilever, again, oscillates close to its resonance frequency (typically in the range of $f = 500\,\mathrm{Hz}$–$50\,000\,\mathrm{Hz}$) but with a much larger free amplitude ($A \approx 200\,\mathrm{nm}$). The scanning tip is brought close to the sample surface, such that it touches the surface every oscillation. By this intermittent contact with the sample, the oscillation amplitude is altered. The magnitude of this perturbed amplitude is then used as a set point. Upon rastering the scanning tip over the sample, the tip-sample distance is adjusted such that the oscillation amplitude remains constant. This provides the desired imaging information of the sample's topography. [3]

Depending on the mode of operation, either changes in cantilever bending or changes in

cantilever oscillation have to be detected. These changes in cantilever properties are typically monitored with the help of a laser reflected on the back of the cantilever and monitored by means of a photo diode (Fig. 3.1).

In this work an ULTRA Objective Pico Station (SiS GmbH, Herzogenrath, Germany) is used. The cantilever is excited to oscillate at a frequency of $f \approx 160\,\text{kHz}$ with a free amplitude of $A \approx 185\,\text{nm}$ (70% of free amplitude is used as setpoint amplitude). The freely available software Gwyddion [4] is employed to process and visualize the raw data acquired.

3.1.2 X-Ray Diffraction (XRD) and X-Ray Reflectivity (XRR)

X-ray diffraction (XRD) is used in this work to elucidate the structure of $SrRuO_3$ thin films with focus on probing the epitaxial relationship between film and substrate.

X-rays are focused on the sample, where they are elastically scattered by the electronic structure of the sample's constituents.

In cases where these constituents are periodically arranged, only for distinct incidence angles Θ of the X-ray beam constructive interference of the scattered waves occurs. In these cases peaks of high intensity can be observed under the angle of 2Θ (see Fig. 3.2). A plot of the observed intensity versus 2Θ — a diffractogram — is then characteristic for the periodic structure of constituents in the sample investigated. The condition for constructive interference is given by the Bragg equation (Eq. (3.1)):

$$\lambda = 2d_{(hkl)} \sin(\Theta) \qquad (3.1)$$

with λ being the wavelength of the incident X-rays and $d_{(hkl)}$ the spacing between parallel planes in the periodic structure under investigation. For a periodic arrangement of atoms in a

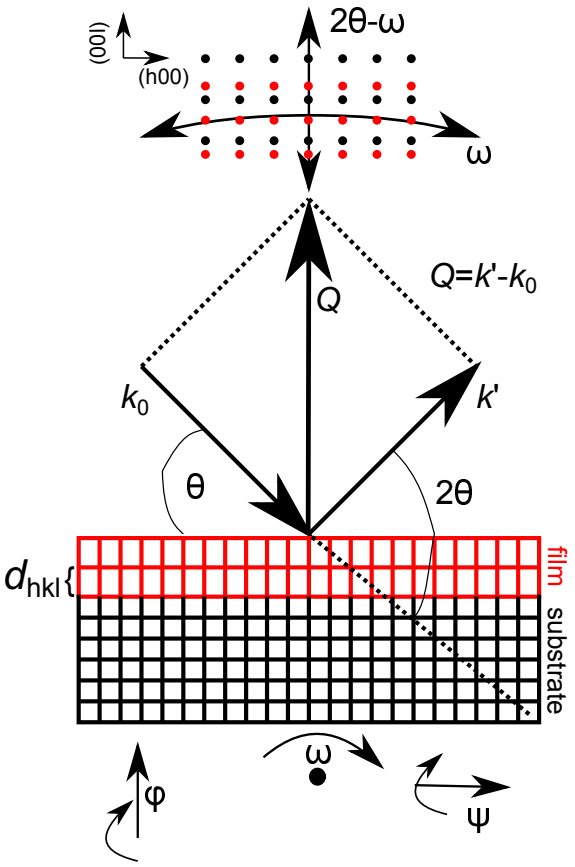

Figure 3.2: Visualization of a diffraction experiment: X-rays with wave-vector k_0 are focussed onto the hetero structure sample where they elastically scatter. The scattered wave is k'. Each time the vector of momentum transfer Q hits a reciprocal lattice point, a reflex in a diffractogram is observed. By variation (rotation around ω, ϕ, ψ or changing 2Θ) of the sample position, the angle of incidence of k_0 is changed. Therefore the length and the direction of Q are varied. This opens the possibility to probe the reciprocal lattice in different ways.

crystal with rectangular symmetry, this spacing can be expressed as

$$d_{hkl} = \left(\left(\frac{h}{a}\right)^2 + \left(\frac{k}{b}\right)^2 + \left(\frac{l}{c}\right)^2 \right)^{-1/2} \tag{3.2}$$

In Eq. (3.2) a, b, c are the unit lattice parameters and h, k, l the respective Miller indices of the lattice planes investigated. As the Miller indices h, k, l define the probed lattice planes in reciprocal space, each observed reflex can be regarded as a point in reciprocal space. To account for this fact Bragg's law can also be illustrated in reciprocal space: The incident X-rays wave with the wave vector k_0 are elastically scattered as k', hence only a change in momentum occurs. This difference in momentum is expressed by the vector of momentum transfer $Q = \frac{2\pi}{d_{hkl}} = k' - k_0$. For cases in which the Bragg equation is fulfilled the scattering vector Q hits a reciprocal lattice point and a reflex is observed. This means that in order to probe the reciprocal lattice and thus elucidate the crystal structure one has to vary Q. considering a fixed wavelength and thus a fixed absolute value of k_0, this can only be achieved by changing k_0's angle of incidence. Modern instruments allow for this by rotating the sample in all three dimensions (around the axis ω, ϕ, ψ) and moving the detector around 2Θ.

For a coupled a coupled $2\Theta - \omega$ scan the detector and sample are moved such that the length of Q is changed in one direction. This kind of scan, however, does not provide any information about the extension of the reciprocal lattice points perpendicular to the investigated direction. To retrieve this information, the sample is moved around ω ("rocking-curve" or ω-scan) so that Q does not vary in length, but the extent of the lattice point in reciprocal space is probed (cf. Fig. 3.2). The FWHM of such a scan is generally considered as an indicator of the film's crystal quality. To probe entire areas in reciprocal space, $2\Theta - \omega$ and ω scans can be combined to retrieve reciprocal space maps (RSM). This allows for elucidating epitaxial relationships between film and substrate in cases in cases where $2\Theta - \omega$ don not allow for probing in-plane relationships (cf. Fig. 3.2).

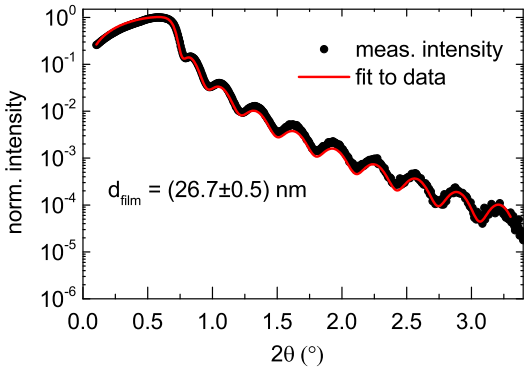

Figure 3.3: The results of a typical XRR-measurement of an $SrRuO_3$-film on top of a $SrTiO_3$ substrate. For the simulation the film thickness as well as surface- and interface roughness were assumed as free parameters. The fit is regarded to be of sufficient quality when a figure of merit (FOM) FOM $\leq$ 0.1 is obtained.

In this work reciprocal space maps around the $SrTiO_3$ (103)-reflex are conducted. In that manner the lattice parameters of the grown $SrRuO_3$ films in relation to those of the $SrTiO_3$ substrate are measured.

Fitting of the obtained ω- and $2\Theta - \omega$-scans was done using the software Fityk [5]. To process data of reciprocal space maps the software Origin (OriginLab, Northampton, MA, USA) was used.

A further method used in this work is X-ray reflectometry (XRR). It is used to reliably determine the thickness of films thinner than $d_{\text{film}} \leq 60\,\text{nm}$. In contrast to visible light, for X-rays the refractive index of solid materials is $n \leq 1$. For this reason below a critical angle ϕ_c X-rays are totally reflected by a thin film sample. For angles $2\Theta \geq \phi_c$ x-rays partly penetrate into the sample and are partly reflected by the surface and the film-substrate interface. These reflected rays interfere with each other. Upon variation of 2Θ interference maxima and minima are observed. The distance of these maxima and minima is determined by the film's thickness. A typical XRR diffractogram is depicted in Fig. (3.3). The software GenX [6] was used to fit the obtained XRR-data. In writing this section, Refs. [7–9] have been consulted, as they provide a comprehensive introduction into this topic. All diffractograms were recorded on a 4-circle goniometer equipped with a $\text{CuK}_{\text{alpha}}$ X-ray source (X'Pert PRO MRD, PANalytical B.V, Almelo, The Netherlands).

3.2 Thin film growth

3.2.1 Pulsed Laser Deposition (PLD)

In the zoo of techniques [10,11] used to produce epitaxial thin films on a crystalline substrate, pulsed laser deposition (PLD) is one of the most frequently applied as it allows for a comparably fast and easy film production of complex materials. [12,13] The rise of PLD was triggered by the deposition of high-quality, stoichiometric thin films of high-T_C superconductors in the 1980s. [14] Nowadays, the understanding of the method matured so far that production of atomically sharp interfaces and superlattices has become commonplace. [15]

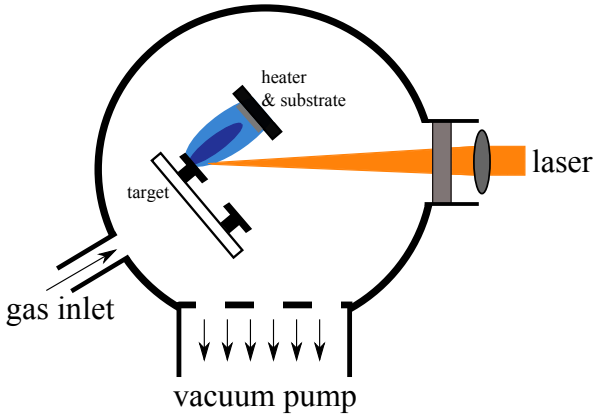

Figure 3.4: Principle of pulsed laser deposition (PLD): A laser is focussed on a rotating target where it ablates material and transfers it into a plasma. A heated substrate is placed into the emerging plasma plume. On the substrate the plasma condenses and a film grows.The growth process can be conducted in different gas atmospheres. In this work oxygen is used.

The basic principle of PLD is sketched in Fig. 3.4: A short pulsed laser beam is focused down to a high energy density (fluence J_{L}) onto a single or polycrystalline target, placed in a vacuum chamber with a defined gas atmosphere. The laser energy is absorbed by the target material and converted into thermal, chemical and mechanical energy. This leads to a rapid removal of target material, which is ejected as a plasma plume expanding in a flow perpendicular to the target surface. This plasma plume contains charged and neutral species of the target material and its composition is in first order independent of different melting points of the target compounds. For this reason a stoichiometric transfer of target material onto a substrate placed in the plasma plume is feasible.

Typically the substrate is placed several centimeters away from the target and the plasma species are thermalised in a background gas before condensing on the substrate with an average kinetic energy of several eV. On the substrate the collected species can diffuse, cluster or desorb again. All processes eventually result in the growth of a thin film. This growth process can occur in different modes that are strongly dependent on the pressure p and the kind of background gas used (for the growth of oxides oxygen is most frequently used), the temperature the substrate is held at (T_{subs}) and of course the laser fluence J_{L} the material was ablated with. Furthermore the distance of the substrate relative to the target $d_{\mathrm{s-t}}$ and the repetition rate of the laser pulses f have a strong impact on the film properties. In this work a PLD setup (Neocera Inc, College Park, Maryland, USA) equipped with a KrF eximer laser (LPX305, Lambda Physik, Germany) with a wavelength of $\lambda = 248\,\mathrm{nm}$ and pulse duration of $t_{\mathrm{pulse}} = 20\,\mathrm{ns}$ is used. The substrate target distance of the setup is fixed to $d_{\mathrm{s-t}} = 7.5\,\mathrm{cm}$. The substrate is glued onto a stainless steel heater with silver paste. The temperature of the heater is measured and controlled and in the following referred to as the substrate temperature T_{S}.[1] The oxygen partial pressure $p\mathrm{O}_2$ in the system is adjusted with mass flow contollers.

3.2.2 $SrTiO_3$ substrate preparation

For the growth of high quality, epitaxial thin films a vicinal surface structure of the used substrates is indispensable. The crystal is typically cut at a characteristic angle and the surface is then constituted of a train of steps of one unit cell in height. In the as-received state, the purchased (Crystec GmbH, Berlin, Germany) $SrTiO_3$ substrates, however, exhibit a disordered surface structure. Regions of both TiO as well as of SrO surface-termination can be observed.[16] To prepare a uniform TiO-terminated surface with steps of exclusively single unit cell height, a wet-etching process in buffered hydrofluoric acid (BHF) is used:

1. **Sample cleaning:** Sonicate 3 min in acetone, then 3 min in isopropanol.

2. **$Sr(OH)_2$ formation:** Sonicate 3 min in demin. water; the corresponding reaction is

$$\mathrm{SrO} + \mathrm{H_2O} \rightleftharpoons \mathrm{Sr(OH)_2} \tag{3.3}$$

3. **Removal of $Sr(OH)_2$:** Rinse the sample for $t_{\mathrm{etch}} = 150\,\mathrm{s}$ in BHF ($p\mathrm{H} = 6.5$)

$$\mathrm{Sr(OH)_2} + 2\mathrm{HF} \rightleftharpoons \mathrm{SrF_2} + 2\mathrm{H_2O} \tag{3.4}$$

4. **Removal of SrF_2:** Sonicate 3 min in acetone, then 3 min in isopropanol.

5. **Annealing:** 2 h at $T_{\mathrm{anneal}} = 1223\,\mathrm{K}$

[1] There will be a small difference between the actual temperature at the sample surface and that adjusted by the controller. As all samples used in this study were deposited with the same heater, this difference is of no practical relevance.

This procedure is based on Refs. [16,17]. The way it is conducted conducted in this work, was proposed among others in Refs. [18,19].

3.2.3 Growth of thin film $SrRuO_3$

In the preceding section, it was stated that upon arrival on the substrate the ablated species (adatoms) can diffuse, cluster and desorb and it is these three processes that determine the growth behaviour of the growing thin film. For the growth of $SrRuO_3$ three fundamentally different modes have been observed resulting in epitaxial thin films[20]: 1. STEP-FLOW: Here the adatoms and small clusters thereof diffuse to the step edges of the substrate, resulting in a persistent advancement of the vicinal steps. 2. STEP-BUNCHING: Adatoms still diffuse to the step edges, but with their advancement these steps increasingly interact with each other and coalescence of several steps to large terraces occurs. 3. ISLAND-GROWTH: Here the mutual interaction of adatoms results in island formation and coalescence of the islands. In that way the film is formed layer by layer. For $SrRuO_3$ the parameter space covering all three growth regimes was characertized theoretically and experimentally by Hong *et al.*.[20] The two decisive parameters are the deposition flux and the step length of the vicinal substrates used. The deposition flux is the amount of material arriving on the substrate per unit time and thus represented by the deposition frequency if the laser fluence is kept constant. At low deposition fluxes and small step length, interaction forces between the advancing steps dominate and step bunching occurs.

With increasing deposition flux and step length these energetic interaction forces become less dominant and kinetic phenomena prevail. Now adatoms diffuse without interaction to the step edges and ideal step-flow film growth occurs. Using too high deposition fluxes or too long step edges, however, increases the probability of adatom interaction and island formation, thus island growth dominates. To put it briefly, in order for the desired step-flow growth mode to be persistent, one has to find the right combination of deposition frequency and vicinal angle.

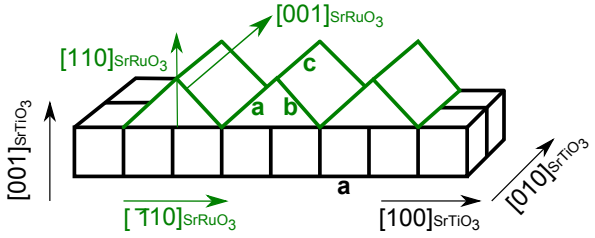

Figure 3.5: Orientation relationship of an $SrRuO_3$-film on a (100) oriented $SrTiO_3$ substrate. The film growth with a (110) texture with the [001] and [$\bar{1}$10] direction of the orthorhombic film aligned along the [100] and [010] direction of the substrate. (Sketch based on Ref. [21])

Not only are step-flow grown samples of $SrRuO_3$ desired, but the film's crystallographic orientation on the substrate can also be considered as a benchmark for successful film growth. It has been found that epitaxial films of $SrRuO_3$ exhibit a (110) texture on $SrTiO_3$ substrates. The in-plane [001] and [$\bar{1}$10] are aligned along the [100] and [010] of the substrate[22,23] (see Fig. 3.5 for illustration). Reminding oneself of the pseudo-cubic unit-cell concept of perovskites (cf. Sec. 2.1), one finds that the (110)-direction in $SrRuO_3$'s orthorhombic unit cell corresponds to the (001) pseudo-cubic direction. For this reason probing the out-of-plane

lattice constant provides information about the pseudo-cubic lattice parameter. As long as we can consider the in-plane lattice parameter being clamped to the substrate, probing the out-of-plane parameters is sufficient to characterize the crystallographic properties of our films.

The standard routine to prepare thin film $SrRuO_3$ in this study was as follows: Ablation was conducted in an oxygen atmosphere of $pO_2 = 0.133\,\text{mbar}$ ($p_{\text{base}} \leq 5 \times 10^{-5}\,\text{mbar}$) from a $SrRuO_3$ - target (99.9% purity of raw materials, Praxair S.T. Technology Inc., Indianapolis, USA) at a laser frequency of $f = 10\,\text{Hz}$ and with a fluence of $J_{\text{L}} \approx 1\,\text{J}\,\text{cm}^{-2}$ The heater-temperature was $T_{\text{Depo}} = 973\,\text{K}$. After deposition samples were cooled down to room temperature within two hours in an oxygen atmosphere of $pO_2 = 500\,\text{mbar}$.

In order to assess the quality of films deposited and facilitate comparison above described benchmarks set by previous studies, several characteristica are used. Atomic-force micrographs of as deposited films, as shown in Fig. 3.6 (a), reveal their surface morphology. The terrace structure that reflects the underlying $SrTiO_3$ substrate and occasional screw-like formations that can be attributed to threading dislocations [24] are observed; no other features can be found. Investigating larger sample areas ($50\mu\text{m} \times 50\mu\text{m}$) by means of interference microscopy reveals that the height distribution of sample surface points follows a Gaussian distribution with a full-width at half maximum ($FWHM$) of $FWHM = 1.2\,\text{nm}$ (histogram shown in Fig. 3.6 (e)).

The reciprocal space map, shown in Fig. 3.6 (b), confirms the clamping of the in-plane lattice parameter of $SrRuO_3$ to that of the $SrTiO_3$ substrate $a = (3.905 \pm 0.003)\,\text{Å}$. Furthermore an out-of-plane lattice parameter for the thin film of $c = (3.951 \pm 0.002)\,\text{Å}$ is revealed and confirmed by a conventional $2\theta - \omega$ scan (Fig. 3.6 (c)). These results are in good agreement with literature: $c = 3.96\,\text{Å}$ Ref. [25], $c = (3.9635 \pm 0.0005)\,\text{Å}$ Ref.[26]. Rocking-curve scans of the pseudo-cubic (002)-peak yielded $\Delta\omega \approx 0.028°$ (Fig. 3.6 (f)). These results indicate that the $SrRuO_3$ films are epitaxial with a high degree of crystalline quality. Furthermore they suggest that our films, as generally observed for PLD films of $SrRuO_3$, [27,28] are Ru deficient: the out-of-plane lattice parameter of our films is higher than the corresponding value for stoichiometric films (deposited by means of molecular beam epitaxy (MBE)). [28] All as-deposited samples were examined with conventional $2\theta - \omega$ scans to confirm that the out-of-plane lattice parameter, and thus the degree of Ru deficiency, remained constant for all samples.

3.3 Isotope Exchange Experiments

As first shown by Kilner *et al.* [29], introducing an oxygen-isotope profile by gas-solid exchange and subsequent depth profiling is a powerful means to reliably determine the oxygen tracer diffusion coefficient D^*_{O} and simutaneously the corresponding surface exchange coefficient k^*_{O}.

The typical course of an isotope exchange experiment consists of two steps: A pre-anneal and an exchange- (or tracer-) anneal.

The prerequisite that purely entropically driven tracer diffusion occurs during the experiment is that no gradients in the chemical potential of oxygen are a priori present in the sample

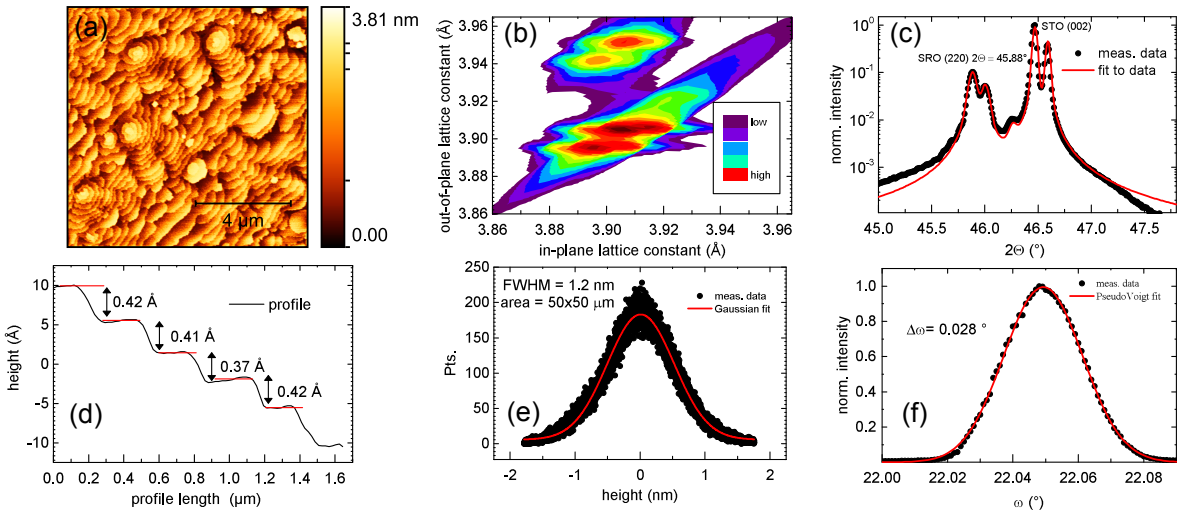

Figure 3.6: (a) Atomic Force Micrograph of the surface of an as-deposited $SrRuO_3$ thin film. The image refers to an area of $10\,\mu m \times 10\,\mu m$. Steps with the height of ca. one (pseudocubic) unit cell are clearly discernible; the root-mean-square (rms) roughness was 0.23 nm. (b) Reciprocal space map around the $SrTiO_3$ (103) peak measured for an as-deposited thin film. Double peaks are due to the X-ray source's Cu $K_{\alpha 1/\alpha 2}$ doublet. (c) $2\Theta - \omega$-scan of the (002)- $SrTiO_3$ and the (220)-$SrRuO_3$ $(002)_{pc}$ peak. From this measurement the out-of-plane lattice constant is deduced. (d) line-scan of the step-structure visible in (a) (d) Histogram of an interference microscopy measurent. It reveals that over $50\mu \times 50\mu m$ the height distribution of surface points follows a Gaussian distribution with a fullwidth at half maximum of $FWHM = 1.2\,nm$. (e) rocking-curves of the (220)-$SrRuO_3$ peak shown in (c) exhibit a width of $\Delta\omega = 0.028°$, this is only slightly above the instruments resolution of about $\Delta\omega \approx 0.02°$ measured for the (004)-reflex on a Si-wafer.

(cf. Sec. 2.5). This is ensured by exposing the sample to the first step of the experiment, the pre-anneal. The sample is exposed to the same thermodynamic conditions, that is the same temperature T and the same oxygen activity aO_2 as in the subsequent exchange experiment in oxygen of normal isotopic abundance (hereafter referred to as $^{16}O_2$-gas). In that manner all gradients in the chemical potential of oxygen in the sample are eliminated. A second purpose of the pre-anneal is to equalise any initial profile in tracer concentration on a length scale much larger than the diffusion length realized during the tracer anneal. The third purpose of the pre-anneal is to make sure that the sample surface is in a stable condition and does not significantly change during the tracer anneal.[30]

These three conditions are typically fulfilled, if the pre-anneal time t_{pre} is chosen to be one order of magnitude longer than the exchange time t_{ex}.[31,32] [2] After quenching the sample to room temperature the $^{16}O_2$ gas is replaced by oxygen, which is highly enriched of the minor isotope ^{18}O (hereafter referred to as $^{18}O_2$-gas). Now the same thermodynamic conditions as for the pre-anneal are realised again for a certain exchange time t_{ex}. Then the sample is again cooled down to room temperature.

[2] In present work the pre-anneal time is not always chosen to be one order or magnitude longer than the exchange time. This is mainly because here the pre-annealing step significantly alters the sample's properties, a process that will be addressed in more detail in Chapter 4 of this work.

During the experiment the temperature is monitored with a thermocouple placed directly at the sample and is recorded as a function of time. This allows for taking into account the ramps required for heating up to and cooling down from the set point temperature when calculating t_{pre} and t_{ex}.

The calculation of t_{pre} and t_{ex} follows a method based on publications by D. R. Killoran.[33,34] The main idea is that the diffusion process is thermally activated with a material-dependent activation enthalpy ΔH_D (cf. Sec. 2.5). For a high activation enthalpy the diffusion process during heating and cooling will be more inhibited than for a small activation enthalpy. Consequently the effective diffusion times will be shorter in the first and longer in latter case. This is illustrated in Fig. 3.7. A temperature profile of a typical exchange anneal is shown in Fig. 3.7 (a). Fig. 3.7 (b) depicts that when assuming an activation enthalpy of $\Delta H_D = 2\,\mathrm{eV}$ a much shorter diffusion time results than when assuming $\Delta H_D = 1\,\mathrm{eV}$. A further aspect this kind of analysis demonstrates is that the longer the exchange time is, the less important diffusion during heating and cooling gets and the flatter the t_{ex} vs. ΔH_D curve is. For short t_{ex}, on the other hand, the ΔH_D vs. t_{ex} curve is very steep and already slight variations in ΔH_D result in significantly different t_{ex}. As a consequence, determining ΔH_D with short tracer-exchange experiments can require the iterative determination of t_{ex} and thus ΔH_D.

As any chemical driving forces have been eliminated in the pre-anneal and just the entropic motion of oxygen is present, equal amounts of $^{18}\mathrm{O}$ and $^{16}\mathrm{O}$ are exchanged between the gas and the sample during the exchange anneal. Hence the sum of the concentrations of the different oxygen isotopes is constant in the gas as well as in the sample. This means that in principle one could probe the diffusion kinetics both ways by either measuring the tracer concentration in the gas phase in-situ[35–37] or by analysing the solid sample after completion of the exchange.[29,38–40] There is, however, one decisive drawback to the in-situ method: The surface exchange coefficient k^*_{O} and the tracer-diffusion coefficient D^*_{O} cannot always be determined simultaneously. It depends on the sample geometry, whether the surface exchange or the diffusion process dominates and which constant can reliably be determined.[35]

For this reason ex-situ analysis of "frozen-in" tracer profiles by means of Secondary Ion Mass Spectrometry (SIMS) (for details see Sec. 3.4) presents an excellent way to probe both k^*_{ex} and D^*_{ex} simultaneously.[29,38,39]

In order to facilitate a straightforward interpretation of these frozen-in profiles, due care is taken to keep the total amount of tracer exchanged so small that it is negligible compared to the total gas volume. This allows for considering the tracer concentration in the gas to be constant and to apply Dirichlet boundary conditions at the sample surface when solving the diffusion equation (cf. Sec. 2.5).

To check this assumption's validity the tracer concentration in the used gas is checked before each pre-anneal and exchange experiment by means of quadrupole mass-spectrometry (PrismaPlus QMG 220, Pfeiffer Vacuum GmbH, Asslar, Germany). The isotopic abundances are checked by monitoring the biatomic species of oxygen and calculating the abundances. Here Refs.[41] and references therein were taken as a guideline.

The basic idea is to derive isotope abundances from measured isotope ratios. As in A.

Nier's paper,[41] in this work the intensity ratios ${}^{17}R = {}^{17}\mathrm{O}^{16}\mathrm{O}/{}^{16}\mathrm{O}^{16}\mathrm{O}$ as well ${}^{18}R = {}^{18}\mathrm{O}^{16}\mathrm{O}/{}^{16}\mathrm{O}^{16}\mathrm{O}$ were measured.

The percentance isotope abundance abundance for ${}^{17}\mathrm{O}$ and ${}^{18}\mathrm{O}$ are defined as

$$n_{{}^{17}\mathrm{O}} = \frac{{}^{17}\mathrm{O}}{{}^{16}\mathrm{O} + {}^{17}\mathrm{O} + {}^{18}\mathrm{O}} \quad n_{{}^{18}\mathrm{O}} = \frac{{}^{18}\mathrm{O}}{{}^{16}\mathrm{O} + {}^{17}\mathrm{O} + {}^{18}\mathrm{O}} \tag{3.5}$$

In a similar fashion, the measured intensity ratios R can be expressed

$$\begin{aligned} {}^{17}R' &= \frac{{}^{17}\mathrm{O}}{{}^{16}\mathrm{O}} = \frac{2\,{}^{17}\mathrm{O}^{16}\mathrm{O}}{{}^{16}\mathrm{O}^{16}\mathrm{O}} \\ {}^{18}R' &= \frac{{}^{18}\mathrm{O}}{{}^{16}\mathrm{O}} = \frac{2\,{}^{18}\mathrm{O}^{16}\mathrm{O}}{{}^{16}\mathrm{O}^{16}\mathrm{O}} \end{aligned} \tag{3.6}$$

Combining Eq. (3.5) and Eq. (3.6) yields

$$\begin{aligned} n_{{}^{17}\mathrm{O}} &= \frac{{}^{17}R}{2(1 + {}^{17}R + {}^{18}R)} \\ n_{{}^{17}\mathrm{O}} &= \frac{{}^{18}R}{2(1 + {}^{17}R + {}^{18}R)} \end{aligned} \tag{3.7}$$

In this context it is noteworthy that in order to determine the minor isotopes in ${}^{18}\mathrm{O}_2$ gas, the ratios R were defined based on the major isotope ${}^{18}\mathrm{O}$ [3]. Isotopic abundances determined in the above described fashion for gases used in this work are tabulated in Table 3.1.

There are two striking aspect of the compilation in Table 3.1): 1. The isotope fractions determined in the ${}^{16}\mathrm{O}_2$-gas used are within the range of the naturally occurring variations. Here $n_{{}^{18}\mathrm{O}}$ is at the upper end of this range, a fact that is common for high-purity gases.[32] 2. The isotope abundances in the cryo-system used to recycle and store ${}^{18}\mathrm{O}_2$-gas significantly differ from those in the metal cylinder this gas delivered in. The main reason for this discrepancy is that even after extensive bake-out of the cryo-system, there is some residual ${}^{16}\mathrm{O}_2$ left in the zeolithes used for gas capture. This results in "contamination" of the ${}^{18}\mathrm{O}_2$-gas with ${}^{16}\mathrm{O}_2$.[4]

A further assumption in need for validation is the negligibility of the presence of water and thus the hydroxide incorporation during the course of the exchange experiment (in Sec. 2.3.3 we neglected this issue discussing the defect chemistry of $SrTiO_3$. In Ref.[43], for example, the incorporation reaction of hydroxide plays an important role for the defect behaviour). To measure the humidity in the gas a dew-point sensor (Easidew On-line Hygrometer, Michell Instruments,Friedrichsdorf, Germany) is employed. The measured dew-points are converted into volume fractions of water using Magnus' formula. In all experiments conducted, the water

[3] ${}^{17}R = {}^{17}\mathrm{O}^{18}\mathrm{O}/{}^{18}\mathrm{O}^{18}\mathrm{O}$ and ${}^{16}R = {}^{16}\mathrm{O}^{18}\mathrm{O}/{}^{18}\mathrm{O}^{18}\mathrm{O}$; the calculation is analogous

[4] Insufficient evacuation of the vacuum-system and the potential neglection of dead-volumina in valves can be excluded as a major contribution as the value for $n_{{}^{18}\mathrm{O}}$ remains constant within the error-margins over several recycling cycles.

Table 3.1: Isotope abundances of the two gases used in this work measured by means of quadrupole mass spectrometry. A comparison with the certificate of analysis with of the $^{18}O_2$- gas is made. The significant differences are due to the fact that the $^{18}O_2$- gas is stored in a cryo-pump-system which initially contained residual $^{16}O_2$.

	$n_{^{16}O}$ (%)	$n_{^{17}O}$ (%)	$n_{^{18}O}$ (%)
$^{16}O_2$-gas	(99.748 ± 0.003)	(0.038 ± 0.002)	(0.216 ± 0.003)
natural variation [42]	99.738–99.776	0.037–0.040	0.188–0.222
$^{18}O_2$- gas	(6.345 ± 0.016)	(1.169 ± 0.007)	(92.572 ± 0.087)
Certificate of Analysis (cylinder)	2	0.9	97.1

content was below $x_{H_2O} < 0.1\,\mathrm{ppm}_v$; this requires the dew-point to be below $\vartheta_{dew} \leq -94\,°C$ at an oxygen pressure of $pO_2 = 500\,\mathrm{mbar}$.

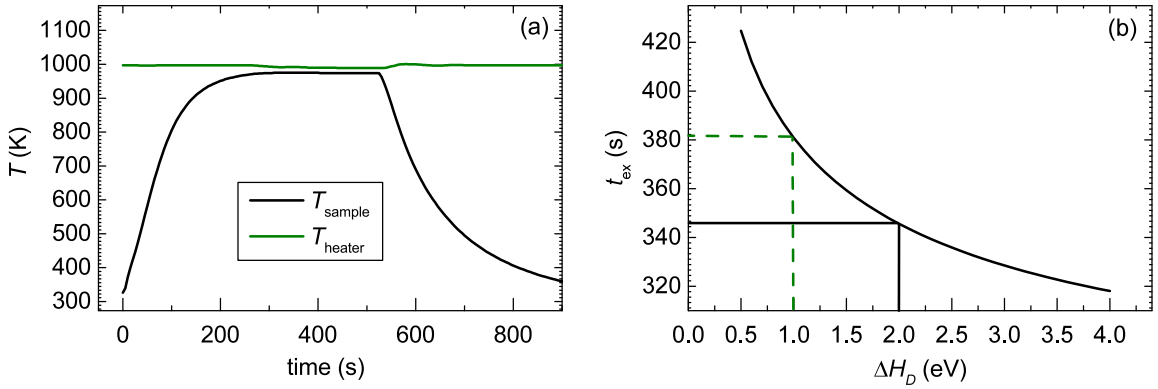

Figure 3.7: (a) Typical profiles of the temperature measured at the sample (black line). The heater temperature of the furnace (green line) is automatically adjusted with help of a second control loop, which is dependent on that controlling the sample temperature (cascade control). (b) t_{ex} versus the enthalpy of diffusion ΔH_D of the investigated process . The smaller ΔH_D, the larger the effect of diffusion that takes places during heating and cooling of the sample to the desired set point. For large errors in ΔH_D, the error in t_{ex} will be large too.

3.4 Secondary Ion Mass Spectrometry

Secondary Ion Mass Spectrometry (SIMS) is a powerful tool to probe a sample's composition with trace level (ppm or in some cases ppb) sensitivity, sub-micrometer lateral resolution and sub-nanometer depth resolution. [44]

The principle of SIMS is based on the fact that during a sputter process a small fraction of charged particles is formed that can be extracted and analyzed with a mass spectrometer. [45] In the following, it will be shown how this principle can be exploited for the analysis of solid state samples. In the second part of this section, some instrumental details regarding depth profiling of oxygen isotopes will be covered.

The SIMS-principle is sketched in Fig. 3.8. Primary ions (PI) – typically Ga^+, Cs^+, O_2^+, Bi^+ – are focused onto a target with a defined energy, typically ranging from 0.25 keV to 30 keV.

Upon impinging on the sample surface these primary ions induce collision cascades by elastically transferring their energy to the target atoms (Fig. 3.8). Collision cascades that reach the surface may cause species – atoms, ions or molecules – to be ejected from the target's first one or two mono layers, typically with an energy distribution peaking around 10 eV. A minute fraction of these sputtered species is charged (a fraction of 10^{-4} to 10^{-6}). These are the secondary ions (SI). By means of an extraction electrode the SI are collected and sorted according to their mass to charge ratio ($\frac{m}{q}$) in a mass spectrometer (see Fig. 3.9). This principle allows for detection of every isotope in the periodic table. The detected intensity of secondary ions i_X^{SI} of a specific isotope X depends on a number of variables:

$$i_X^{\mathrm{SI}} = i^{\mathrm{PI}} Y \alpha_X^{+/-} \eta_X \Theta_X c_X \tag{3.8}$$

with i^{PI} being the primary ion (PI) intensity; Y the sputter yield; $\alpha_X^{+/-}$ the probability of the formation of positive or negative ions respectively; η_X the transfer efficiency of ions through the SIMS detector system; Θ_X the abundance of the detected isotope X and c_X the concentration of the respective element.

Except for $\alpha_X^{+/-}$ and η_X all quantities in Eq. (3.8), the "SIMS equation", are tabulated (Θ_X)[42] or can be measured (Y and i^{PI}). But it is these two quantities that vary by orders of magnitude depending on the secondary ion monitored, the matrix investigated and the measurement conditions. Hence SIMS intensities neither represent the sample's stoichiometry nor do they necessarily reflect changes in concentration of an isotope when investigating different materials in heterostructures.

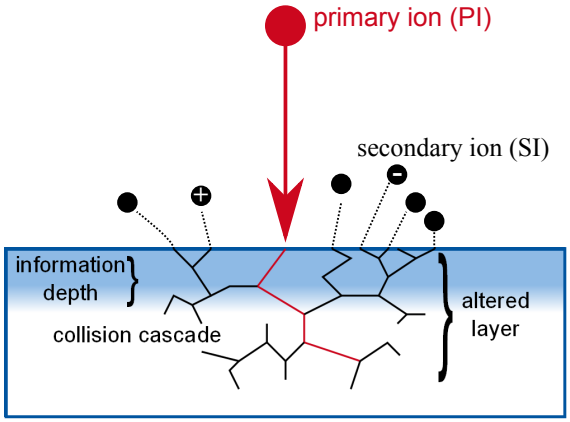

Figure 3.8: Visualization of the SIMS principle. A primary ion hits the sample surface and induces collision cascades. Some of the cascades return to the surface and secondary ions (SI) are emitted. The blue shaded area corresponds to the depth secondary ions are emitted from, the "information depth". The entire area where collision cascades are induced by the primary ions is called the "altered layer".

Considering ratios $i_{X1}^{\mathrm{SI}}/i_{X2}^{\mathrm{SI}}$ of different isotopes ($X1$ and $X2$) of the same element — as for example for ^{16}O and ^{18}O — provides an elegant way to make results comparable between different systems. In the here presented work we are not interested in the absolute concentrations of elements present, only their distribution in the heterostructure samples is of interest. For this reason, considering only intensity ratios is sufficient to correctly analysise isotope diffusion profiles.[5]

The raw data of secondary ion intensities are measured with a single event detector. The

[5] Absolute quantification of SIMS data is also possible by measuring i_X^{SI} on standards with similar properties as the material under investigation, but with known c_X and Θ_X. Ion-implantation techniques are often employed to produce these standards.[46–48]

uncertainty i_X^{SI} is measured with is thus determined by counting statistics and follows a square-root dependence $\Delta i_X^{\mathrm{SI}} \propto (i_X^{\mathrm{SI}})^{-1}$. To keep the error in i_X^{SI} its ratios as small as possible, a high value of i_X^{SI} is desirable. Since i_X^{SI} is determined by the parameters in Eq. (3.8), optimization of i_X^{SI} is only possible by tuning these parameters. Of these parameters only the primary ion current i^{PI} is truly material independent. All other parameters depend on the combination of the material investigated and the secondary ion monitored. $\alpha_{\mathrm{X}}^{+/-}$ is an exception in the sense that it can be influenced by the primary ion used: Employing the electronegative O_2^+ as a primary ion increases α_X^+, that means species that tend to form cations are best monitored sputtering with O_2^+. On the other hand Cs^+ increases α_X^-, hence the investigation of electronegative elements should be conducted sputtering with Cs^+.

In the bulk part of this work oxygen isotopes are analysised. Here $i_{16/18_{\mathrm{O}}}^{\mathrm{SI}}$ is generally very high when sputtering with Cs^+. Thus uncertainties in intensities are low and the minor isotope ^{18}O can be reliably detected despite its low natural abundance. Quite contrary, extracting the correct isotopic fraction can be problematic, because intensities are too high $i_{16/18_{\mathrm{O}}}^{\mathrm{SI}}$. In such cases the single event detector saturates and intensities cannot be measured reliably.[49–52] To avoid this problem of detector saturation and to determine the secondary ion intensity of both oxygen isotopes with high accuracy, the so called "burst mode" along with the corresponding data analysis routine, as detailed in Ref. [49], is applied.

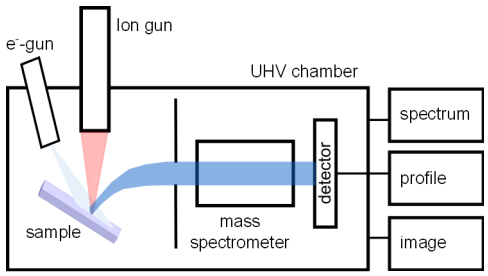

Figure 3.9: Realisation of the SIMS principle in a ToF-SIMS instrument. All components are placed in a vacuum system with a base pressure of $p_{\mathrm{base}} \leq 10^{-10}$ mbar. Ion guns are used to generate ions for sputtering as well as the secondary ions monitored. Electric charges can be compensated with an electron flood gun.

When analysing diffusion profiles, not only the determination of the correct isotope ratios is a concern. A high depth resolution is also desirable. For this purpose low energy ions for sample erosion are required.[53,54] On the other hand high energy ions are beneficial to achieve good lateral resolution and high sputter yields.[55,56] For depth profiling both properties, a high depth resolution and a high sputter yield, are necessary. These two goals cannot be reached by using only one ion beam.

To solve the dichotomy between having to choose high or low energy primary ions, the dual beam technique[57] is applied: A low energy, high current ion beam of Cs^+ or O_2^+ is used to efficiently sputter the sample material. A high-energy, but low current Ga^+ ion beam is employed to create the secondary ions used for analysis. This decoupling of sputter processes for sample erosion and analysis provides the possibility to independently optimize both processes. As the ion beam current of the Ga^+ beam is very low, the sputter ion beam still determines $\alpha_X^{-/+}$.

To correctly interpret depth profiles, one has to keep in mind that profiles always are broad-

ened by sputter-induced effects (ion-beam mixing, topography development) and a convolution of these effects with the "true profile" is observed.[58] Consequently due care has to be taken whether these effects can be neglected or not.
During a SIMS analysis the information of the SI intensity (i_X^{SI}) is recorded as a function of sputter time. In order to obtain a true depth profile, the sputter time needs to be converted into the corresponding sputter depth. To do this, sputter rates have to be determined for each material present in the investigated sample. These rates are determined by measuring the depth of a sputter crater after a defined sputter time by means of stylus profilometry. In cases the material is present in form of a thin films with a thickness below $d \leq 60\,\mathrm{nm}$, the thickness is determined by means of XRR.
In writing this section the following references have been consulted and shall be recommended for a comprehensive introduction into the technological aspects of SIMS: Refs. [44,46,47,59–61]
In this work a dual beam TOFSIMS IV machine (IONTOF GmbH, Münster, Germany) was used. Typically a beam of 25 keV Ga^+ ions was rastered over $50\,\mu\mathrm{m} \times 50\,\mu\mathrm{m}$ to generate secondary ions for ToF analysis (either in burst mode to monitor oxygen isotopes or in bunched mode to monitor metal species.[49]) Low-energy ion beams of Cs^+ or O_2^+ were used to sputter-etch the sample surface (2 keV Cs^+ for the oxygen isotope profiles or 1 keV O_2^+ for the metal species profiles) over an area of $200\,\mu\mathrm{m} \times 200\,\mu\mathrm{m}$. For charge compensation a beam of low-energy ($< 20\,\mathrm{eV}$) electrons was used.

3.5 Additional techniques

Techniques described above were used to produce, characterise and obtain the results the main claims of this work are founded on. Other techniques were occasionally applied to support arguments or to broaden the understanding of observed phenomena.

Interference Microscopy and Stylus Profilometry:
These two methods are applied to characterise sample surfaces. Stylus profilometry is applied to determine the depth of sputter craters after a SIMS measurement and in that manner convert sputter times into sputter depth. Interference microscopy (Wyco NT1100, Veeco Instruments Inc., Plainview, NY, USA) is applied as a general tool to obtain information about a sample's surface quality. Additional information about interference microscopy can be found in Refs. [62–64]. For stylus profilometry Refs.[64,65] can be consulted.

X-ray Photoelectron Spectroscopy (XPS) and X-ray Photoelectron Emission Microscopy (XPEEM)
These two methods rely on the photoelectric effect and enable chemical analysis of the solid state with an information depth of approx. 5-10 nm. The characteristic binding energy of

electrons is used to determine the electronic structure of a sample. Furthermore does the intensity of the detected electrons allow for determination of the sample composition. With XPEEM this information can be obtained laterally resolved, whereas XPS integrates over the entire sample surface. For comprehensive information Refs. [66–68] are recommended for cosultation. XPEEM measurements in this work were conducted by Christoph Bäumer (PGI-7, Forschungszentrum Jülich, Jülich, Germany) and made on a NanoESCA machine (Omicron Nanotechnology GmbH, Taunusstein, Germany) operated in aberration-corrected energy filtered imaging ESCA mode with Al K_α X-ray illumination (pass energy 100 eV). The same holds for XPS measurements conducted on a PHI 5000 Versa Probe (Physical Electronics Inc., Chanhassen, USA) with Al K_α X-ray illumination, a pass energy of 29.35 eV and a take-off angle of 45°. Electron neutralisation was employed. The data were processed using CasaXPS[69].

Conductivity Measurements

The electrical conductivity data used in this work was provided by Dr. Felix Gunkel (PGI-7, Forschungszentrum Jülich, Jülich, Germany). Measurements were conducted on a physical property measurement system (PPMS) (Quantum Design INC, San Diego, USA) employing samples in four-terminal Hall-bar geometry.

Bibliography

[1] G. Binnig, C. F. Quate and C. Gerber, *Phys. Rev. Lett.*, 1986, **56**, 930–933.
[2] F. J. Giessibl, *Rev. Mod. Phys.*, 2003, **75**, 949.
[3] Q. Zhong, D. Inniss, K. Kjoller and V. Elings, *Surf. Sci. Lett.*, 1993, **290**, L688–L692.
[4] D. Nečas and P. Klapetek, *Central European Journal of Physics*, 2012, **10**, 181–188.
[5] M. Wojdyr, *J. Appl. Crystallogr.*, 2010, **43**, 1126–1128.
[6] M. Björck and G. Andersson, *J. Appl. Crystallogr.*, 2007, **40**, 1174–1178.
[7] L. Spieß, G. Teichert, R. Schwarzer, H. Behnken and C. Genzel, *Moderne röntgenbeugung*, Springer-Verlag, 2009.
[8] M. Birkholz, *Thin film analysis by X-ray scattering*, John Wiley & Sons, 2006.
[9] B. E. Warren, *X-ray Diffraction*, Courier Corporation, 1969.
[10] D. P. Norton, *Mater. Sci. Eng., R*, 2004, **43**, 139 – 247.
[11] D. Smith, *Thin-Film Deposition: Principles and Practice*, McGraw-Hill Education, 1995.
[12] D. B. Chrisey and G. K. Hubler, *Pulsed laser deposition of thin films*, Wiley New York, 1994.
[13] R. Eason, *Pulsed laser deposition of thin films: applications-led growth of functional materials*, John Wiley & Sons, 2007.
[14] D. Dijkkamp, T. Venkatesan, X. D. Wu, S. A. Shaheen, N. Jisrawi, Y. H. Min-Lee, W. L. McLean and M. Croft, *Appl. Phys. Lett.*, 1987, **51**, 619–621.
[15] D. G. Schlom, L.-Q. Chen, X. Pan, A. Schmehl and M. A. Zurbuchen, *J. Am. Ceram. Soc.*, 2008, **91**, 2429–2454.
[16] G. Koster, B. L. Kropman, G. J. H. M. Rijnders, D. H. A. Blank and H. Rogalla, *Appl. Phys. Lett.*, 1998, **73**, 2920–2922.
[17] T. Ohnishi, K. Shibuya, M. Lippmaa, D. Kobayashi, H. Kumigashira, M. Oshima and H. Koinuma, *Appl. Phys. Lett.*, 2004, **85**, 272–274.
[18] F. Gunkel, *The role of defects at functional interfaces between polar and non-polar perovskite oxides*, Forschungszentrum Jülich, 2013.
[19] A. Herpers, *Electrical characterization of manganite and titanate heterostructures*, Forschungszentrum Jülich, 2014, vol. 32.
[20] W. Hong, H. N. Lee, M. Yoon, H. M. Christen, D. H. Lowndes, Z. Suo and Z. Zhang, *Phys. Rev. Lett.*, 2005, **95**, 095501.
[21] A. Vailionis, H. Boschker, W. Siemons, E. P. Houwman, D. H. A. Blank, G. Rijnders and G. Koster, *Phys. Rev. B*, 2011, **83**, 064101.
[22] R. A. Rao, Q. Gan and C. B. Eom, *Appl. Phys. Lett.*, 1997, **71**, 1171–1173.
[23] A. Vailionis, W. Siemons and G. Koster, *Appl. Phys. Lett.*, 2008, **93**, 051909.
[24] D. Schlom, D. Anselmetti, J. Bednorz, R. Broom, A. Catana, T. Frey, C. Gerber, H.-J. Güntherodt, H. Lang and J. Mannhart, *Z. Phys. B: Condens. Matter*, 1992, **86**, 163–175.
[25] C. Eom, R. Cava, R. Fleming, J. M. Phillips, J. Marshall, J. Hsu, J. Krajewski and W. Peck, *Science*, 1992, **258**, 1766–1769.
[26] K. J. Choi, S. H. Baek, H. W. Jang, L. J. Belenky, M. Lyubchenko and C.-B. Eom, *Adv. Mater.*, 2010, **22**, 759–762.
[27] N. Zakharov, K. Satyalakshmi, G. Koren and D. Hesse, *J. Mater. Res.*, 1999, **14**, 4385–4394.
[28] W. Siemons, G. Koster, A. Vailionis, H. Yamamoto, D. H. A. Blank and M. R. Beasley, *Phys. Rev. B*, 2007, **76**, 075126.
[29] J. Kilner, B. Steele and L. Ilkov, *Solid State Ionics*, 1984, **12**, 89 – 97.
[30] D. J. Reed and B. J. Wuensch, *J. Am. Ceram. Soc.*, 1980, **63**, 88–92.
[31] R. A. De Souza and J. F. Kilner, J. A .and Walker, *Mater. Lett.*, 2000, **43**, 43–52.
[32] R. A. De Souza and R. J. Chater, *Solid State Ionics*, 2005, **176**, 1915 – 1920.
[33] D. R. Killoran, *J. Electrochem. Soc.*, 1962, **109**, 170–171.
[34] D. R. Killoran, *J. Electrochem. Soc.*, 1962, **109**, 1215–1216.
[35] W. D. Kingery, J. Pappis, M. E. Doty and D. C. Hill, *J. Am. Ceram. Soc.*, 1959, **42**, 393–398.
[36] A. Paladino, L. Rubin and J. Waugh, *J. Phys. Chem. Solids*, 1965, **26**, 391 – 397.
[37] M. C. Kim, S. J. Park, H. Haneda, J. Tanaka, T. Mitsuhasi and S. Shirasaki, *J. Mater. Sci. Lett.*, 1990, **9**, 102–104.
[38] J. A. Kilner, S. J. Skinner and H. H. Brongersma, *J. Solid State Electrochem.*, 2011, **15**, 861–876.
[39] P. Fielitz and G. Borchardt, *Solid State Ionics*, 2001, **144**, 71–80.
[40] J.-M. Bassat, M. Petitjean, J. Fouletier, C. Lalanne, G. Caboche, F. Mauvy and J.-C. Grenier, *Appl. Catal., A*, 2005, **289**, 84 – 89.
[41] A. O. Nier, *Phys. Rev.*, 1950, **77**, 789.
[42] J. Böhlke, J. De Laeter, P. De Bievre, H. Hidaka, H. Peiser, K. Rosman and P. Taylor, *J. Phys. Chem. Ref. Data*, 2005, **34**, 57–67.

[43] M. Kessel, R. De Souza, H.-I. Yoo and M. Martin, *Appl. Phys. Lett.*, 2010, **97**, 021910–021910.
[44] D. McPhail, *J. Mater. Sci.*, 2006, **41**, 873–903.
[45] R. F. K. Herzog and F. P. Viehböck, *Phys. Rev.*, 1949, **76**, 855–856.
[46] R. De Souza and M. Martin, *Bunsen-Magazin*, 2006, **8**, 109–120.
[47] R. G. Wilson, F. A. Stevie and C. W. Magee, *Secondary ion mass spectrometry: a practical handbook for depth profiling and bulk impurity analysis*, Wiley-Interscience, 1989.
[48] C. W. Magee, D. Jacobson and H.-J. Gossmann, *J. Vac. Sci. Technol., B*, 2000, **18**, 489–492.
[49] R. A. De Souza, J. Zehnpfenning, M. Martin and J. Maier, *Solid State Ionics*, 2005, **176**, 1465–1471.
[50] T. Stephan, J. Zehnpfenning and A. Benninghoven, *J. Vac. Sci. Technol., A*, 1994, **12**, 405–410.
[51] H. Téllez, J. Druce, J.-E. Hong, T. Ishihara and J. A. Kilner, *Anal. Chem.*, 2015, **87**, 2907–2915.
[52] G. Holzlechner, M. Kubicek, H. Hutter and J. Fleig, *J. Anal. At. Spectrom.*, 2013, **28**, 1080–1089.
[53] P. C. Zalm, *Rep. Prog. Phys.*, 1995, **58**, 1321.
[54] J. Clegg, N. Smith, M. Dowsett, M. Theunissen and W. De Boer, *J. Vac. Sci. Technol., A*, 1996, **14**, 2645–2650.
[55] N. Laegreid and G. Wehner, *J. Appl. Phys.*, 1961, **32**, 365–369.
[56] J. Bohdansky, *Nuclear Instruments and Methods in Physics Research Section B: Beam Interactions with Materials and Atoms*, 1984, **2**, 587–591.
[57] K. Iltgen, C. Bendel, A. Benninghoven and E. Niehuis, *The 43rd national symposium of the American Vacuum Society*, 1997, **15**, 460–464.
[58] S. Hofmann, *Rep. Prog. Phys.*, 1998, **61**, 827.
[59] *Secondary Ion Mass Spectroscopy: Principles and Applications*, ed. J. C. Vickerman, N. Reed and A. Brown, Oxford University Press, 1989, p. 341.
[60] R. A. De Souza and M. Martin, *MRS Bulletin*, 2009, **34**, 907–914.
[61] A. Benninghoven, F. Rüdenauer and H. Werner, *Secondary Ion Mass Spectrometry: Basic Concepts, Instrumental Aspects, Applications, and Trends*, J. Wiley, 1987.
[62] H. Beyer, *Theorie und Praxis der Interferenzmikroskopie*, Akademische Verlagsgesellschaft Geest&Portig K.-G., 1974.
[63] M. Spencer, *Fundamentals of light microscopy*, CUP Archive, 1982.
[64] K. J. Stout and L. Blunt, *Three dimensional surface topography*, Elsevier, 2000.
[65] E. C. Teague, F. E. Scire, S. M. Baker and S. W. Jensen, *Three-dimensional stylus profilometry*, Elsevier, 1982, vol. 83, pp. 1–12.
[66] J. J. Weimer, in *Characterization of Materials*, John Wiley & Sons, Inc., 2002, ch. X-Ray Photoelectron Spectroscopy, pp. 1493–1535.
[67] B. P. Tonner, D. Dunham, T. Droubay and M. Pauli, *J. Electron Spectrosc. Relat. Phenom.*, 1997, **84**, 211–229.
[68] M. Mundschau, *Synchrotron Radiation News*, 1991, **4**, 29–34.
[69] N. Fairley, *CasaXPS, version 2.3.16*, Casa Software, Ltd., Teighnmouth, Devon, U.K. technical report, 2011.

Chapter 4

Oxygen and Titanium Diffusion in $SrRuO_3$ Thin Films

This chapter will deal with oxygen and titanium diffusion in $SrRuO_3$ thin films. First, we will address the influence of sample exposure to elevated temperatures. Here it will be shown in what way the experimental procedure used to investigate diffusion affects the sample properties and thus the processes investigated. Second, the diffusion profiles obtained for anion and for cation diffusion will be presented. Both profiles suggest a surprisingly complex defect behaviour. This defect behaviour will be discussed. The main reason for its complexity can be attributed to the non-equilibrium nature of PLD films. The further focus of the discussion will be on a classification of the two diffusion processes and their comparison with diffusion processes in other perovskite oxides.

4.1 Results

All results presented in the following were acquired with samples produced according to the procedure presented in Sec. 3.2.3. Sample properties all match the benchmarks defined there.[1]

4.1.1 Initial annealing experiments

Thin films of $SrRuO_3$ produced by PLD have been reported to undergo morphological and chemical changes upon annealing at elevated temperatures.[1–4] For this reason we first subjected our as-deposited films to pre-anneals at $T = 973\,\mathrm{K}$ and $pO_2 = 500\,\mathrm{mbar}$ for various times. As shown in Fig. (4.1), the surface morphology undergoes significant changes: islands and pits appear, and the rms surface roughness increases, too, to $\mathrm{rms} = 1.75\,\mathrm{nm}$ after 1 day, $\mathrm{rms} = 2.63\,\mathrm{nm}$ after 3 days and $\mathrm{rms} = 5.00\,\mathrm{nm}$ after 5 days. In the same fashion the size of the precipitates observed on the sample surface increases (Fig. 4.1 (d)-(f)). XRD scans of the three samples indicated no significant change in the out-of-plane lattice parameter. Only for samples annealed at the higher temperature of $T = 1073\,\mathrm{K}$ for much longer times, $t_{\mathrm{pre}} > 10$ days, a significant decrease in the out-of-plane lattice constant of $\Delta c \approx 0.2\,\mathrm{pm}$ was observed

[1] The here presented and discussed results have already been published in: H. Schraknepper, C. Bäumer, R. Dittmann and R.A. De Souza *Physical Chemistry Chemical Physics* **17** (2015) 1060-1069

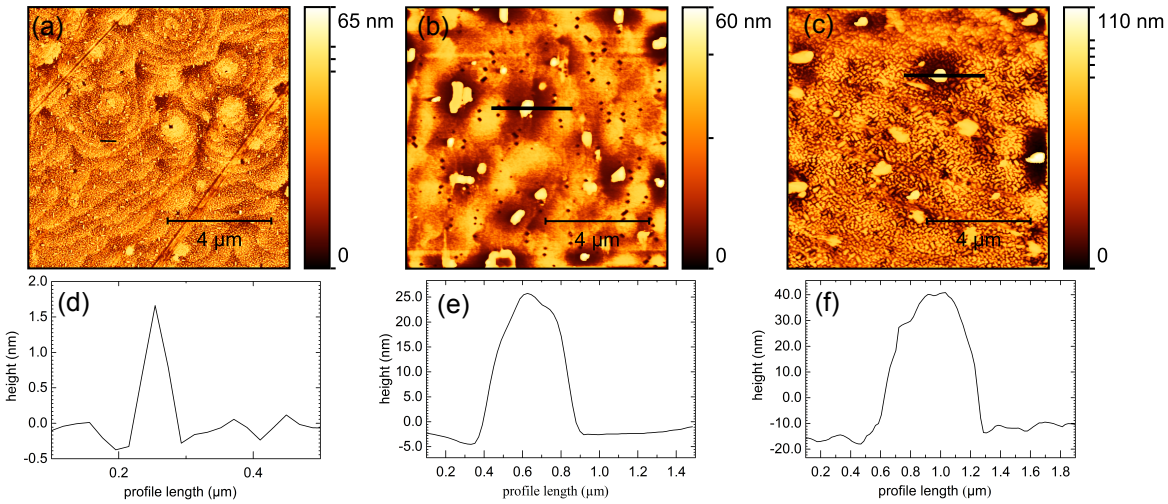

Figure 4.1: Atomic Force Micrographs of $SrRuO_3$ thin film samples after pre-annealing at $T = 973\,\mathrm{K}$ for 1 day (a), 3 days (b), and 5 days (c). The formation of islands and pits was observed. The images refer to an area of $10\,\mu\mathrm{m} \times 10\,\mu\mathrm{m}$. In (d), (e) and (f) line profiles across the observed precipitates are shown. Here a significant increase in the precipitate'size is observed.

(cf. Fig. 4.2). It should be noted that changes in the out-of-plane lattice constant of similar magnitude were detected upon delibarate variation of the cation stoichiometry in $SrTiO_3$ thin-films.[5]

Similar phenomena of island formation have been observed for $SrRuO_3$[1] as well as for other perovskite oxides.[6,7] In many cases the newly formed precipitates are thought to be SrO and the phenomenon is often referred to as "strontium surface segregation".[8,9] In few cases, however, the nature of the precipitates has been directly investigated. Here an XPEEM analysis of differently treated $SrRuO_3$ thin film is presented. This allows for a clarification of the chemical composition of the observed precipitates. In particular it makes the investigation of precipitates in the early stage of their growth possible. Here a SIMS-analysis cannot provide sufficient contrast and lateral resolution. In Fig. (4.5) an XPEEM image, which was taken at a binding energy of $E_\mathrm{B} = 132\,\mathrm{eV}$ and can be assigned to the Sr $3d^{\mathrm{SrRuO_3}}_{(5/2)}$ core level, shows dark features, which are similar in shape and length scale to the features observed in the AFM micrographs (Fig. 4.1). Such features were absent from XPEEM images of

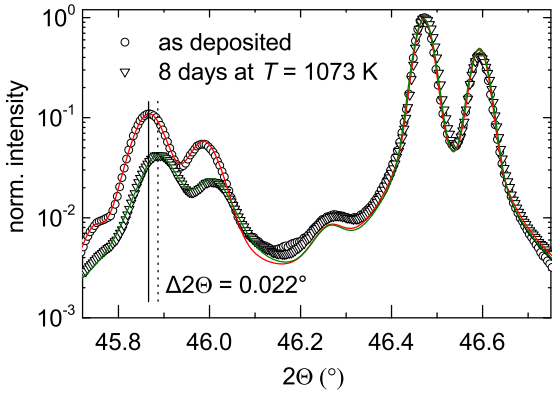

Figure 4.2: $2\Theta - \omega$ scans of the $SrTiO_3$ (200) and the $SrRuO_3$ $(002)_\mathrm{pc}$ reflexes of one thin-film sample in the as-deposited state as well as after anneanling at $T = 1073\,\mathrm{K}$ and $pO_2 = 500\,\mathrm{mbar}$ for $t_\mathrm{pre} > 10$ days. A shift of the $SrRuO_3$ $(002)_\mathrm{pc}$ reflex to higher 2Θ is observed indicating a reduction of the $SrRuO_3$ out-of-plane lattice constant of $\Delta c \approx 0.2\,\mathrm{pm}$. (red and green lines are the respective fits.)

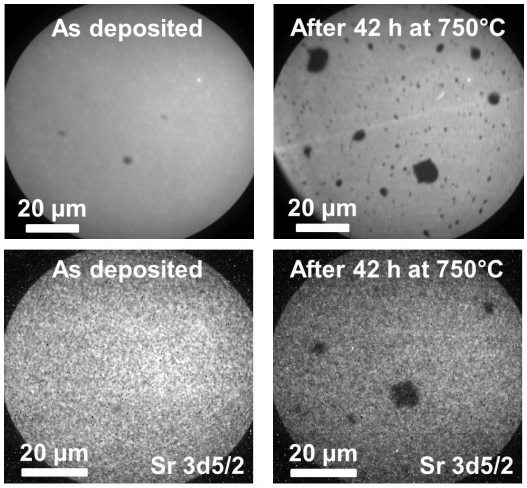

Figure 4.3: PEEM micrographs of differently annealed samples. In the upper row the work-function contrast is depicted. Whereas for the untreated sample no lateral inhomogenities can be observed, for the annealed one μm-sized features can be distinguished. The same holds for the Sr $3d^{SrRuO_3}_{(5/2)}$ contrast shown for both samples in the lower row.[2]

untreated films. Comparing the Sr $3d$ photoemission spectrum for these regions (Fig. 4.5(b)) with that for the unchanged surroundings Fig. 4.5 (a), one finds several distinct differences. First, the Sr $3d^{SrRuO_3}_{(5/2)}$ peak intensity is significantly reduced for the new features, which accounts for the contrast in the XPEEM image. Second, and more importantly, a new peak arises at a binding energy of $E_B = 135.6\,\text{eV}$, and the peak at $E_B = 133.8\,\text{eV}$ is strongly enhanced.

Comparison of these spectra with reference XPS spectra of $SrRuO_3$ and SrO thin films (Fig. 4.5(c)) allows us to assign unambiguously the new microstructural features to SrO as a second phase: the photoemission spectrum extracted for the dark features can be described well by a superposition of $SrRuO_3$ and SrO doublets, while the spectrum extracted for the unmodified surroundings can be described by the $SrRuO_3$ doublet (with an additional small contribution from a surface component regularly found in $SrRuO_3$ spectra [4]).

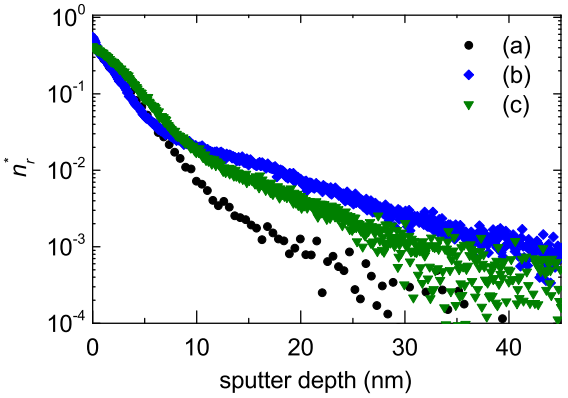

Figure 4.4: Oxygen isotope diffusion profiles obtained for the samples shown in Fig. 4.1 after the same exchange time, $t_{ex} = 7 \times 10^3\,\text{s}$, but different pre-anneal times, t_{pre}: 1 day (a), 3 days (b), and 5 days (c).

The conventional expectation towards the results of isotope exchange experiments is that, regardless of the pre-anneal time t_{pre}, all aquired diffusion profiles should be identical, if the same exchange time t_{ex} is used. Oxygen

[2] All PEEM and XPS measurements presented in this section were conducted by Christoph Bäumer (PGI-7, Forschungszentrum Jülich, Jülich, Germany)

isotope profiles obtained for three samples that were pre-annealed at $T = 973\,\mathrm{K}$ for different times, surprisingly, were not identical (see Fig. 4.4), even though the three samples were exposed to the enriched-isotope atmosphere for the same period of time. Furthermore, two diffusion processes appear to be operative (termed here $\mathrm{An_{sl}}$ for the slower anion process and $\mathrm{An_{fa}}$ for the faster anion process), with the faster process ($\mathrm{An_{fa}}$) becoming more dominant with increasing *pre-anneal* time.

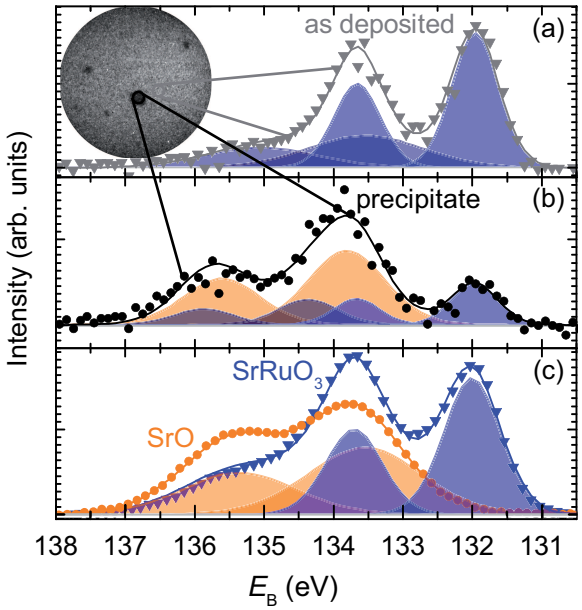

Figure 4.5: Sr 3*d* photoemission spectra obtained for unchanged regions (a) and new features (b) of a $SrRuO_3$ thin film pre-annealed at $T = 1073\,\mathrm{K}$ for $t_{\mathrm{pre}} = 42\,\mathrm{h}$. Inset shows an XPEEM image (field of view of 80 μm) recorded at a binding energy of $E_B = 132\,\mathrm{eV}$. Reference spectra (energy calibrated) obtained separately for as-deposited $SrRuO_3$ and SrO films (c).

These processes will receive detailed attention in the next section (Sec. 4.2). Here it suffices to summarize two major consequences: First, the occurrence of a second feature in the diffusion profile at sputter-depths of 10 nm-15 nm indicates that the characterized phenomenon is not limited to the surface, but also significantly alters the bulk properties of the $SrRuO_3$ thin films. Second, if accurate diffusion coefficients are to be extracted for both processes, due care must be exercised in selecting both pre-anneal and exchange times. This is of particular importance as the conventional selection of t_{pre} might already result in substantial surface roughening. Low surface roughness, however, is critical for reliable diffusion experiments (as well as for further integration of $SrRuO_3$ films into multilayer devices). For this reason much shorter pre-anneal times will be chosen. This is legitimate, because the major reason for the choice of long pre-anneal times is the establishment of stable surface conditions[3] and the removal of polishing damage.[10] In the present case of epitaxial thin films with atomically flat surfaces, the main reason for a prolonged pre-anneal becomes obsolete.

[3]Here the two other reasons for the pre-anneal mentioned in Sec. 3.3 are negligible: The establishment of a constant chemical potential will be much faster than the tracer diffusion process and thus not decicive. Furthermore it was checked that no tracer profile was present after only the pre-anneal.

4.1.2 Oxygen diffusion

In this section the results of isotope exchange experiments and the subsequent SIMS-analysis are presented. As elaborated in Sec. (3.3), due care was taken that the boundary conditions imposed by the isotope exchange experiment correspond to isotope incorporation taking place from a large volume of gas, such that n^*_{gas} is constant for the duration of the anneal.[10] A second requirement for the way of straight forward data analysis, presented in Sec. 2.5, to be valid, is that the isotope profile is shorter than the film thickness. In this case the film can be treated as a semi-infinite medium.
Only then the solution of the diffusion equation for a uniform medium with these boundary conditions and with first-order surface-reaction kinetics is a modified complementary error function:[11]

$$\begin{aligned} n^*_r &= \frac{n^*(x,t_{\mathrm{ex}}) - n^*_{\mathrm{bg}}}{n^*_{\mathrm{gas}} - n^*_{\mathrm{bg}}} \\ &= \mathrm{erfc}(x') - \exp(h'x' + h'^2) \cdot \mathrm{erfc}(x' + h') \end{aligned} \tag{4.1}$$

where the solution has been written in terms of the dimensionless variables $x' = x/\sqrt{4D^*_{\mathrm{O}}t_{\mathrm{ex}}}$ and $h' = (k^*_{\mathrm{O}}/D^*_{\mathrm{O}})\sqrt{D^*_{\mathrm{O}}t_{\mathrm{ex}}}$, with D^*_{O} being the tracer diffusion coefficient of oxygen, k^*_{O} the oxygen surface exchange coefficient and x the spatial coordinate.

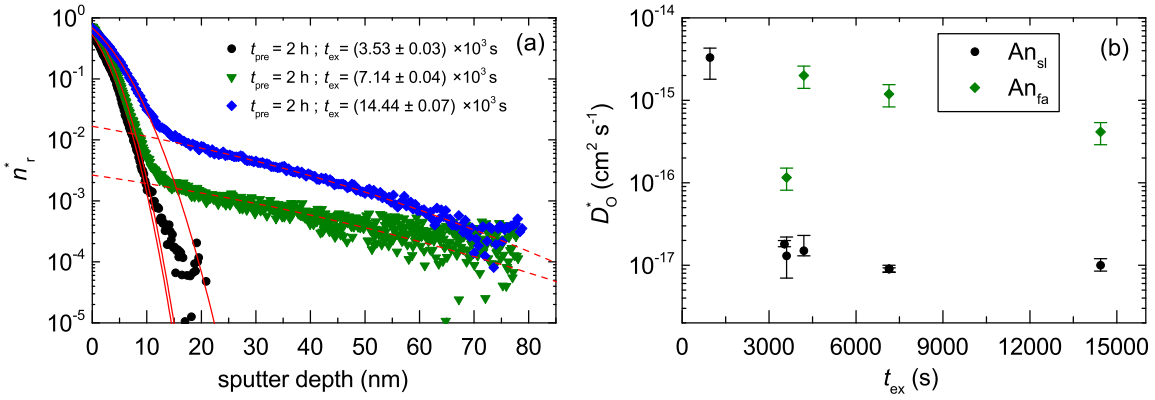

Figure 4.6: (a) Oxygen isotope diffusion profiles measured for different exchange times and the corresponding fitted curves to Eq. (4.1): $\mathrm{An_{sl}}$ (solid line), $\mathrm{An_{fa}}$ (dashed line). (b) Oxygen tracer diffusion coefficients obtained as a function of exchange time t_{ex} for both $\mathrm{An_{sl}}$ and $\mathrm{An_{fa}}$. Samples were annealed at $T = 1023\,\mathrm{K}$ and $p\mathrm{O_2} = 500\,\mathrm{mbar}$.

Whereas a single feature is expected for a uniform medium with constant D^*_{O} (Eq. (4.1)), the experimental profiles obtained for $\mathrm{SrRuO_3}$ thin films for various exchange times (but with constant pre-anneal time) show two features (see Fig. 4.6 (a)). The traditional explanation for a diffusion profile consisting of two features is the occurrence of bulk diffusion (the slow process) and accelerated diffusion along extended defects such as dislocations or grain boundaries combined with bulk diffusion (the fast process). This is referred to as "Harrison type-B" diffusion kinetics (cf. Sec. (2.5.2)). As it will be shown in Sec. 4.1.4, however, $\mathrm{An_{fa}}$

does not correspond to diffusion along extended defects, neither along dislocations nor along grain boundaries. Rather, An_{fa} is best described by a modified complementary error function, Eq. (4.1). The entire profile is therefore described by two modified complementary error functions, each with a tracer diffusion coefficient and a surface exchange coefficient.
When describing the experimentally obtained data with Eq. (4.1), the major concern regards the reliability of the extracted diffusion constants for both processes, $D^*_O(An_{sl})$ and $D^*_O(An_{fa})$. The reason is the extremely shallow nature of the profiles observed. This subject was broached in Sec. 3.4. We know that SIMS profiles are broadened by ion beam mixing and the surface roughness of the sample. These effects can be taken into account by determining a depth resolution function for each specific material system.[12] As this is a very elaborate process, question one has to aks is: When does the SIMS depth resolution function has to be considered and when can it be neglected? One answer this question by plotting the extracted diffusion constants $D^*_O(An_{sl})$ and $D^*_O(An_{fa})$ as a function of exchange time t_{ex} as shown Fig. 4.6 (b). The data for An_{sl}, with the exception of the data point for the shortest exchange time, display a constant value. This means that after the profile lengths exceed a certain limit, profile broadening can be neglected. And although the depth resolution function was not determined, one can deduce from Fig. 4.6 (a) and Fig. 4.6 (b) that isotope diffusion profiles have to be at least 15 nm long in these particular samples to obtain reliable transport data. Furthermore it is confirmed that, even for such short isotope penetration profiles (here, of the order of tens of nanometers), it is possible to reliably determine diffusion coefficients. In this context I want to emphasise that by taking care of the issues described above the determination of reliable diffusion data is an iterative process. Neither $D^*_O(An_{sl}/An_{fa})$ nor the activation enthalpy of the diffusion process are known prior to the experiments. For this reason one has to repeat the experiment in cases the realised profile length did not exceed the required 15 nm. At the same time arbitrarily long exchange times are not feasible, as the realization of too long diffusion profiles would violate the semi-infinite medium conditions demanded for a reliable extraction of $D^*_O(An_{sl}/An_{fa})$.

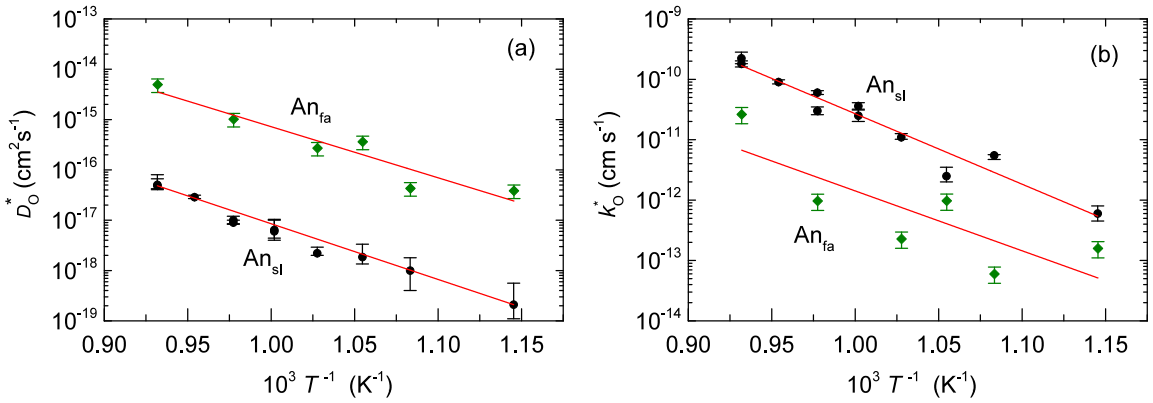

Figure 4.7: Variation as a function of inverse temperature of oxygen tracer diffusion coefficients D^*_O (a) and oxygen surface exchange coefficients k^*_O (b). All data refer to an oxygen partial pressure of $pO_2 = 500$ mbar.

In Fig. 4.6 (b) the data for the two observed processes is shown. The values for An_{fa} show

more scatter than those for An_{sl}. As a consequence we limited further analysis of An_{fa} to those diffusion coefficients obtained for the longest exchange times. It is also noted that no An_{fa} profile was observed for the shortest exchange time. A reason for both observations will be presented in Section 4.2. The the transport data shown in Fig. 4.7 were obtained by repeating the above outlined procedure at different temperatures. It is worth noting that $k^*_O(An_{sl}) > k^*_O(An_{fa})$, although $D^*_O(An_{sl}) < D^*_O(An_{fa})$; in both cases the activation enthalpies are, within experimental error, identical. Analysis yields values for oxygen tracer diffusion of $\Delta H_{D^*_O(An_{sl})} = (2.1 \pm 0.2)\,\text{eV}$ and $\Delta H_{D^*_O(An_{fa})} = (2.0 \pm 0.3)\,\text{eV}$, and for oxygen surface exchange of $\Delta H_{k^*_O(An_{sl})} = (2.3 \pm 0.2)\,\text{eV}$ and $\Delta H k_{D^*_O(An_{fa})} = (2.0 \pm 0.7)\,\text{eV}$.

4.1.3 Titanium diffusion

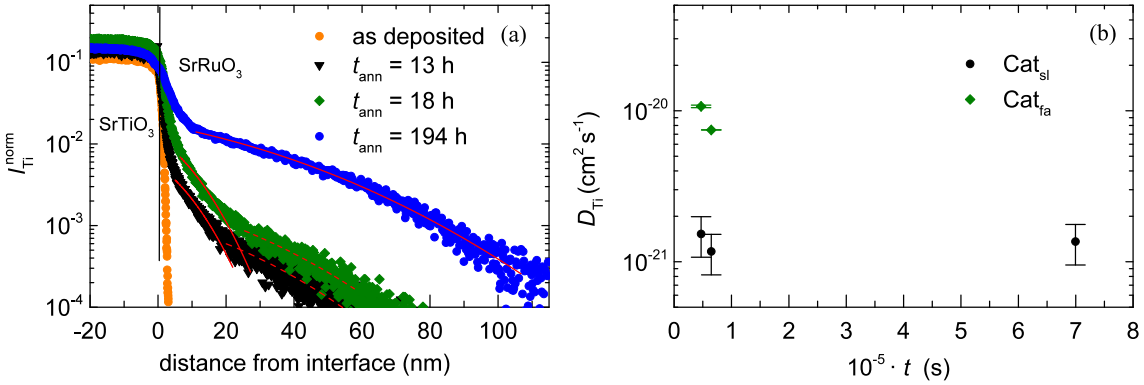

Figure 4.8: (a) Normalized secondary ion intensity, $I^{norm}_{Ti} = I(^{48}Ti)/I(^{88}Sr)$, obtained for thin-film $SrRuO_3$ on single crystal $SrTiO_3$ substrates for various annealing times and the corresponding fitted curves to Eq. (4.2): Cat_{sl} (solid line), Cat_{fa} (dashed line). (b) Titanium diffusion coefficients obtained as a function of annealing time t_{ann} for both Cat_{sl} and Cat_{fa}. Samples were annealed at $T = 1073\,\text{K}$ and $pO_2 = 500\,\text{mbar}$.

By comparing SIMS depth profiles for an as-deposited and for annealed samples (Fig. 4.8 (a)), we found unequivocal evidence of Ti diffusion into the $SrRuO_3$ thin film, but no evidence of Ru diffusion into the $SrTiO_3$ substrate. It is striking that, as in the case of oxygen tracer diffusion, two distinct Ti diffusion processes (a slower cation process, Cat_{sl}, and a faster cation process, Cat_{fa}) are clearly discernible. In this case, however, the faster process, Cat_{fa}, becomes *less* pronounced with increasing anneal time, and for the longest diffusion time examined, it is no longer discernible.

Since the total amount of Ti diffusing into the $SrRuO_3$ thin film is small, the $SrTiO_3$ substrate effectively serves as a constant source of the Ti diffusant. The appropriate solution of the diffusion equation is thus[11]

$$I^{norm}_{Ti} = A\,\text{erfc}\left[\frac{x}{2\sqrt{D_{Ti} \cdot t_{ann}}}\right] \tag{4.2}$$

where I^{norm}_{Ti} is the secondary ion intensity of titanium normalised to the value for strontium; A is a scaling factor; and D_{Ti} is the diffusion coefficient of Ti in thin film $SrRuO_3$.

Each of the two parts of the cation diffusion profile is best described by Eq. (4.2), as shown in Fig. 4.8(a). As in the case of oxygen tracer diffusion, $\mathrm{Cat_{fa}}$ cannot be attributed to fast diffusion of Ti along dislocations, because it disappears with increasing anneal time. The values of $D_{\mathrm{Ti}}(\mathrm{Cat_s})$ and $D_{\mathrm{Ti}}(\mathrm{Cat_f})$ obtained from the fits are plotted as a function of anneal time t_{ann} in Fig. 4.8 (b). As far as it is possible to determine, both diffusion coefficients are independent of annealing time, confirming that diffusion processes were observed, rather than, for example, the effect of interface roughening. Note the annealing times involved in cation diffusion are much longer than for anion diffusion (compare Fig. (4.6) (b) and Fig. 4.8 (b)), and the respective diffusion coefficients are correspondingly smaller, $D_{\mathrm{Ti}} \ll D^*_{\mathrm{O}}$.

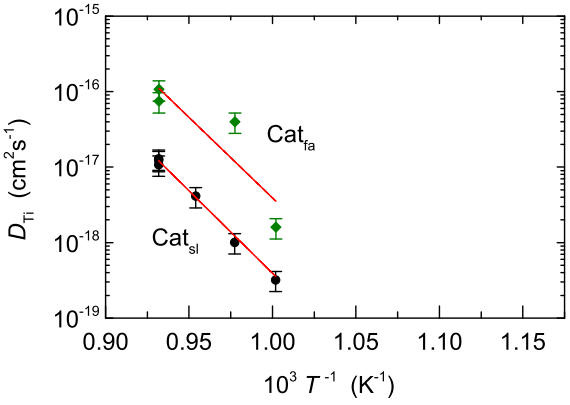

Figure 4.9: Variation of D_{Ti}, the diffusion coefficient of Ti in thin-film $SrRuO_3$, as a function of inverse temperature. All data refer to $p\mathrm{O_2} = 500$ mbar.

In Fig. 4.9, data obtained for $D_{\mathrm{Ti}}(\mathrm{Cat_{sl}})$ and $D_{\mathrm{Ti}}(\mathrm{Cat_{fa}})$ as a function of temperature are shown. The activation enthalpies of diffusion are $\Delta H_{D_{\mathrm{Ti}}(\mathrm{Cat_{sl}})} = (4.3 \pm 0.3)\,\mathrm{eV}$ and $\Delta H_{D_{\mathrm{Ti}}(\mathrm{Cat_{fa}})} = (4.2 \pm 1.5)\,\mathrm{eV}$.

4.1.4 Potential influence of extended defects

Generally, for diffusion profiles that consist of two features, the second feature is taken as evidence of short-circuit diffusion along extended defects, such as dislocations or grain boundaries.[13,14] This is known as "Harrison type-B" diffusion kinetics.[14,15] In such cases, the second feature of the profile – termed the "tail" – displays certain characteristics depending on the type of extended defect: for dislocations,[16] the tail has the form $c \propto \exp(-Z_{\mathrm{dis}} x)$, whereas for grain boundaries,[17] the tail has the form $c \propto \exp(-Z_{\mathrm{gb}} x^{6/5})$. In both cases Z is the characteristic slope in a $\ln(x)$ versus x or in an $\ln(x)$ versus $x^{6/5}$ plot respectively. In addition, the specific values of Z vary with increasing time in different ways, $Z \propto t^m$: for dislocations $m \approx 0$ but for grain boundaries $m = -3/10$.

The diffusion profiles presented in Fig. 4.6 were analysed in terms of short-circuit diffusion along dislocations[16] or along grain boundaries.[18] The values of Z_{dis} and Z_{gb} obtained are shown as a function of time in Fig. 4.10. Neither set of data is consistent with $\mathrm{An_{fa}}$ corresponding to short-circuit diffusion. Furthermore, the variation in $\mathrm{An_{fa}}$ with pre-anneal time argues strongly against assigning this process to short-circuit diffusion (see Fig. 4.4). Hence an alternative explanation for the appearance of two features in a diffusion profile has to be provided.

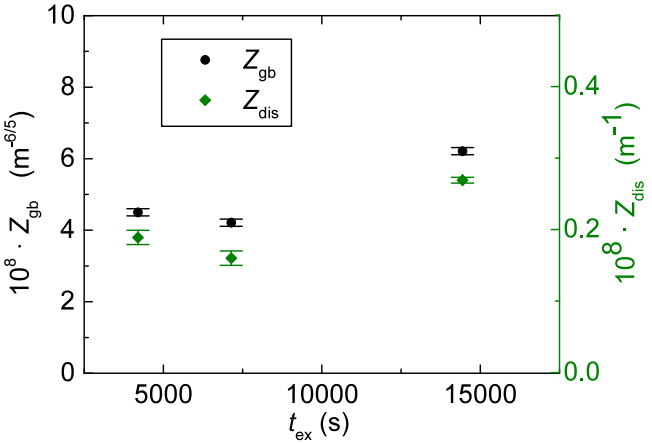

Figure 4.10: Analysing An_{fa} as if it were fast diffusion along grain boundary or dislocations. Data refer to isotope profiles at $T = 1023$ K and $pO_2 = 500$ mbar.

4.2 Discussion

4.2.1 Anion diffusion

In this section all phenomena related to diffusion taking place in the oxygen sublattice will be discussed. In the first part of the discussion the obtained oxygen tracer diffusion data will be compared with diffusion data available for other perovskite oxides. Furthermore some defect-chemical aspects of $SrRuO_3$ will be discussed and in this context an explanation for the appearance of the two-fold diffusion profiles will be given. Subsequently the measured activation enthalpies of diffusion will be compared and discussed. Here two admittedly rather speculative explanations for the unusual values of the activation enthalpies will be given. Lastly the kinetics of the oxygen incorporation reaction, here condensed by $k_{D^*_O}$ will be classified and discussed.

Oxygen diffusion and the origin of two diffusion mechanisms

The oxygen tracer diffusion coefficient in the case of oxygen migration by a vacancy mechanism can be expressed as

$$D^*_O = f^* D_V n_V, \tag{4.3}$$

where f^* is the tracer correlation coefficient (for dilute, non-interacting oxygen vacancies in an ABO_3 perovskite oxide, $f^* = 0.69$);[19] D_V is the vacancy diffusion coefficient; and n_V is the site fraction of oxygen vacancies. In Fig. 4.11(a) we compare D^*_O obtained for thin-film strontium ruthenate with data for selected other perovskite oxide compositions. One sees that oxygen diffusion in $SrRuO_3$ is many orders of magnitude slower than that in nominally undoped $SrTiO_3$ and $BaTiO_3$, and is comparable with that in $LaMnO_3$. Examination of Eq. (4.3) indicates that these low values of D^*_O are due either to lower vacancy diffusivities D_V or to lower site fractions of oxygen vacancies n_V.

Material	$\Delta H_{D^*_O}$ (eV)	$\Delta H_{\mathrm{mig,V}}$ (eV)	$\Delta H_{k^*_O}$ (eV)	$\Delta H_{\mathrm{gen,V}}$ (eV)	Ref.
$SrRuO_3$	(2.1 ± 0.2)	–	(2.5 ± 0.4)	-	this work
$LaMnO_3$	(2.49 ± 0.23)	≈ 0.7	(1.48 ± 0.16)	(3.61 ± 0.06)	20–23
$LaCoO_3$	(3.2 ± 0.22)	(0.78 ± 0.22)	(1.96 ± 0.16)	-	24
$LaFeO_3$	(2.21 ± 0.16)	(0.77 ± 0.25)	-	-	19
$BaTiO_3$	(0.68 ± 0.08)	(0.70 ± 0.04)	(2.15 ± 0.13)	(2.82 ± 0.39)	25,26
$SrTiO_3$	(0.58 ± 0.08)	(0.62 ± 0.08)	(2.95 ± 0.25)	(3.75 ± 0.13)	27,28
$LaAlO_3$	(1.00 ± 0.03)	(1.02 ± 0.03)	(2.42 ± 0.24)	-	29

Table 4.1: Comparison of activation enthalpies of oxygen tracer diffusion, oxygen vacancy diffusion and oxygen surface exchange in selected ABO_3 perovskite oxides.

Comparing literature data[19,20,24,25,27,29] for D_V in ABO_3 perovskite oxides [Fig. 4.11(b)], one finds (as previously identified[19,30,31]) that isothermal values of D_V vary by less than one order of magnitude between different ABO_3 perovskite oxides. This strongly suggests that the low values of D^*_O in $SrRuO_3$ arise from the low site fraction of oxygen vacancies. We cannot discount the possibility, however, of D_V in the $SrRuO_3$ thin-films being outside the (small) range of the literature values for single crystals and polycrystalline ceramics shown in Fig. 4.11(b). Being epitaxial and under a small compressive strain, the thin films may exhibit different vacancy diffusivities compared with unstrained bulk samples, as strain is known to affect the migration of vacancies in perovskite oxides.[32,33] Since the degree of strain is small, though, with $\Delta a/a = 0.64\,\%$ (based on the lattice mismatch of pseudocubic lattice parameters), the effect on D_V is likely to be small, too. Hence, we conclude that it is low n_V that is primarily responsible for the low D^*_O.

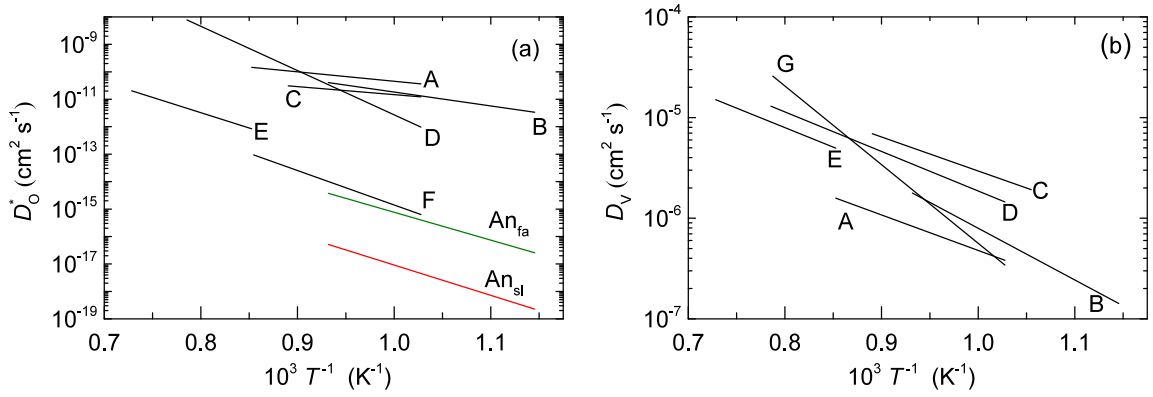

Figure 4.11: Comparison of selected oxygen (a) tracer diffusion and (b) vacancy diffusion coefficients: An_s and An_f this work; A – $BaTiO_3$ single crystals[25]; B – $LaAlO_3$ single crystals[29]; C – $SrTiO_3$ single crystals[27]; D – $LaCoO_3$ single crystals[24]; E – $LaFeO_3$[19]; F – $LaMnO_3$ ceramics[20]. All data refer to $200 \leq pO_2/\mathrm{mbar} \leq 1000$.

Two questions arise: Why is n_V so low? And why were two anion diffusion processes, An_{sl} and An_{fa}, observed? The answers to these two questions lie in a combination of $SrRuO_3$ displaying unusual defect chemistry and of PLD thin films being metastable systems. This combination also explains diverse questions concerning cation transport and morphological changes.

Specifically in contrast to the vast majority of perovskite oxides, $SrRuO_3$ has a strong tendency towards oxygen hyperstoichiometry, with the excess oxygen coming from cation vacancies rather than oxygen interstitials. There is thus a strong similarity with the well-known oxygen excess perovskite $LaMnO_3$.[34] The predominant cation vacancies in this case are on the Ru sublattice, and hence the chemical composition is $SrRu_{1-z}O_3$.[35] These negatively charged Ru vacancies are compensated by positively charged electrons holes, as in the analogous case of $LaMnO_3$.[36,37] Investigations of $SrRuO_3$'s electrical properties[38,39] indicate that electron holes are the majority charge carriers. Hence, the charge neutrality equation can be approximated by

$$4 \cdot [V''''_{Ru}] \approx [h^{\bullet}]. \tag{4.4}$$

$SrRuO_3$ thin films deposited by PLD exhibit a significant Ru deficiency,[40] but also contain probably more Sr vacancies than stipulated by equilibrium thermodynamics. Such high concentrations of vacancies on both cation sublattices are expected for films grown by a non-equilibrium process, such as PLD, as evidenced by studies[41,42] of cation defects in PLD thin films of $SrTiO_3$. The chemical formula of thin-film strontium ruthenate in its as-deposited state is thus $Sr_{1-y}Ru_{1-z'}O_3$, with $y < z'$ and $z' > z$. The time-dependent behavior observed for anion and cation diffusion arises from these metastable films reducing their Ru deficiency. And they do so by expelling superfluous SrO and O_2 from the lattice,

$$Sr^{\times}_{Sr} + 3O^{\times}_{O} + V''''_{Ru} + 4h^{\bullet} \longrightarrow SrO(s) + O_2(g) \tag{4.5}$$

That is, one formula unit of $SrRuO_3$ lattice sites is annihilated, and SrO forms as a second phase at the sample surface. This decomposition reaction accounts for the appearance on the $SrRuO_3$ surface (in the atomic force micrographs, Fig. 4.1) of pits (annihilated formula units) and of the small islands of SrO. The observed decrease in the out-of-plane lattice parameter is also consistent with a decrease in the amount of Ru deficiency.[35,40]

Oxygen vacancies, in any case, are minority defects: they do not appear in Eq. (4.4). Their concentration is governed by the Schottky disorder equilibrium,

$$Sr^{\times}_{Sr} + Ru^{\times}_{Ru} + 3O^{\times}_{O} \rightleftharpoons V''_{Sr} + V''''_{Ru} + 3V^{\bullet\bullet}_{O} + SrRuO_3(s), \tag{4.6}$$

with equilibrium constant,

$$K_{Sch}(T) = [V''_{Sr}][V''''_{Ru}][V^{\bullet\bullet}_{O}]^3. \tag{4.7}$$

Since V''''_{Ru} (and V''_{Sr}) are the dominant defects (and fixed through the PLD process), $[V^{\bullet\bullet}_{O}]$ is small. Consequently $n_V (\approx [V^{\bullet\bullet}_{O}]/[O^{\times}_{O}])$ and D^*_O are small, too.

Furthermore, the appearance of the two anion diffusion processes becomes clear: An_{sl} corresponds to diffusion in the metastable parent phase ($Sr_{1-y}Ru_{1-z'}O_3$), while An_{fa} corresponds to diffusion in the newly-forming daughter phase ($SrRu_{1-z}O_3$). We emphasize that the values of $D^*_O(An_{fa})$ we measured probably do not refer to the equilibrium daughter phase, but to various stages on the way to the daughter phase (see Fig. 4.14). Nevertheless, it is clear that a decrease in $[V''''_{Ru}]$ (and in $[V''_{Sr}]$) leads, according to Eq. (4.7), to an increase in the oxygen

vacancy concentration $[V_O^{\cdot\cdot}]$ from parent to daughter phases. And thus, as observed experimentally [Fig. 4.7(a)], oxygen diffusion in the daughter phase is faster than in the parent phase. That the activation enthalpy of oxygen tracer diffusion is the same for An_{sl} and An_{fa} is an additional indication that the two processes simply reflect differing concentrations of oxygen vacancies in parent and daughter phases and differ neither in mechanism nor in path.

Activation enthalpies

In the preceding section the low concentration of oxygen vacancies and the pivotal importance of cation defects were emphasiseed. This raises the question of why the oxygen vacancy concentration in $SrRuO_3$ is so low. One potential explanation can be found by identifying general trends in perovskite oxides:

We start from a completely stoichiometric ABO_3 perovskite, in which (i) all A, B and O sublattices are fully occupied and (ii) the B transition-metal cation is formally characterised by a d^4 configuration. A more favorable electron configuration is either d^5 or d^3. Let us assume that the latter is preferred, that is, the B cation would like (at least partially) to be oxidised, and one method to achieve this is to incorporate oxygen into the material. There are, however, no vacant sites on the oxygen sublattice, and the formation of oxygen interstitials is energetically prohibited in the close-packed ABO_3 perovskite lattice (see Sec. 2.3.1). The alternative is to create a cation-deficient compound, *e.g.*, $ABO_3 + \frac{2y}{1-y}O_2 \rightarrow A_{1-y}B_{1-y}O_3$.[43] Since Mn^{3+} is formally $3d^4$, and Ru^{4+} is $4d^4$, this simple picture provides an explanation for both $LaMnO_3$ and $SrRuO_3$ being oxygen-excess / cation-deficient perovskites. It strongly suggests that their defect structures will be similiar, too.

This potential similarity is further supported by comparison of he measured activation enthalpies of oxygen tracer diffusion, $\Delta H_{D_O^*}$, which are around $\Delta H_{D_O^*} \approx 2.2\,\text{eV}$ for both systems. From Eq. (4.3) (cf. Sec. 2.5), one finds that $\Delta H_{D_O^*}$ is the sum of the two terms,[27]

$$\Delta H_{D_O^*} = \Delta H_{\text{mig,V}} + \Delta H_{\text{gen,V}} \tag{4.8}$$

where $\Delta H_{\text{mig,V}}$ is the activation enthalpy for vacancy migration, $\Delta H_{\text{gen,V}}$ is the generation enthalpy of oxygen vacancies, and reflects the change in vacancy concentration with temperature.

In Table 4.1 $\Delta H_{\text{mig,V}}$ is seen to be between 0.6 eV and 1 eV for most perovskite oxides. Consequently one could assume $\Delta H_{\text{gen,V}}$ to be of the order of at least 1 eV.

Looking at the compiled values for $\Delta H_{\text{gen,V}}$ in the same table, however, reveals that assuming a value for $\Delta H_{\text{gen,V}}$ of the order of 1 eV might in both systems be an underrating of $\Delta H_{\text{gen,V}}$. For $LaMnO_3$ this problem has already been identified among others by Lee and Morgan[22] as well as by De Souza and Kilner[31]. One attempt to explain this behaviour is the assumption of a charge-disproportionation reaction, which is part of the defect chemical model of $LaMnO_3$.[44–47]

Lee and Morgan[22], for instance, used a charge-disproportionation reaction to bring experimental values and the results of *ab-initio* calculations in accordance.

Furthermore the assumption of charge-disproportionation in accordance with Goodenough et al.'s[48] bad-metal conduction picture of $LaMnO_3$ at high temperatures.[22]

Since $SrRuO_3$ is one of the archetype bad-metals, this, again, strongly suggests similar defect-structures of $LaMnO_3$ and $SrRuO_3$ and emphasizes their unique position within the perovskite oxide family.

Furthermore by Ru^{4+} disproportionating to Ru^{3+} and Ru^{5+} energetically favourable d^5 or d^3 electron configurations would be established. An_{sl} and An_{fa} exhibit the same activation enthalpies, despite corresponding to different cation as well as anion vacancy concentrations in the sample. This questions a competing model according to Lankhorst et al.[49] sometimes used[31] to explain a reduction of $\Delta H_{mig,V}$ in $LaMnO_3$, as this model strongly relies on deviations in cation stoichiometry.

Surface exchange

In this last part of the discussion, I will focus on the oxygen reduction reaction (ORR), particularly on the values obtained for the surface exchange coefficients k^*_O. Comparing the surface exchange coefficients for the two different observed processes, An_{fa} and An_{sl}, it is evident that for the slow diffusion mechanism An_{sl} the surface exchange is slow too.

SrO is known to drastically hamper surface exchange kinetics.[6,50] Jung and Tuller[6] proposed two mechanism potentially being responsible for this phenomenon: Either a limited electron transfer through a dense SrO layer or a limited active surface area where the ORR can take place is responsible for a reduced k^*_O.

AFM-micrographs and the complementing PEEM-analysis conducted in this work show that SrO is not present as a dense cover layer, but rather as surface precipitates. This strongly suggests that a limited surface area is involved in the ORR, which results a reduction of active surface sites for the ORR to take place and eventually leads to a diminished k^*_O. Whereas the relative relation between in $k^*_O(An_{sl})$ and $k^*_O(An_{fa})$ seem understandable, the more intriguing question arises when comparing the obtained temperature dependent surface exchange coefficients with those of other perovskite oxides.

It is striking that $SrRuO_3$ is the material with the lowest values for k^*_O, both absolute (Fig. 4.12 (a)) as well as when taking D^*_O into account (Fig. 4.12 (b)). This is especially peculiar as according to De Souza[51] a material with a low concentration of oxygen vacancies and a high concentration of electronic charge carriers should exhibit a particularly high surface exchange rate k^*_O. Here it might be important to note that in $SrRuO_3$ the electronic charge carriers are holes, but for the rate determining step of the oxygen incorporation reaction electrons are required.[52] Furthermore it is not clear in what way the oxygen vacancy concentration in the outermost surface layers facilitates the ORR as these vacancies would expose the transition metal cation (Ru) in the subsurface-layer.[53] In this context the electronic structure of the surface, which is influenced by the transition metal cation, seems to be of crucial importance.[54]

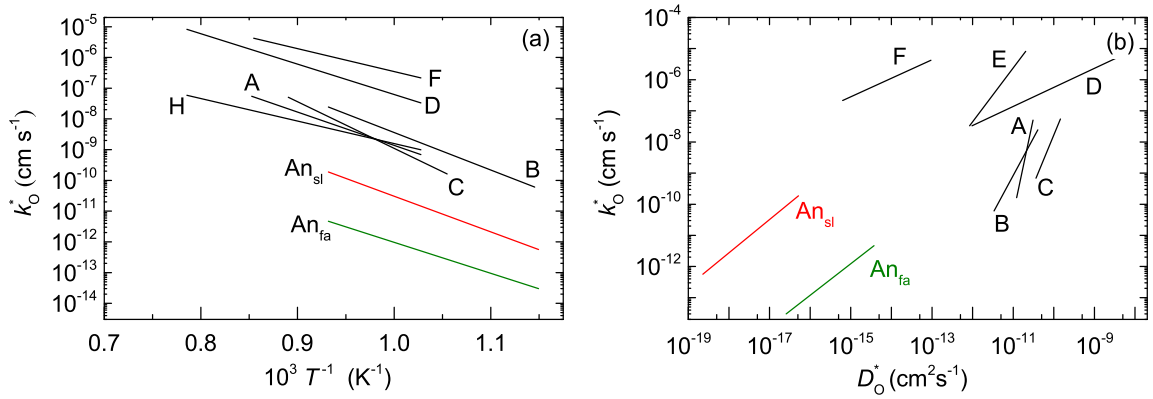

Figure 4.12: Comparison of selected oxygen surface exchange coefficients for different perovskite oxides: An_s and An_f this work; A – $BaTiO_3$ single crystals[25]; B – $LaAlO_3$ single crystals[29]; C – $SrTiO_3$ single crystals[27]; D – $LaCoO_3$ single crystals[24]; E – $LaFeO_3$[19]; F – $LaMnO_3$ ceramics[20]. H – $LaSrMnO_3$ ceramics[31] All data refer to $200 \leq pO_2/\text{mbar} \leq 1000$.

4.2.2 Cation diffusion

Before discussing the Ti diffusion data, three comments shall be made. First, Ti resides most likely on the Ru sublattice in $SrRuO_3$ on account of the similar ionic radii of the two ions in sixfold (VI) coordination:[55] $r^{\text{VI}}_{\text{Ru}^{4+}} = 0.62$ Å; $r^{\text{VI}}_{\text{Ti}^{4+}} = 0.605$ Å. Second, the asymmetry in the cation diffusion process—Ti diffuses into $SrRuO_3$, but there is no measurable Ru diffusion into $SrTiO_3$—can be explained by the relative concentrations of *B*-site vacancies in the two materials. In $SrRuO_3$, there is a high concentration of empty sites available for Ti to occupy (V''''_{Ru} is high), but in $SrTiO_3$, there is a lack of available sites for Ru to occupy (V''''_{Ti} is low), and hence, appreciable diffusion is only apparent in one medium. Third, the chemical diffusion of Ti as a neutral component into $SrRuO_3$ requires the ambipolar diffusion of Ti^{4+} and another charged species. The obvious possibility is oxygen ions. The in-diffusion process corresponds, therefore, to TiO_2 as a chemical component being incorporated in miniscule amounts into $SrRuO_3$, thereby generating V''''_{Ti} and $2V^{\bullet\bullet}_{\text{O}}$ in $SrTiO_3$. Because anions are more mobile than cations in ABO_3 perovskites (compare Fig. 4.11 and Fig. 4.13), the chemical diffusion of Ti will be governed by the diffusion of the cations.

With regard to the two diffusion processes, the faster process that disappears with increasing anneal time, Cat_{fa}, can be assigned to diffusion in the parent phase with its higher Ru deficiency. The slower process that becomes more dominant with increasing anneal time, Cat_{sl}, then corresponds to diffusion in the daughter phase, with its diminished Ru deficiency (see Fig. 4.14).

In Fig. 4.13, the here reported data is compared with data reported in the literature for cation diffusion in perovskite oxides.[56–60,63] In terms of the absolute magnitude, the here measured values agree well with literature data. There are, however, two issues that are unclear. First, a comparison of the measured activation enthalpy $\Delta H_{D_{\text{Ti}}} = (4.3 \pm 0.3)$ eV with literature data (see Table 4.2)) suggests $\Delta H_{\text{gen,V}}$ to be close to zero, whereas the concentration of Ru vacancies is expected to decrease with increasing temperature, *i.e.* $\Delta H_{\text{gen,V}}$ should be negative

Cation in Perovskite	$\Delta H_{D_{\mathrm{Cat}}}$ (eV)	Ref.
Ti in $SrRuO_3$	(4.3 ± 0.3)	this work
Mn in $LaMnO_3$	(0.6 ± 0.1)	56
Pr in $LaMnO_3$	(1.3 ± 0.1)	57
Mn in (Ba,Sr)(Co,Fe)O_3	(3.9 ± 0.6)	58
Sr in (La,Sr)CoO_3	(3.5 ± 0.4)	59
Zr in $BaTiO_3$	(5.1 ± 0.6)	60
Sr in $BaTiO_3$	(5.6 ± 1.2)	60
Ti in $SrTiO_3$	~ 3.3	58
Sr in $SrTiO_3$	(4.0 ± 0.3)	61
V_{Ti} in $BaTiO_3$	(3.9 ± 0.7)	62

Table 4.2: Comparison of activation enthalpies for cation diffusion in various ABO_3 perovskite oxides.

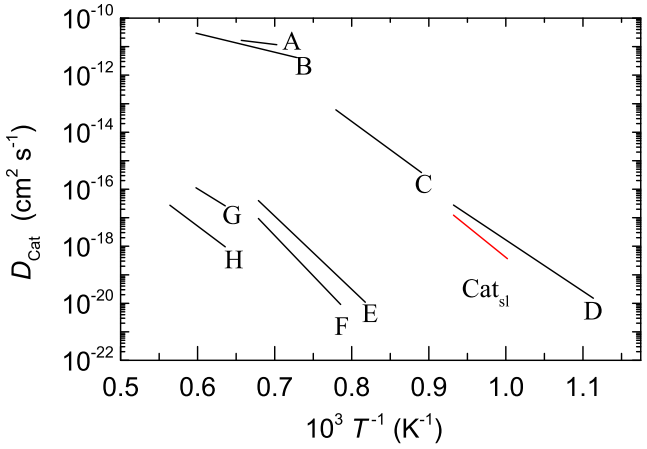

Figure 4.13: Comparison of cation diffusion coefficients in selected ABO_3 perovskites: Ti(Cat_{sl}) in $SrRuO_3$ thin-films – this work; A – Mn in $LaMnO_3$ ceramics[56]; B – Pr in $LaMnO_3$ ceramics[57]; C – Mn in (Ba,Sr)(Co,Fe)O_3 ceramics[63]; D – Sr in (La,Sr)CoO_3 thin-films[59]; E – Zr in $BaTiO_3$ single crystals[60]; F – Sr in $BaTiO_3$ single crystals[60]; G – Ti in $SrTiO_3$ single crystals[58]; H – Sr in $SrTiO_3$ single crystals[61]

(*cf.* $LaMnO_3$[56]). Second, our data are remarkably close to data obtained by Kubicek *et al.*[59] for Sr diffusion in (La,Sr)CoO_3, and it is unclear if this is due to both studies being conductued on thin-film samples.

4.3 Conclusions

Through investigations of oxygen tracer diffusion and titanium diffusion, the behavior of point defects in thin-film $SrRuO_3$ was revealed to be surprisingly complex. The following points are emphasized:

- Thin-film samples of perovskite oxides (*e.g.* $SrRuO_3$) produced by PLD possess a metastable point-defect structure. Given sufficient time and/or temperature, such systems will relax to equilibrium.

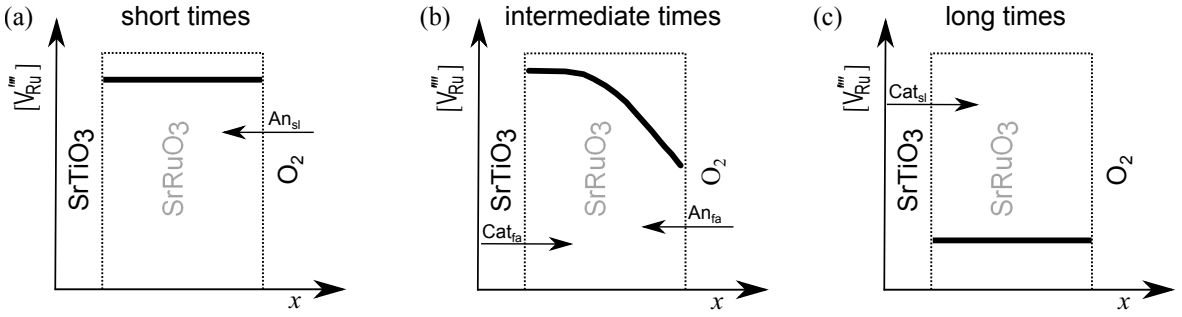

Figure 4.14: Schematic summary of operative diffusion processes and the time regimes in which they are probed. At short anneal times (a), the films can be considered as as-deposited: the decomposition reaction [Eq. (4.5)] has yet to proceed appreciably, as the cations are comparatively slow. Oxygen diffusion, being much faster, is observable as $\mathrm{An_{sl}}$. At intermediate times (b), cation mobility starts to be evident through the observation of $\mathrm{Cat_{fa}}$ and the appearance of $\mathrm{An_{fa}}$. These two processes refer to different phases because they occur at different interfaces, $\mathrm{Cat_{fa}}$ at $\mathrm{SrTiO_3}|\mathrm{SrRuO_3}$; $\mathrm{An_{fa}}$ at $\mathrm{SrRuO_3}|\mathrm{O_2(g)}$. Note $D^*_{\mathrm{O}}(\mathrm{An_{fa}})$ shows enlarged scatter because the composition of the daughter phase is continually changing as diffusion is being probed. At long anneal times (c), the films' relaxation to the final equilibrium state has progressed furthest, and $\mathrm{Cat_{sl}}$ is observed. Anion diffusion was not examined at such long times due to the prohibitively high surface roughness.

- The multiple anion and cation diffusion processes that were observed refer to transport in the metastable parent and the newly forming daugther phases.
- The physical properties of PLD thin-film systems may differ considerably from those of single crystals or bulk ceramics. The appearance of SrO at the sample surface, for example, is due to the metastable nature of PLD thin-films, not due to surface segregation. On the one hand, this means that care is therefore required when comparing PLD thin films with other systems. On the other hand, it means that PLD can fabricate point-defect structures far from equilibrium.
- Compared with most other $AB\mathrm{O_3}$ perovskites, the diffusion of oxygen in $\mathrm{SrRuO_3}$ is found to be abnormally slow. Thus, thin-film $\mathrm{SrRuO_3}$, when used as an electrode, acts effectively as a diffusion barrier for oxygen, and oxygenating underlying oxide layers in an oxide heterostructure will be prolonged severely.
- A further striking issue is the magnitude of the measured activation enthalpies of oxygen diffusion. Here the fact that $\mathrm{SrRuO_3}$ exhibits bad-metal behaviour seems to open a promising way for future endeavour in connecting defect chemistry and electronic properties of this material.

Bibliography

[1] J. Shin, S. Kalinin, H. Lee, H. Christen, R. Moore, E. Plummer and A. Baddorf, *Surf. Sci.*, 2005, **581**, 118 – 132.
[2] D. Halley, C. Rossel, D. Widmer, H. Wolf and S. Gariglio, *Mater. Sci. Eng., B*, 2004, **109**, 113 – 116.
[3] H. N. Lee, H. M. Christen, M. F. Chisholm, C. M. Rouleau and D. H. Lowndes, *Appl. Phys. Lett.*, 2004, **84**, 4107–4109.
[4] M. Mlynarczyk, K. Szot, A. Petraru, U. Poppe, U. Breuer, R. Waser and K. Tomala, *J. Appl. Phys.*, 2007, **101**, 023701.
[5] S. Wicklein, A. Sambri, S. Amoruso, X. Wang, R. Bruzzese, A. Koehl and R. Dittmann, *Appl. Phys. Lett.*, 2012, **101**, –.
[6] W. Jung and H. L. Tuller, *Energy Environ. Sci.*, 2012, **5**, 5370–5378.
[7] K. Szot, W. Speier, U. Breuer, R. Meyer, J. Szade and R. Waser, *Surf. Sci.*, 2000, **460**, 112 – 128.
[8] E. J. Crumlin, E. Mutoro, Z. Liu, M. E. Grass, M. D. Biegalski, Y.-L. Lee, D. Morgan, H. M. Christen, H. Bluhm and Y. Shao-Horn, *Energy Environ. Sci.*, 2012, **5**, 6081–6088.
[9] R. Bertacco, J. Contour, A. Bartholemy and J. Olivier, *Surf. Sci.*, 2002, **511**, 366 – 372.
[10] R. A. De Souza and R. J. Chater, *Solid State Ionics*, 2005, **176**, 1915 – 1920.
[11] J. Crank, *The Mathematics Of Diffusion*, Claredon Press, Second Edition edn., 1975.
[12] S. Hofmann, *Rep. Prog. Phys.*, 1998, **61**, 827.
[13] A. Atkinson, *Solid State Ionics*, 1984, **12**, 309 – 320.
[14] H. Mehrer, *Diffusion in solids: fundamentals, methods, materials, diffusion-controlled processes*, Springer, 2007, vol. 155.
[15] L. G. Harrison, *Trans. Faraday Soc.*, 1961, **57**, 1191–1199.
[16] A. Le Claire and A. Rabinovitch, *J. Phys. C Solid State*, 1981, **14**, 3863.
[17] A. D. Le Claire, *Br. J. Appl. Phys.*, 1963, **14**, 351.
[18] Y.-C. Chung and B. J. Wuensch, *J. Appl. Phys.*, 1996, **79**, 8323–8329.
[19] T. Ishigaki, S. Yamauchi, K. Kishio, J. Mizusaki and K. Fueki, *J. Solid St. Chem.*, 1988, **73**, 179 – 187.
[20] A. Berenov, J. MacManus-Driscoll and J. Kilner, *Solid State Ionics*, 1999, **122**, 41–49.
[21] A. Belzner, T. M. Gür and R. A. Huggins, *Solid State Ionics*, 1992, **57**, 327 – 337.
[22] Y.-L. Lee and D. Morgan, *Phys. Chem. Chem. Phys.*, 2012, **14**, 290–302.
[23] J. van Roosmalen and E. Cordfunke, *J. Solid State Chem.*, 1994, **110**, 113 – 117.
[24] T. Ishigaki, S. Yamauchi, J. Mizusaki, K. Fueki and H. Tamura, *J. Solid St. Chem.*, 1984, **54**, 100 – 107.
[25] M. F. Kessel, *Ph.D. thesis*, RWTH-Aachen University, 2012.
[26] D.-K. Lee and H.-I. Yoo, *Solid State Ionics*, 2001, **144**, 87–97.
[27] R. A. De Souza, V. Metlenko, D. Park and T. E. Weirich, *Phys. Rev. B*, 2012, **85**, 174109.
[28] L. Walters and R. Grace, *J Phys. Chem. Solids*, 1967, **28**, 239 – 244.
[29] C. Schwab, H. Schraknepper and R. A. De Souza, unpublished.
[30] J. Mizusaki, I. Yasuda, J. Shimoyama, S. Yamauchi and K. Fueki, *J. Electrochem. Soc.*, 1993, **140**, 467–471.
[31] R. A. De Souza and J. A. Kilner, *Solid State Ionics*, 1998, **106**, 175–187.
[32] R. Al-Hamadany, J. P. Goss, P. R. Briddon, S. A. Mojarad, M. Al-Hadidi, A. G. O'Neill and M. J. Rayson, *J. Appl. Phys.*, 2013, **113**, –.
[33] M. Kubicek, Z. Cai, W. Ma, B. Yildiz, H. Hutter and J. Fleig, *ACS Nano*, 2013, **7**, 3276–3286.
[34] J. Töpfer and J. B. Goodenough, *Chem. Mater.*, 1997, **9**, 1467–1474.
[35] B. Dabrowski, O. Chmaissem, P. W. Klamut, S. Kolesnik, M. Maxwell, J. Mais, Y. Ito, B. D. Armstrong, J. D. Jorgensen and S. Short, *Phys. Rev. B*, 2004, **70**, 014423.
[36] J. van Roosmalen and E. Cordfunke, *J. Solid St. Chem.*, 1994, **110**, 109 – 112.
[37] J. A. Alonso, M. J. Martinez-Lope, M. T. Casais, J. L. Macmanus-Driscoll, P. S. I. P. N. de Silva, L. F. Cohen and M. T. Fernandez-Diaz, *J. Mater. Chem.*, 1997, **7**, 2139–2144.
[38] T. Maekawa, K. Kurosaki, H. Muta, M. Uno and S. Yamanaka, *J. Alloys Compd.*, 2005, **387**, 56–59.
[39] S. C. Gausepohl, M. Lee, R. A. Rao and C. B. Eom, *Phys. Rev. B*, 1996, **54**, 8996–8999.
[40] W. Siemons, G. Koster, A. Vailionis, H. Yamamoto, D. H. A. Blank and M. R. Beasley, *Phys. Rev. B*, 2007, **76**, 075126.
[41] D. J. Keeble, S. Wicklein, R. Dittmann, L. Ravelli, R. A. Mackie and W. Egger, *Phys. Rev. Lett.*, 2010, **105**, 226102.
[42] D. J. Keeble, S. Wicklein, L. Jin, C. L. Jia, W. Egger and R. Dittmann, *Phys. Rev. B*, 2013, **87**, 195409.
[43] J. V. Roosmalen, E. Cordfunke, R. Helmholdt and H. Zandbergen, *J. Solid State Chem.*, 1994, **110**, 100 – 105.
[44] D. S. Mebane, Y. Liu and M. Liu, *Solid State Ionics*, 2008, **178**, 1950–1957.
[45] F. W. Poulsen, *Solid State Ionics*, 2000, **129**, 145–162.
[46] J. Nowotny and M. Rekas, *J. Am. Ceram. Soc.*, 1998, **81**, 67–80.

[47] H. Kamata, Y. Yonemura, J. Mizusaki, H. Tagawa, K. Naraya and T.-i. Sasamoto, *J. Phys. Chem. Solids*, 1995, **56**, 943–950.
[48] J. Goodenough, J.-S. Zhou, F. Rivadulla and E. Winkler, *J. Solid State Chem.*, 2003, **175**, 116–123.
[49] M. H. Lankhorst, H. Bouwmeester and H. Verweij, *J. Solid State Chem.*, 1997, **133**, 555 – 567.
[50] S. Jiang and J. Love, *Solid State Ionics*, 2001, **138**, 183–190.
[51] R. A. De Souza, *Phys. Chem. Chem. Phys.*, 2006, **8**, 890–897.
[52] R. Merkle and J. Maier, *Angew. Chem. Int. Ed.*, 2008, **47**, 3874–3894.
[53] J. Druce, H. Tellez, M. Burriel, M. Sharp, L. Fawcett, S. Cook, D. McPhail, T. Ishihara, H. Brongersma and J. Kilner, *Energy Environ. Sci.*, 2014, **7**, 3593–3599.
[54] D. N. Mueller, M. L. Machala, H. Bluhm and W. C. Chueh, *Nat. Commun.*, 2015, **6**, 6097.
[55] R. D. Shannon and C. T. Prewitt, *Acta Crystallogr., Sect. B: Struct. Sci*, 1969, **25**, 925–946.
[56] S. Miyoshi and M. Martin, *Phys. Chem. Chem. Phys.*, 2009, **11**, 3063–3070.
[57] M. Palcut, J. S. Christensen, K. Wiik and T. Grande, *Phys. Chem. Chem. Phys.*, 2008, **10**, 6544–6552.
[58] K. Gomann, G. Borchardt, A. Gunhold, W. Maus-Friedrichs and H. Baumann, *Phys. Chem. Chem. Phys.*, 2004, **6**, 3639–3644.
[59] M. Kubicek, G. M. Rupp, S. Huber, A. Penn, A. K. Opitz, J. Bernardi, M. Stoger-Pollach, H. Hutter and J. Fleig, *Phys. Chem. Chem. Phys.*, 2014, **16**, 2715–2726.
[60] S. Koerfer, R. A. De Souza, H.-I. Yoo and M. Martin, *Solid State Sci.*, 2008, **10**, 725 – 734.
[61] K. Gomann, G. Borchardt, M. Schulz, A. Gomann, W. Maus-Friedrichs, B. Lesage, O. Kaitasov, S. Hoffmann-Eifert and T. Schneller, *Phys. Chem. Chem. Phys.*, 2005, **7**, 2053–2060.
[62] W. Preis and W. Sitte, *Solid State Ionics*, 2006, **177**, 3093–3098.
[63] S. P. Harvey, R. A. De Souza and M. Martin, *Energy Environ. Sci.*, 2012, **5**, 5803–5813.

Chapter 5

The ruthenium deficiency in $SrRuO_3$ thin-films: A variation and its impact on basic film properties

The optimization of deposition parameters is indispensable for the successful growth of thin-films by means pulsed laser deposition (PLD). In the case of $SrRuO_3$, film properties are drastically affected by the choice of deposition temperature T_S,[1–3] the oxygen background pressure pO_2[2,4,5] as well as the laser fluence J_L.[6] A major general obstacle for PLD growth of $SrRuO_3$ is Ru loss during deposition, which prohibits the growth of perfectly stoichiometric $SrRuO_3$ thin-films.[7,8] In the preceding chapter (Chapter 4) the paramount importance of this Ru non-stoichiometry for the film's complex defect behaviour was emphasized. Deliberately adjusting the Ru deficiency would provide further insights into the defect chemistry of $SrRuO_3$.

The main argument presented for the phenomenon of Ru loss during PLD deposition is the thermodynamic instability of several Ru species,[7,8] such as RuO_4 and RuO_3.[8][1]

When recalling the major principle of PLD, however, one finds that it is the prevalence of kinetics over thermodynamics that mainly facilitates the deposition of materials, particularly that of complex oxides (cf. Sec. 3.2.1 and Refs. [9,10]). Therefore it seems peculiar that mostly thermodynamics arguments are used to explain the Ru deficit in $SrRuO_3$ thin-films.

The underlying idea of the study presented in this chapter is to investigate the impact of deposition kinetics on the Ru deficiency. The hypothesis is that a variation in deposition frequency f kinetically hampers the reactions leading to Ru loss during deposition. It will be shown that an increase of the deposition frequency f is sufficient to systematically increase the cation off-stoichiometry and in this manner influence structural, electrical as well as oxygen-defect and disorder properties in $SrRuO_3$ thin films.

In the first section the differences to the standard deposition conditions described in Sec. 3.2.3 will be outlined. This is followed by the presentation of the results obtained. Here first a characterisation of the varying structural film properties is given. Then the results regarding

[1] The main species here are RuO_4 and RuO_3.[8] In this study it was not determined which of the several volatile ruthenium species evaporates, I will refer to them as RuO_x.

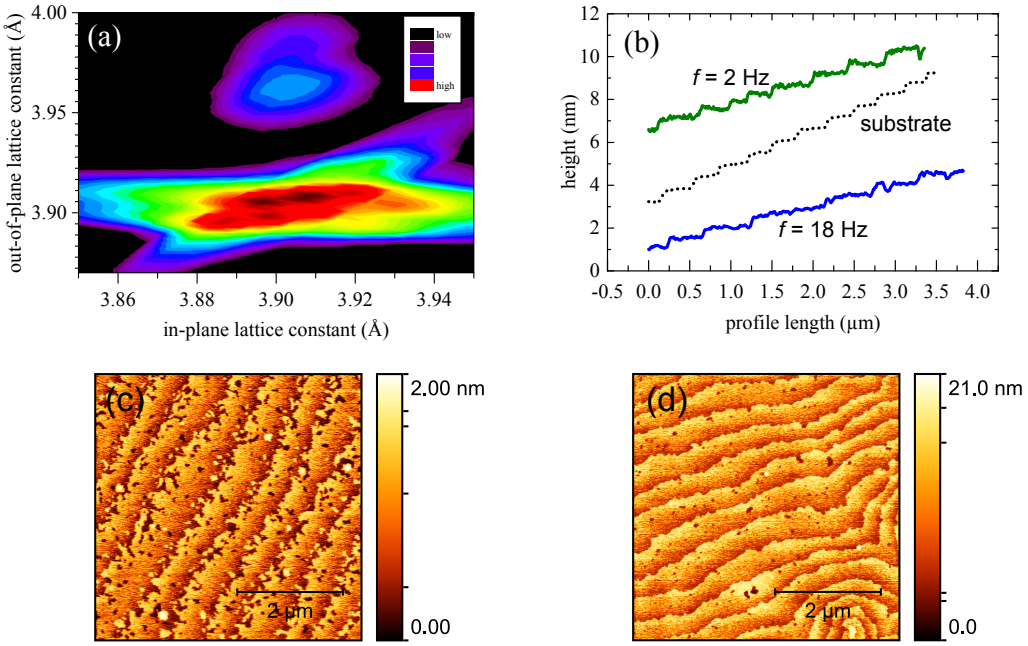

Figure 5.1: Exemplary result from characterization of an $SrRuO_3$ thin-film: (a) Reciprocal space mapping confirms the coherence of the in-plane lattice parameter of film and substrate. (b) line profiles across the step-edges confirm resemblance with the $SrTiO_3$ substrate (deposition conditions in particular case: $f = 18\,\mathrm{Hz}$ step-length $l_\mathrm{T} = 240\,\mathrm{nm}$ and $f = 2\,\mathrm{Hz}$ step-length $l_\mathrm{T} = 450\,\mathrm{nm}$) AFM micrograph of as deposited films with (c) $f = 18\,\mathrm{Hz}$ and (d) $f = 2\,\mathrm{Hz}$

oxygen diffusion are presented. Finally the differences in electrical properties of the different films are shown. The subsequent discussion is structured in the same manner.

5.1 Modified deposition conditions

All samples used in the present section were deposited at a deposition temperature of $T_\mathrm{Dep} = 873\,\mathrm{K}$. The reduction of the deposition temperature compared to the standard conditions (see Sec. (3.2.3)) was carried out for two reasons: First, to reduce loss of volatile RuO_x [8] species during deposition (see for instance Ref. [6]). Second, to extend the parameter space available for variation of the deposition frequency. Here Hong et al. [11] showed that by reducing T_Dep and choosing substrates with a small terrace width l_T of the vicinal step-structure ($l_\mathrm{T} \leq 500\,\mathrm{nm}$), the conditions for step-flow growth to occur are less sensitive to variation of deposition frequency f (cf. Fig. 1 in Ref. [11]). The choice of substrates with a terrace width of $l_T \leq 500\,\mathrm{nm}$ and a deposition temperature of $T_\mathrm{Dep} = 873\,\mathrm{K}$ thus allowed for the growth of $SrRuO_3$ thin-films with frequencies ranging from $f = 2\,\mathrm{Hz}$ to $f = 18\,\mathrm{Hz}$ without changing the basic growth mode. The oxygen partial pressure and the laser fluence were not altered compared to the values reported in Sec. 3.2.3. [$pO_2 = 0.133\,\mathrm{mbar}$; $J_\mathrm{L} \approx 1\,\mathrm{J\,cm^{-2}}$]

5.2 Results

5.2.1 Structure and Stoichiometry

All films considered in this study exhibit atomically flat morphology similar to the vicinal step-structure of the $SrTiO_3$ substrate. Deposition at high frequencies resulted in more facetted step-structure than when depositing at low frequencies (Compare Fig. 5.1 (c) for high and (d) for low frequencies). Quantification of this phenomenon by different measures such as step-length and width of island or length of facet free area on the steps did not reveal any dependence on the frequency, but remained in the same order as the substrate step-length. The epitaxial relationship between film and substrate was confirmed by means of reciprocal space mapping around the (103) $SrTiO_3$ peak (Fig. 5.1 (a)) exemplary shown for the highest frequency $f = 18\,\mathrm{Hz}$). ω-scans revealed rocking-curve widths of $FWHM \approx 0.03°$ for all films; no significant differences in $FWHM$ between the films were observed.

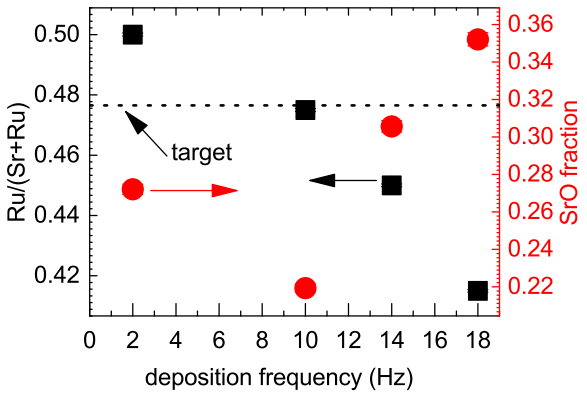

Figure 5.2: Results of an investigation of the film's composition by means of XPS. With increasing deposition frequency the Ru-content decreases. Furthermore an SrO component is observed. The fraction of this component increases with increasing deposition frequency.[2]

Granted that the film's in-plane lattice parameter is clamped to the $SrTiO_3$ substrate, $2\Theta - \omega$ scans probe the out-of-plane lattice parameter from which the strain-state ϵ of the film can be derived according to

$$\epsilon = \frac{c_{\mathrm{pc}} - a_{0\mathrm{pc}}}{a_{0\mathrm{pc}}} \tag{5.1}$$

with c_{pc} being the film's out-of-plane lattice parameter derived from XRD-scans in Fig. 5.3 (a) and $a_{0pc} = 3.93\,\text{Å}$ being the pseudocubic lattice parameter of bulk $SrRuO_3$.[12,13]

Values for c_{pc} and ϵ are depicted in Fig. 5.3 (b). It is evident that an increase in deposition frequency f results in increased tensile strain in the out-of-plane direction. The composition of the same set of films was investigated in the as-deposited state by means of X-ray photoelectron spectroscopy (XPS). The results can be summarized as follows: Samples deposited at highest frequencies posses the lowest ruthenium content and thus more ruthenium vacancies (Fig. 5.2). A further observation is that the fraction of SrO increased as the ruthenium content decreased (Fig. 5.2). In other words deposition at low frequencies results in films with stoichiometric Sr:Ru ratio (Sr/(Sr+Ru) = 0.5) and thus enables congruent transfer of the target's composition. As the information depth of XPS is limited to first

[2] XPS data presented in this section were measured and processed by Christoph Bäumer (PGI-7, Forschungszentrum Jülich, Jülich, Germany)

few nm of the films, the values depicted in Fig. 5.8 (b) do not necessarily represent the true ratios in the bulk of the film. Nonetheless we consider the observed trend to reliably reflect differences between the samples. This is for two reasons: First the same trends were observed for XPS analysis with different incident angles of x-ray photons and therefore different depth of origin of the analysed electrons. Secondly the same correlation between ruthernium non-stochiomety and out-of-plane lattice parameters where observed in several previous studies.[7,14,15] In Sr rich perovskites there is the possibility that superfluous Sr is incorporated into the material as additional SrO rocksalt-layers, which results in the formation of so called Ruddlesden-Popper phases.[16–18] It has been shown that by ablating from a stoichiometric $SrRuO_3$ target, some members of the $SrRuO_3$ Ruddlesden-Popper series — $Sr_3Ru_2O_7$ and Sr_2RuO_4 — can successfully be grown.[6] In this study, however, no Ruddlesden-Popper (RP) phases were detected.

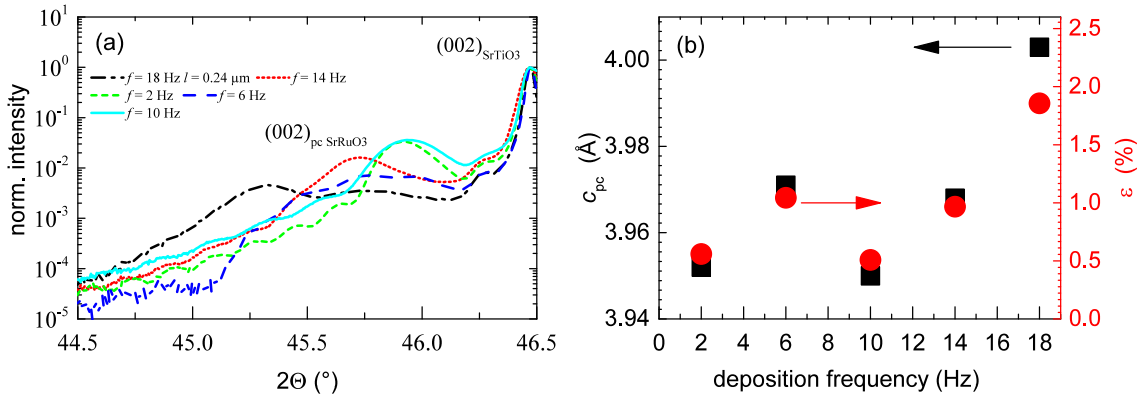

Figure 5.3: (a) XRD-scans of differently prepared $SrRuO_3$| $SrTiO_3$ heterorstructures. A shift in the $(002)_{pc}$ $SrRuO_3$ reflex towards lower 2Θ with increasing f is observed. Determining the out-of-plane lattice constant from these diffractograms (as done in Sec. (4.1.1)) results in the dependence depicted in (b). (b) Here the values for the out-of-plane lattice constant c_{pc} and the corresponding values for the strain ϵ are shown. With increasing deposition frequency both, c_{pc} and ϵ, increase.

5.2.2 Oxygen diffusion and surface exchange

The impact of deposition conditions on the oxygen sublattice was probed by means of isotope exchange experiments and subsequent SIMS analysis (see Sec. 3.3 for the detailed course of experiment). In Fig. 5.4 the resulting profiles of the corrected ^{18}O isotope fraction n_r^* after sample exposure to $^{18}O_2$ for one hour are shown.

Comparing the profiles in different samples, a significant increase in the diffusion-profile length with increasing f becomes apparent (Fig. 5.4 (a)). Evaluation of these profiles with the appropriate solution to the diffusion equation (cf. Sec. 4.1.2) thus yields an increase in the value for the tracer diffusion coefficients D_O^* with increasing deposition frequency. Concomitantly the value of the surface exchange coefficient k_O^* rises (Fig. 5.4) (b)). To extract the correct value for D_O^* and k_O^*, we ensured that no SIMS induced artifacts dominate the behaviour. This is the case for profiles longer than 15 nm. For this reason here, again, in some

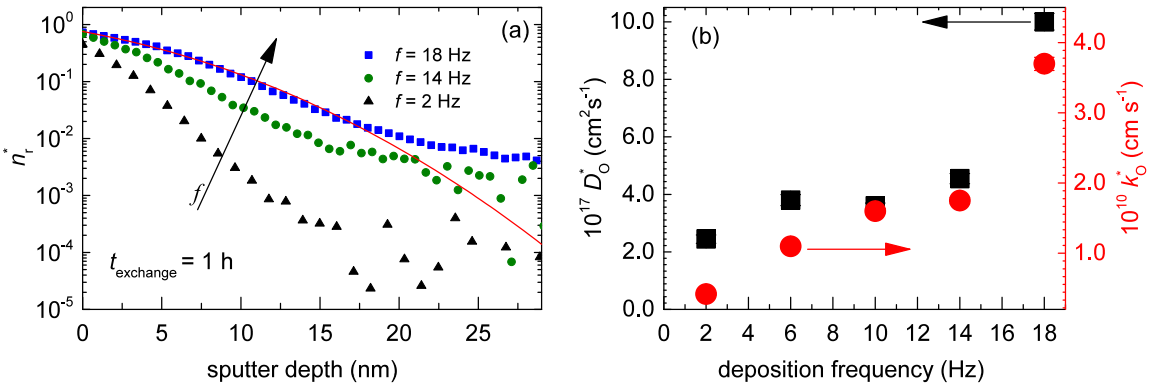

Figure 5.4: (a)Tracer diffusion profiles of differently deposited $SrRuO_3$ thin films. The larger frequency to ablate from the stoichiometric target, the longer the observed tracer diffusion profiles.(b) Extracted tracer diffusion coefficients and surface exchange coefficients as a function of deposition frequency. With increasing deposition frequency larger values are observed for both properties. The exchange experiments for the data shown in (a) and (b) were conducted at $T = 1023\,\mathrm{K}$ and $pO_2 = 500\,\mathrm{mbar}$ for an exchange time of $t_{ex} = 1\,\mathrm{h}$. The pre-anneal time t_{pre} was less than 30 min in all cases

cases a series of exchange experiments as a function of exchange time had to be conducted to obtained reliable values for D^* and k^* (cf. Sec. 4.1.2).

Diffusion profiles were obtained as a function of temperature for for different sets of samples. The resulting diffusion and surface exchange coefficients are depicted for three sets of samples in Fig. 5.5 (a) and (b). The Arrhenius analysis yields an activation enthalpy for the diffusion ($\Delta H_{D^*_O}$) as well as for the surface exchange coefficient ($\Delta H_{k^*_O}$) for each set of deposition parameters.

There is no clear trend in activation enthalpy, neither for $\Delta H_{D^*_O}$ nor for $\Delta H_{k^*_O}$, with increasing f discernible. There are also no other trends of ΔH_{D^*} or ΔH_{k^*} with e.g. the out-of-plane lattice parameter and thus the strain-state of the film present. In fact all acquired values for

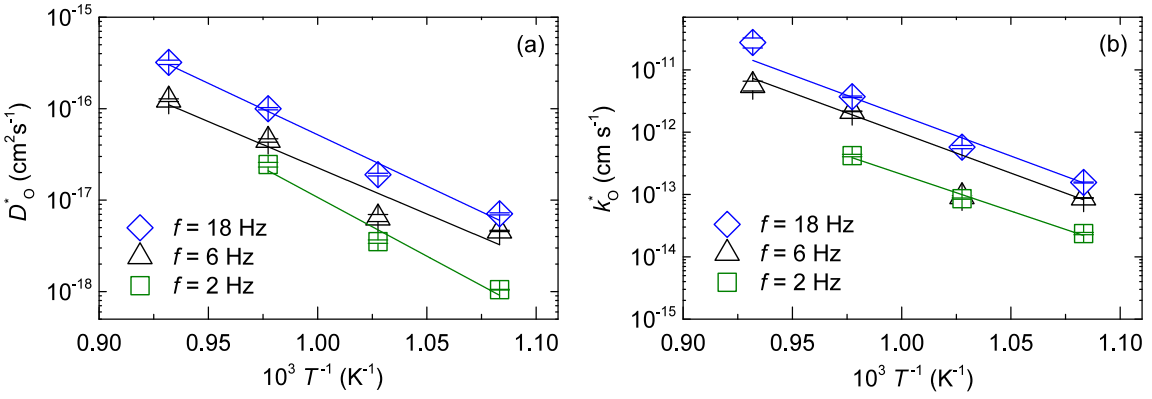

Figure 5.5: (a)Arrhenius plots for the tracer diffusion process in samples deposited at different frequencies. (b) The surface exchange coefficients exhibit Arrhenius-type behaviour as well. The corresponding activation enthalpies for both processes are depicted in Fig. 5.6. (Here the Arrhenius plot for $f = 10\,\mathrm{Hz}$ is not shown for clarity reasons.)

ΔH_{D^*} scatter around $\Delta H_{D^*_O} = (2.29 \pm 0.54)$ eV. In the same manner as $\Delta H_{D^*_O}$ the obtained data for $\Delta H_{k^*_O}$ behave. Here a mean of $\Delta H_{D^*_O} = (2.37 \pm 0.48)$ eV was determined. Both values are remarkably close to the values for the same properties obtained in the previous chapter for a set of samples deposited with different deposition parameters as the samples presented here(see Chapter 4). Combining the results from Chapter 4 and those presented here, one thus can conclude that the deposition conditions seem to have little influence on the activation enthalpies for the anion diffusion process. At first sight this is a peculiar observation; it will be further discussed in Sec. 5.3.2.

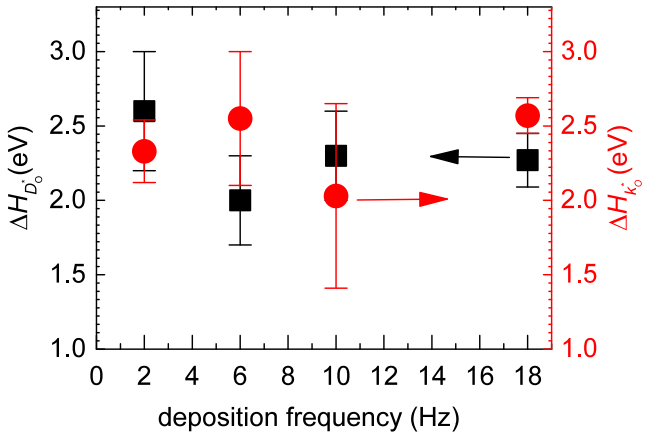

Figure 5.6: Activation enthalpies for oxygen tracer diffusion $\Delta H_{D^*_O}$ and surface exchange $\Delta H_{k^*_O}$, both as a function of deposition frequency. The corresponding Arrhenius plots are shown in Fig. (5.5)

5.2.3 Electrical and disorder properties

Besides characterizing structural and defect properties of the different films, temperature dependend measurements of the electric resistivity in the range of $2 \leq T/K \leq 300$ were performed. At first glance the different resistivity curves $\rho(T)$ (Fig. 5.7) exhibit similar shape over the whole temperature range, only a shift towards higher resistivities with increasing f is observed. The room-temperature $\rho_{300\,\mathrm{K}}$ and the residual resistivity $\rho_{2\,\mathrm{K}}$ can both be regarded as measures of this shift (see Fig. (5.8) (a)). The residual resistivity ratio (RRR) — here defined as $\rho_{300\,\mathrm{K}}/\rho_{2\,\mathrm{K}}$ and generally regarded as a

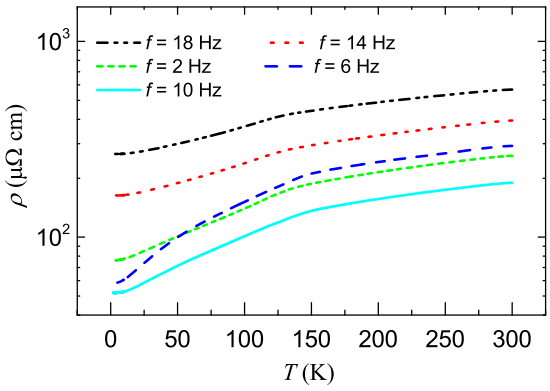

Figure 5.7: Temperature dependent resistivity measured in the range of $2 \leq T/K \leq 300$ for all films investigated.The measured curves are similar in shape, but shifted to overall higher resistivities with increasing f. (see Fig. 5.8 (a))[3]

measure of defect density in a crystal[19] — slightly decreases with increasing deposition frequency (see Fig. 5.8 (b)). Here a comparison with literature values of the RRR helps to assess the tendency observed. For PLD grown $SrRuO_3$ thin films the RRR can be as high as 34[20]. Most PLD grown thin films, however, exhibit an RRR below 7.[7,21,22] Especially the introduction of Ru-vacanies as additional scattering centres was identified as a reason for the reduction of the RRR.[7,21]

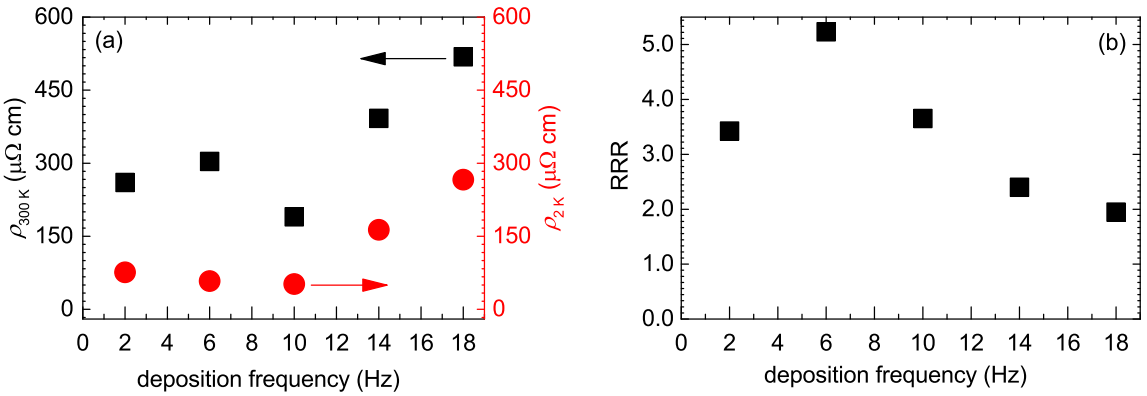

Figure 5.8: (a) The absolute values for ρ_{300K} and ρ_{2K} taken as measures of the shift in resistivity observed in Fig. 5.7 With increasing f an increase in both properties is observed (b) the residual resistivity ratio (RRR) $\rho_{300\,K}/\rho_{2\,K}$ can be taken as one indicator of the defect density in the films.

Taking a closer look at the $\rho(T)$ curves reveals that three distinct features can be reliably characterized (see Fig. (5.9) (a)):

1. The position of the distinct kink approximately in the middle ($T \approx 140K$) of the investigated temperature range that corresponds to the ferromagnetic transition temperature T_C.[23]

2. The slope γ of the clearly linear dependence of ρ on temperature observed for $T > T_C$

3. Below $T < 10K$ a resistivity minimum at $T = T_{min}$ occurs and an upturn in resistivity towards $\rho_{2\,K}$ is observed

The Curie temperature T_C of the different films is extracted from the position of the discontinuity in $\partial\rho/\partial T$. As shown in Fig. 5.9 (b), the ferromagnetic transition shifts down to lower temperatures as f increases. To characterize the linear dependence $\rho(T)$ for $T > T_C$ we followed a procedure resulting from the Bloch-Grüneisen framework and outlined in Ref.[24] and fitted the curves according to

$$\rho(T) = \rho_0 + \rho_m + \gamma T, \tag{5.2}$$

[3]The conductivity data presented were obtained by Dr. Felix Gunkel (PGI-7, Forschungszentrum Jülich, Jülich, Germany)

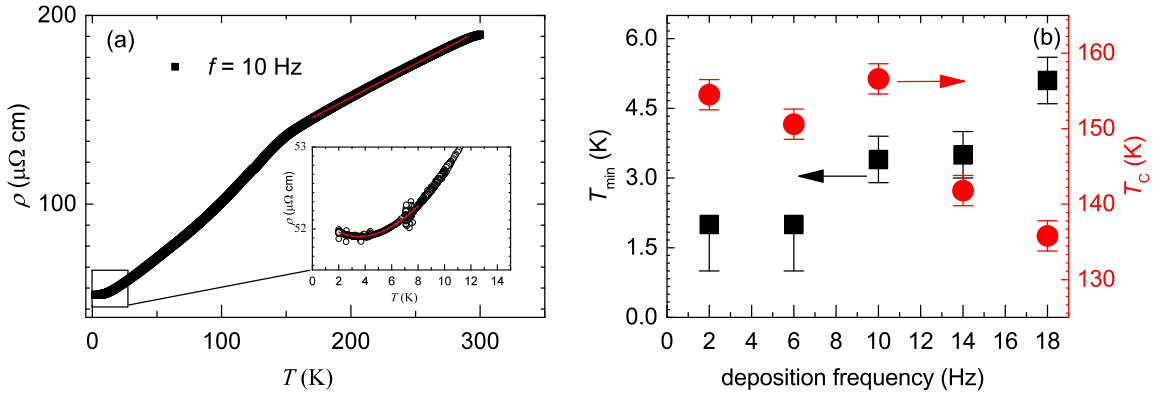

Figure 5.9: (a) More detailed example of $\rho(T)$ with a zoom-in at low temperatures shown in the inset to illustrate the resistivity minimum at the temperature T_{min}. The kink in the middle of the curve is an indicator of the Curie temperature T_{C}. (b) The values for T_{min} as well as for T_{C} exhibit a linear dependence of f.

with being ρ_0 as the residual resistivity and ρ_m as the magnetic resistivity arising from spin-scattering of electrons and assumed to be constant above T_C. Here γ is defined as

$$\gamma = \frac{2\pi k_{\mathrm{B}}}{\hbar e^2 (n/m_{\mathrm{eff}})} G(\Theta_{\mathrm{D}}/T)\lambda' \tag{5.3}$$

with $\hbar$ being the reduced Planck's constant; n the charge carrier density; m_{eff} the effective mass; $G(\Theta_{\mathrm{D}}/T)$ the Grüneisen function and λ' the electron-phonon coupling constant. The extracted slope γ -shown in Fig. (5.10)- increases as a function of f.

The resistivity behaviour at temperatures below $T < 20\,\mathrm{K}$ reveals further differences of the prepared $SrRuO_3$ thin films. We characterized the position of the resistivity minimum T_{min} as well as the the resistivity at $2\,\mathrm{K}$ $\rho_{2\,\mathrm{K}}$, depicted in Fig. 5.9 (b). The curvature in the low-temperature regime is characterized as follows: We assumed — as in several comparable studies [25,26] — that Matthiessen's rule holds and we can fit the measured resistivity curves with Eq. (5.4) assuming two independent scattering mechanisms.

$$\rho(T) = \frac{1}{\sigma_0 + uT^{1/2}} + vT^2 \tag{5.4}$$

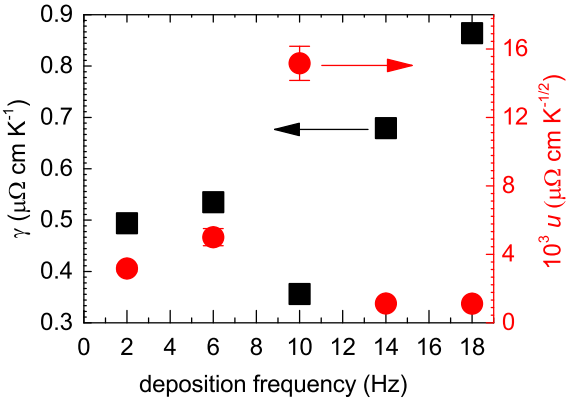

Figure 5.10: Two properties taken to characterise the high- as well as the low-temperature behaviour of the resistivity. γ defined in Eq. 5.2 was taken to quantify differences in the high-temperature regime. u defined in Eq. 5.4 indicates changes in the low temperature regime.

Here σ_0 is the minimum conductance; u accounts for $e^- - e^-$ interactions (Altshuler-Aronov correction [27]). The term vT^2 describes higher order scattering and extends the analyis to higher temperatures. Neither u nor v

reveals a clear dependence on the deposition parameters. The absolute values of v do not exhibit any dependence with$f$. Despite this lack of systematic dependence, the values as such agreed within the order of magnitude $v \approx 10^{-2}\mu\Omega cmK^{-2}$ well with what has been reported in Refs.[26,28]. In this context it is emphasized that values of u and v are prone to depend on the temperature range chosen to fit Eq. (5.4). For this reason we varied the fitting range by 20 K and the errors given are extracted from differences originating from different temperature ranges resulting in equally good fits and do not correspond to the much lower fitting-errors. The tendencies shown here do, however, not change upon variation of the fitting range.

5.3 Discussion

Many property variations in differently prepared $SrRuO_3$ thin films are commonly attributed to changes in disorder, a term often used to describe different phenomena. In some cases clear trends with microstructural film quality are observed [29]; in others, point-defects created by irradiation [4,24] are considered to be the main source of disorder. In addition it is widely believed that ruthenium vacancies (V''''_{Ru}) are the majority point defect and thus influence a wide range of properties in $SrRuO_3$ thin films [7]. In the following we will discuss the observed results, focusing on the effects of the changes in the ruthenium vacancy concentration [V''''_{Ru}].

5.3.1 Structure and Stoichiometry

With an increase in deposition frequency f a decrease in the thin-film's ruthenium content is observed (see Fig. (5.2)). Parameters known to result in systematic variations of the cation off-stoichiometry, such as laser fluence [30,31], deposition pressure [4,29] and heater temperatature, [3] can be discarded as origin of this decrease, as they remained constant. Moreover the thermodynamic instability of RuO_x [8] species alone cannot result in the observed behaviour, since a faster deposition should kinetically suppress ruthenium loss and result in observation of the opposite tendencies.

For these reasons it is concluded that differences in the film's nucleation and growth process on the substrate are the decisive factor leading to the differences in stoichiometry. This can only be the case if not entire "building-blocks" of $SrRuO_3$, but the individual components SrO and RuO_2 diffuse independently on the substrate surface. This view is supported by molecular dynamic studies [32] confirming that different surface species have different surface mobilities.

In our case at low frequencies pure step-flow growth is dominant. This implies that lifetime of adatoms is longer than the time between two pulses and adatoms barely interact with each other on the terraces. Consequently the film is formed only at the step-edges, resulting in propagation of the step-edges with ongoing deposition. Due to the fact that adatoms barely interact with each other, the probability of volatile RuO_y forming is low. This leads to films with a smoothly edged step-structure and ideal stoichiometry (see Fig. 5.1 and Fig. 5.2).

When increasing the frequency the amount of deposit reaching the the substrate in a certain time interval is increased, so is probability of island nucleation.[11] These islands are engulfed by the increasingly faster advancing steps, which results in more facetted step-edges (Fig. 5.1); a similar phenomenon was observed upon variation of the substrate's vicinal angle by Rijnders.[33] The differences in stoichiometry observed here have to stem from this increased random interaction of RuO_2 and SrO adatom species. As the probability of adatom interaction increases with frequency, the probability of volatile RuO_y species forming is enhanced. The most likely reaction leading to Ru loss is the disproportionation of RuO_2[34]:

$$2RuO_2(s) \longrightarrow Ru(s) + RuO_4(g) \tag{5.5}$$

The emergent elemental Ru will be immediately reoxidised, as oxygen is provided in superfluous amounts by the oxygen background gas. Both contrasting deposition mechanism are illustrated in a simplifying schematic fashion in Fig. 5.11.

The observation of two deposition mechanisms does not necessarily mean that the vicinal step-structure is no longer preserved. As the AFM micrographs in Fig. 5.1 show, at first glance films still grow in mode that could pass as "step-flow", even though not in its "pure" sense.[33] Furthermore the results indicate that there is no abrupt change in film growth characteristics. It is rather a smooth transition between "pure" step-flow and "pure" island growth that is accompanied by a similarly smooth enhancement of the Ru off-stoichiometry. Further support for the stated hypothesis of adatom kinetics on the substrate being the relevant parameter governing the film's stoichiometry can be obtained from literature. $SrRuO_3$ films on $SrTiO_3$ have been grown with excellent stoichiometric properties at hight temperatures up to $T = 1273\,K$ at typical oxygen partial pressures of around $pO_2 \approx 0.1\,mbar$.[3,6] At these conditions RuO_4 as well as RuO_3 should already evaporate.[8] RuO_2 on the other hand is stable under these conditions.[35] For this reason it seems justified to assume that if RuO_4/RuO_3 and not RuO_2 were the species involved in $SrRuO_3$ growth, the films should exhibit a far higher Ru deficiency. All in all the common wisdom that lowering the deposition temperatures results in diminished Ru loss thus seems of questionable help when trying to avoid a Ru deficiency. In fact, it has the opposite effect. This is because RuO_2 remains longer on the terraces so that the probability of adatom interaction (and thus the reaction Eq. (5.5) to happen) is increased.

5.3.2 Anionic defects

As stated in Chapter 4, the abundantly present Ru vacancies V''''_{Ru} are compensated by the majority electronic charge carriers — electron holes $h^{\bullet}$[36,37]— to preserve charge neutrality of the film:

$$4 \cdot [V''''_{Ru}] \approx [h^{\bullet}] \tag{5.6}$$

This means that oxygen vacancies $V^{\bullet\bullet}_{O}$ are minority defects whose concentration is stipulated by the Schottky equilibrium (Eq. 5.7). This condition determines the minority charge

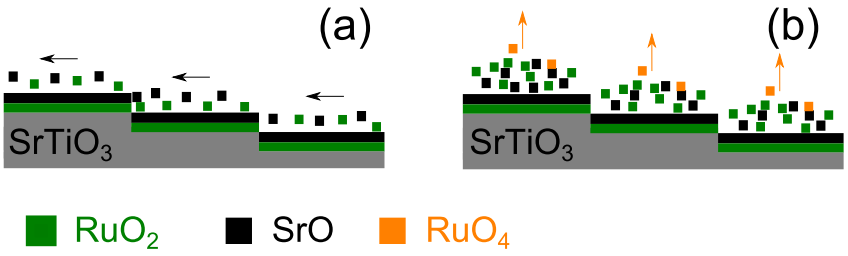

Figure 5.11: Different characteristics of the step-flow deposition mechanism for $SrRuO_3$: (a) "pure" step-flow growth dominating at low deposition frequencies f. Adatoms barely interact with each other and formation of volatile RuO_x is suppressed. (b) With increasing deposition frequency f adatom-interaction is enhanced, which results in formation of volatile RuO_x (in all probability RuO_4). As a consequence, deposition at low frequencies results in films with less Ru-defciency than films deposited at high frequencies. Morphological and crystallographic consequences are depicted in Fig. 5.1 and discussed in the text.

carrier concentration even in the cases $[V''''_{Ru}]$ and $[V''_{Sr}]$ are far away from equilibrium in a thermodynamical sense.

$$\mathrm{Sr}^{\times}_{\mathrm{Sr}} + \mathrm{Ru}^{\times}_{\mathrm{Ru}} + 3\mathrm{O}^{\times}_{\mathrm{O}} \rightleftharpoons \mathrm{V}''_{\mathrm{Sr}} + \mathrm{V}''''_{\mathrm{Ru}} + 3\mathrm{V}^{\bullet\bullet}_{\mathrm{O}} + \mathrm{SrRuO_3(s)}$$
$$\text{with} \qquad (5.7)$$
$$K_{\mathrm{Sch}}(T) = [\mathrm{V}''_{\mathrm{Sr}}][\mathrm{V}''''_{\mathrm{Ru}}][\mathrm{V}^{\bullet\bullet}_{\mathrm{O}}]^3.$$

Here $K_{\mathrm{Sch}}(T)$ is the temperature dependent equilibrium constant of the Schottky-equilibrium. Decreasing the Ru vacancy concentration results according to Eq. (5.7) in an increase in the number of oxygen vacancies.

In order to probe the behaviour of oxygen vacancies, we measured the tracer diffusion coefficient D^*_{O}, which can be expressed as

$$D^*_{\mathrm{O}} = f^* D_{\mathrm{V}} [\mathrm{V}^{\bullet\bullet}_{\mathrm{O}}] \qquad (5.8)$$

where D_{V} is the vacancy diffusion coefficient; f^*, the tracer correlation factor, a constant in the order of unity; $[\mathrm{V}^{\bullet\bullet}_{\mathrm{O}}]$ the vacancy site fraction.

Here D^*_{O} is observed to increase with increasing deposition frequency f. According to Eq. (5.7) this increase cannot be a consequence of a change in $[\mathrm{V}^{\bullet\bullet}_{\mathrm{O}}]$, as the site fraction of oxygen vacancies is expected to decrease according to Eq. (5.7). This means that the overall behaviour cannot be determined by differences in site fraction of point-defects between the samples.

A potential reason for this unexpected behaviour could originate from the observed lattice expansion in out-of-plane direction (cf. Fig. 5.3), since ionic mobility is generally inclined to be affected by strain.[38–41] One would expect this change in ionic mobility to be reflected in the activation enthalpy of oxygen tracer diffusion ΔH_{D^*} as well.[42,43] For the different strain-states of $SrRuO_3$ there is, however, no tendency in $\Delta H_{D^*_{\mathrm{O}}}$ discernible. This observation can be due to two reasons: First, it is possible that the error, the experimentally determined values are afflicted with, is so too large such that a potential tendency cannot be resolved. This

hypothesis is supported by empirical pair potential simulations, which suggest that ΔH_{mig} is increased only in the order of 0.2 eV by an increase in strain of $\epsilon \approx 0.02$.[44] Thus changes induced by this increase could not have been resolved, as the error bars are much larger than 0.2 eV. Second, we know from Sec. 2.5 that $\Delta H_{D^*_{\mathrm{O}}}$ is made up of two contributions, the activation enthalpy of generation ΔH_{gen} and the enthalpy of migration ΔH_{mig} of an oxygen vacancy.

It is highly unlikely that the individual parts ΔH_{gen} and ΔH_{mig} are both unaffected by structural and stoichiometric changes. Therefor it is conceivable that the individual contributions oppose each other. Hence further investigations devoted to unfolding the influence of strain and stoichiometry on ΔH_{gen} as well as on ΔH_{mig} will be an important issue of future endeavour.

The neccessity to investigate ΔH_{gen} originates from the fact that in perovskite oxides, e.g. in (La,Sr)(Mn,Co)O_3, ΔH_{gen} is known to be affected by the cation off-stoichiometry.[45,46] Our result, however, suggest no dependence on the Ru-stoichiometry at all if one assumes ΔH_{mig} to remain unaffected. In this context it would be of particular interest to measure ΔH_{gen} as a function of cation off-stoichiometry with concomittant characterization of the bad-metallic properties of $SrRuO_3$. This will help to elucidate whether the charge disproportionation reaction discussed in Sec. (4.1.2) is the decisive parameter in determining ΔH_{gen} or whether the model described in Refs. [45,46] is valid.

Lastly in this section, the oxygen surface exchange reaction will be addressed. The data presented in Fig. 5.4 show an increase in k^*_{O} with increasing deposition frequency. In Sec. 4.2 it was pointed out that the empirical derived rule[47] of high electronic charge carrier concentrations and a low concentrations of oxygen vacancies result in a high surface exchange coefficient k^*_{O} seems to be invalid in the case of $SrRuO_3$. This is certainly because these empirical relations were derived for semiconductors and not for metals.

In our case, the clear increase in k^*_{O} with ρ suggest that with decreasing concentration of electronic charge carriers, indicated by and increase in ρ, the surface exchange reaction is inhibited. From above's discussion we know, that D^*_{O} can hardly be regarded as a reliable indicator for the concentration of oxygen vacancies, as it is it influence by strain. It could as well be that the increased strain ϵ — as observed in Ref. [48]— dominates the behaviour. A further peculiarity is that with increasing deposition frequency (and thus k^*_{O}) the fraction of SrO present in the sample increased as well (Fig. 5.2). Commonly one would expect SrO to hamper the oxygen incorporation into the sample.[49] To resolve these obscurities further studies dedicated solely to the electronic- and defect-properties of the sample surface are needed. One point however can be made: It seems that the mechanism responsible for oxygen incorporation is the same for all samples as the corresponding activation enthalpy stays constant. It is more likely to be the unique combinations of electronic charge carriers and point-defects that results in the changes of k^*_{O}.

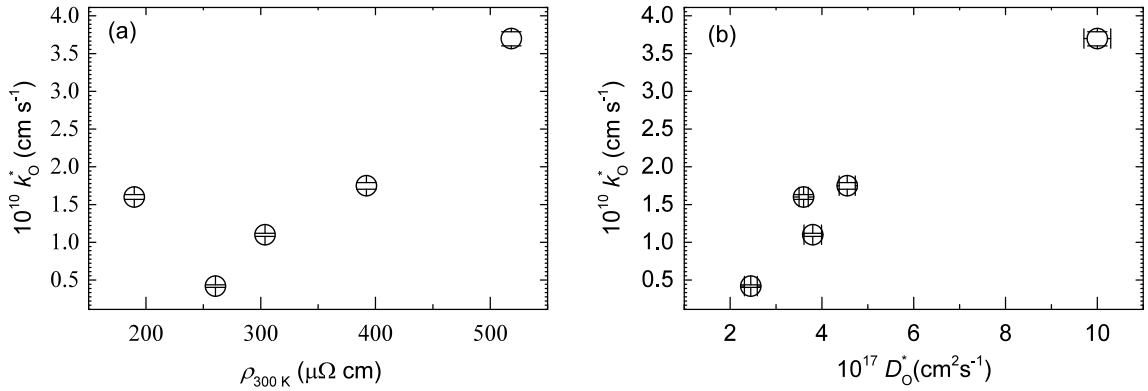

Figure 5.12: A more detailed consideration of the surface exchange coefficient k_O^*(a)dependent on the film's resistivity (b) on the tracer diffusion coefficient D_O^*. In both cases a clear trend is discernible. The diffusion data correspond to $T = 1023\,\mathrm{K}$ and $pO_2 = 500\,\mathrm{mbar}$.

5.3.3 Electrical properties and disorder

The analysis of the conductivity measurements yielded that all resistivity curves exhibit a similar behaviour, the main difference being a shift characterized by ρ_{300K} and ρ_{2K} in the resistivity's magnitude (see Fig. 5.8(c)). From the above discussion we know that with increasing frequency an increase in $[V_{Ru}^{''''}]$ is observed and a decrease $[V_O^{\bullet\bullet}]$ is expected. Both effects have been reported to decrease the density of states at the Fermi level [7,29] and as a consequence could result in a decrease of the overall conductivity. A further explanation going in the same direction is that with increasing Ru vacancy concentration the conduction pathways within the RuO_6 octahedra of $SrRuO_3$'s perovskite structure are broken which results in an increased resistivity. [50,51] Taking a closer look at our data we observed — as numerous previous authors [5,7,14,26,52–54] — a decrease in Curie temperature T_C going hand in hand with an increase in lattice strain and $[V_{Ru}^{''''}]$. This widespread consensus regarding experimental obervations is however not reflected in unambiguity in interpretation. One common explanation is that by changing the lattice parameter a change in the Ru-O-Ru bond angle is induced, thus drastically influencing the coupling of Ru : t_{2g} and O : 2p orbitals. These two orbitals decisively determine the ferromagnetic properties [52,54] and for this reason a modification of their coupling is expected to result in a reduced T_C. Several authors, however, cast coubt on the pure itinerant character of $SrRuO_3$ and the validity of band-structure arguments in explaining the magnetic behaviour. [14,29,50,55,56] For this reasons enhanced local disorder induced by Ru vacancies seems the more likely reason for the decrease in T_C with increasing f. This assumption is consistent with the characterization of disorder at low temperatures as well as with several experimental and theoretical indications [14,29].

Attributing the clear increase in slope γ of the linear high-temperature conductivity behaviour to an increase in disorder introduced by Ru vacancies is tempting and consistent with interpretations given in Ref. [24]. Exactly the opposite trend is however expected from theory. [57] As different parts of the Fermi-surface govern the electrical behaviour at high and at low tem-

peratures respectively[37], one could speculate that also different point-defects influence this behaviour. In our case a decrease in oxygen vacancies with increasing f (cf. Eq. (5.7)) would mean a decrease in disorder of the anion sublattice for $T \geq T_C$ and thus less suppression of the temperature dependent increase in $\rho(T)$. As the concentration of oxygen vacancies is very low, it seems, however, unreasonable to attribute the high-temperature conductivity behaviour to this phenomenon.
The low temperature behaviour is far more straight forward to rationalise : The clear increase in minimum resistivity $T_{\min}$ with f and is thus a consequence of an increase in $[V''''_{Ru}]$. These vacancies act as scattering centers for electrons. In that manner electron localization by impurity scattering is enhanced, a phenomenon we could successfully describe within the Altshuler-Aronov framework[27] and which is comparable to similar studies on $SrRuO_3$[25,26] as well as on manganites[58]. (Refs.[25,26] excluded a magnetic origin- the Kondo-effect- as origin of this behaviour.) Despite the successful description of our data with Eq. (5.4), the large scatter in the fitting parameter u with deposition condicitons remains a peculiarity. This scatter is particularly surprising as u depends on the mean-free charge carrier path[27] and thus should as $T_{\min}$ significantly be influence by $[V''''_{Ru}]$.

5.4 Conclusions

In this chapter it was shown, that varying the deposition frequency in the PLD deposition process is sufficient to systematically vary the Ru off-stoichiometry in $SrRuO_3$ thin-films. As origin of these variations different growth kinetics induced by the deposition frequency were identified. Primarily an increase in adatom interaction resulting in the increased formation of volatile Ru species — presumable mainly by the disproportionation of RuO_2 to RuO_4— can be hold responsible for this phenomenon.
By changing the films Ru stoichiometry several other physical properties are altered. These are the out-of-plane lattice constant and thus the strain state of the film, the oxygen tracer diffusion and surface exchange coefficients, the Curie temperature and temperature of minimal resistivity, as well as parameters characterising disorder in the films. These changes have hitherto been widely discussed in terms of disorder phenomena. In this contribution we could attribute some of these phenomena —such as T_C and $T_{\min}$— being a cause of a variation in Ru vacancy concentration. Other observables are not systematically dependent on changes in the cation sublattice. This is particularly striking in the case of the activation enthalpy of oxygen tracer diffusion as a mutual dependence of both defects is expected. Further endeavour particularly focusing on oxygen vacancy diffusivity is required to better understand these phenomena. Connecting these investigation of point-defect chemistry with that of disorder induced property changes seems to be promising, but so far underrated, way to further understand fascinating properties of $SrRuO_3$ thin-films.

Bibliography

[1] X. Fang and T. Kobayashi, *J. Appl. Phys.*, 2001, **90**, 162–166.
[2] M. Hiratani, C. Okazaki, K. Imagawa and K. Takagi, *Jpn. J. Appl. Phys.*, 1996, **35**, 6212.
[3] N. Zakharov, K. Satyalakshmi, G. Koren and D. Hesse, *J. Mater. Res.*, 1999, **14**, 4385–4394.
[4] J.-P. Maria, S. Trolier-McKinstry, D. G. Schlom, M. E. Hawley and G. W. Brown, *J. Appl. Phys.*, 1998, **83**, 4373–4379.
[5] Y. Z. Yoo, O. Chmaissem, S. Kolesnik, B. Dabrowski, M. Maxwell, C. W. Kimball, L. McAnelly, M. Haji-Sheikh and A. P. Genis, *J. Appl. Phys.*, 2005, **97**, –.
[6] T. Ohnishi and K. Takada, *Appl. Phys. Express*, 2011, **4**, 025501.
[7] W. Siemons, G. Koster, A. Vailionis, H. Yamamoto, D. H. A. Blank and M. R. Beasley, *Phys. Rev. B*, 2007, **76**, 075126.
[8] W. E. Bell and M. Tagami, *J. Phys. Chem.*, 1963, **67**, 2432–2436.
[9] D. B. Chrisey and G. K. Hubler, *Pulsed laser deposition of thin films*, Wiley New York, 1994.
[10] R. Eason, *Pulsed laser deposition of thin films: applications-led growth of functional materials*, John Wiley & Sons, 2007.
[11] W. Hong, H. N. Lee, M. Yoon, H. M. Christen, D. H. Lowndes, Z. Suo and Z. Zhang, *Phys. Rev. Lett.*, 2005, **95**, 095501.
[12] J. J. Randall and R. Ward, *J. Am. Chem. Soc.*, 1959, **81**, 2629–2631.
[13] C. Eom, R. Cava, R. Fleming, J. M. Phillips, J. Marshall, J. Hsu, J. Krajewski and W. Peck, *Science*, 1992, **258**, 1766–1769.
[14] B. Dabrowski, O. Chmaissem, P. W. Klamut, S. Kolesnik, M. Maxwell, J. Mais, Y. Ito, B. D. Armstrong, J. D. Jorgensen and S. Short, *Phys. Rev. B*, 2004, **70**, 014423.
[15] J. Schwarzkopf, R. Dirsyte, A. Devi, M. Schmidbauer, G. Wagner and R. Fornari, *Thin Solid Films*, 2010, **518**, 4675 – 4679.
[16] R. Meyer, R. Waser, J. Helmbold and G. Borchardt, *J. Electroceram.*, 2002, **9**, 101–110.
[17] S. N. Ruddlesden and P. Popper, *Acta Crystallogr.*, 1957, **10**, 538–539.
[18] S. N. Ruddlesden and P. Popper, *Acta Crystallogr.*, 1958, **11**, 54–55.
[19] C. Kittel, *Einführung in die Festkörperphysik*, Oldenbourg Verlag, 2013.
[20] L. Klein, J. S. Dodge, C. H. Ahn, J. W. Reiner, L. Mieville, T. H. Geballe, M. R. Beasley and A. Kapitulnik, *J. Phys.: Condens. Matter*, 1996, **8**, 10111.
[21] C. L. Chen, Y. Cao, Z. J. Huang, Q. D. Jiang, Z. Zhang, Y. Y. Sun, W. N. Kang, L. M. Dezaneti, W. K. Chu and C. W. Chu, *Appl. Phys. Lett.*, 1997, **71**, 1047–1049.
[22] X. D. Wu, S. R. Foltyn, R. C. Dye, Y. Coulter and R. E. Muenchausen, *Appl. Phys. Lett.*, 1993, **62**, 2434–2436.
[23] T. Moriya, *J. Magn. Magn. Mater.*, 1979, **14**, 1 – 46.
[24] G. Herranz, V. Laukhin, F. Sánchez, P. Levy, C. Ferrater, M. V. García-Cuenca, M. Varela and J. Fontcuberta, *Phys. Rev. B*, 2008, **77**, 165114.
[25] G. Herranz, B. Martínez, J. Fontcuberta, F. Sánchez, C. Ferrater, M. V. García-Cuenca and M. Varela, *Phys. Rev. B*, 2003, **67**, 174423.
[26] M. A. López de la Torre, Z. Sefrioui, D. Arias, M. Varela, J. E. Villegas, C. Ballesteros, C. León and J. Santamaría, *Phys. Rev. B*, 2001, **63**, 052403.
[27] B. Altshuler and A. Aronov, *Solid State Commun.*, 1979, **30**, 115 – 117.
[28] L. Klein, J. Dodge, C. Ahn, G. Snyder, T. Geballe, M. Beasley and A. Kapitulnik, *Physical review letters*, 1996, **77**, 2774.
[29] W. Lu, K. He, W. Song, C.-J. Sun, G. Moog Chow and J.-s. Chen, *J. Appl. Phys.*, 2013, **113**, –.
[30] T. Ohnishi, M. Lippmaa, T. Yamamoto, S. Meguro and H. Koinuma, *Appl. Phys. Lett.*, 2005, **87**, 241919.
[31] S. Wicklein, A. Sambri, S. Amoruso, X. Wang, R. Bruzzese, A. Koehl and R. Dittmann, *Appl. Phys. Lett.*, 2012, **101**, –.
[32] J. L. Wohlwend, R. K. Behera, I. Jang, S. R. Phillpot and S. B. Sinnott, *Surf. Sci.*, 2009, **603**, 873 – 880.
[33] A. J. H. M. Rijnders, *Ph.D. thesis*, University of Twente, Enschede, 2001.
[34] M. Green, M. Gross, L. Papa, K. Schnoes and D. Brasen, *J. Electrochem. Soc.*, 1985, **132**, 2677–2685.
[35] S. Ikeda, U. Azuma, N. Shirakawa, Y. Nishihara and Y. Maeno, *J. Cryst. Growth*, 2002, **237**, 787–791.
[36] T. Maekawa, K. Kurosaki, H. Muta, M. Uno and S. Yamanaka, *J. Alloys Compd.*, 2005, **387**, 56–59.
[37] S. C. Gausepohl, M. Lee, R. A. Rao and C. B. Eom, *Phys. Rev. B*, 1996, **54**, 8996–8999.
[38] N. Schichtel, C. Korte, D. Hesse and J. Janek, *Phys. Chem. Chem. Phys.*, 2009, **11**, 3043–3048.
[39] J. L. Rupp, *Solid State Ionics*, 2012, **207**, 1 – 13.
[40] M. Rushton, A. Chroneos, S. Skinner, J. Kilner and R. Grimes, *Solid State Ionics*, 2013, **230**, 37 – 42.
[41] J. Hinterberg, T. Zacherle and R. A. De Souza, *Phys. Rev. Lett.*, 2013, **110**, 205901.
[42] S. Skinner and J. Kilner, *Solid State Ionics*, 2000, **135**, 709 – 712.
[43] M. Burriel, G. Garcia, J. Santiso, J. Kilner, R. Chater and S. Skinner, *J. Mater. Chem.*, 2007, **18**,

416–422.
[44] L. Hesselmann, *Bachelor Thesis*, RWTH-Aachen University, 2013.
[45] M. H. Lankhorst, H. Bouwmeester and H. Verweij, *J. Solid State Chem.*, 1997, **133**, 555 – 567.
[46] R. A. De Souza and J. A. Kilner, *Solid State Ionics*, 1998, **106**, 175–187.
[47] R. A. De Souza, *Phys. Chem. Chem. Phys.*, 2006, **8**, 890–897.
[48] M. Kubicek, Z. Cai, W. Ma, B. Yildiz, H. Hutter and J. Fleig, *ACS Nano*, 2013, **7**, 3276–3286.
[49] W. Jung and H. L. Tuller, *Energy Environ. Sci.*, 2012, **5**, 5370–5378.
[50] Z. Sefrioui, D. Arias, M. A. Navacerrada, M. Varela, G. Loos, M. Lucía, J. Santamaría, F. Sánchez-Quesada and M. A. López de la Torre, *Appl. Phys. Lett.*, 1998, **73**, 3375–3377.
[51] R. A. Rao, Q. Gan, C. B. Eom, R. J. Cava, Y. Suzuki, J. J. Krajewski, S. C. Gausepohl and M. Lee, *Appl. Phys. Lett.*, 1997, **70**, 3035–3037.
[52] R. Dirsyte, J. Schwarzkopf, M. Schmidbauer, G. Wagner, K. Irmscher, S. B. Anooz and R. Fornari, *Thin Solid Films*, 2011, **519**, 6264 – 6268.
[53] D. Kan, R. Aso, H. Kurata and Y. Shimakawa, *J. Appl. Phys.*, 2013, **113**, –.
[54] Q. Gan, R. Rao, C. Eom, J. Garrett and M. Lee, *Appl. Phys. Lett.*, 1998, **72**, 978–980.
[55] M. De Marco, D. Coffey, R. Heary, B. Dabrowski, P. Klamut, M. Maxwell, S. Toorongian and M. Haka, *Phys. Rev. B*, 2005, **71**, 104403.
[56] J. H. Cho, Q. X. Jia, X. D. Wu, S. R. Foltyn and M. P. Maley, *Phys. Rev. B*, 1996, **54**, 37–40.
[57] S. Kumar and P. Majumdar, *Phys. Rev. Lett.*, 2005, **94**, 136601.
[58] E. Rozenberg, M. Auslender, I. Felner and G. Gorodetsky, *J. Appl. Phys.*, 2000, **88**, 2578–2582.

Chapter 6

On the analysis of diffusion profiles with two or three features

Oxygen isotope exchange experiments, when combined with determination of the isotope profile in the solid by means of Secondary Ion Mass Spectrometry (SIMS), are a widely used and powerful tool to determine the rate of oxygen transport in an oxide.[1–5] This transport process may be governed in a single crystal by either diffusion of oxygen in the bulk lattice, mediated by vacancy or interstitial defects, or by the kinetics of the surface reaction between gaseous oxygen and oxygen ions in the solid. In essence, one is interested in the answer to the question of how fast oxygen moves.

A second question that can be addressed by isotope exchange studies is where oxygen moves. That is, short-circuit diffusion of oxygen along extended defects, such as grain boundaries or dislocations, may be revealed under certain experimental conditions in an diffusion profile.[6,7] To be specific, a second feature is observed in diffusion profiles at large penetration depths.

Diffusion profiles with two or more features can also be the consequence of a non-uniform distribution of defects in oxides. This non-uniformity can be a consequence of oxygen-vacancy depletion in an equilibrium space-charge layer at an oxide surface[3,8–11] or an inhomogeneous defect distribution in the near surface area resulting from sluggish cation or impurity diffusion.[12,13] Further effects such as strain can also significantly alter the shape of a measured tracer diffusion profile.[14] A non-uniform defect distribution may also be found in metastable thin films systems (see Chapter 4 for details).

In all these cases the main questions are: How are point defects distributed and is point defect migration uniform or do fast-diffusion pathways exist?

One problem is that in two different cases one may obtain profiles with the same form — a short, sharp profile close to the surface, followed by a longer more extended profile. Having measured such a profile, one could attribute the first feature to bulk diffusion and the second to fast diffusion along an extended defect; or alternatively one could attribute the first feature to slow diffusion in a vacancy-depleted space-charge zone and the second to diffusion in a uniform bulk phase. Both explanations have been suggested for single crystal $SrTiO_3$.[3,15]

The salient question arising here is: Is there a simple way to test the validity of each description in an unbiased, quantitative fashion?

In this context "unbiased" implies not to employ any qualitative arguments that might favor one or the other model. Such arguments could be the observation of grain-boundaries or dislocations in the samples investigated [15] or implications derived from thermodynamic considerations. [3,16]
Here the focus is on illustrating how a diffusion model can be validated or falsified by checking for inconsistencies in the model itself. First the mature model often used to describe diffusion along grain boundaries (GB-MODEL) is contrasted with a rather recent model taking diffusion through a surface space-charge layer into account (SCL-MODEL).
To do this, the a two step approach is pursued:

1. The competing models are implemented in finite element calculations and tracer diffusion profiles are simulated.

2. The simulated tracer diffusion profiles are treated as if they were experimental data. Thus the profiles obtained from the GB MODEL are analysed in terms of the SCL MODEL; and vice versa. A careful analysis of these data provides quantitative arguments that can be used to rule out the models yielding in an invalid description of the diffusion behaviour.

The second part of this chapter is devoted to profiles with three features. In the last section the application of the introduced theoretical considerations to experimental data will be presented.

6.1 GB-model versus SCL-model

The purpose of this section is to illustrate the importance of obtaining and analysing diffusion profiles as a function of time in order to establish a valid model for the diffusion behaviour. In the first section similarities between simulated profiles resulting from the SCL and the GB models will be emphasised. Subsequently SCL model data will be treated according to the procedure conventionally used to analyse grain-boundary diffusion. Here two quantitative conditions will be derived, which are indispensable for the GB model to be valid. In the last part of this section it will be shown that these two conditions cannot only be applied to validate the diffusion model itself, but are also useful in checking for inconsistencies within the data processing routine.

6.1.1 Profile simulation

Interpretation of experimental, two-fold diffusion profiles resulting from coupled bulk and grain-boundary diffusion follows widely accepted models. [17–20] These models, originally developed for metals, [17] have been successfully applied to oxides as well [21] and a general tendency of faster diffusion along extended defects is observed. It is believed that faster diffusion is a result from the atomic arrangement of extended defects being more open than in the densely packed bulk.

As far as oxygen diffusion in oxides is concerned, there is, however, a phenomenon questioning the validity of the existing models: The potential presence of space-charge layers in oxides.[22–24] There are strong indications that these space-charge regions are also present at a sample surface.[3]

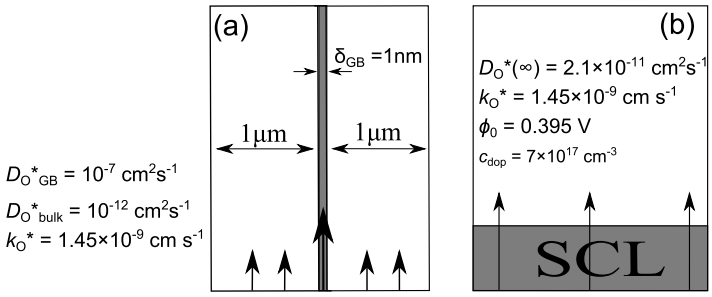

Figure 6.1: In the case of (a) GB-MODEL coupled grain-boundary and bulk diffusion. (b) SCL-MODEL Tracer diffusion through a space charge layer below the surface. The extend of the simulation cell (shown not to scale) was always larger than $4\sqrt{D_O^*(\mathrm{GB})}$

These space-charge layers strongly affect the first part of a tracer diffusion profile. To illustrate this the models depicted in Fig. 6.1 were implemented into the finite element (FEM) simulation package Comsol Multiphyics (COMSOL AB, Stockholm, Sweden) and the corresponding oxygen tracer diffusion profiles were simulated. The spatial variation of the tracer diffusion coefficient in the space charge layer was simulated according to the procedure outlined in Section (2.5.2) and Ref. [3]. The set of parameters used is given for both cases in Fig. 6.2. Here $D_O^*(\mathrm{bulk})$ and $D_O^*(\mathrm{GB})$ are the tracer diffusion coefficients in the bulk and in the grain boundary respectively. k_O^* is the surface exchange coefficient and t_{ex} the exchange time. In the SCL-MODEL $D_O^*(\infty)$ is the tracer diffusion coefficient far away from the interface, ϕ_0 the interface potential and c_{dop} the assumed doping concentration (details on the SCL-MODEL are given in Sec. 2.5.2). Resulting diffusion profiles are shown in Fig. 6.2 (a) for diffusion through a SCL and in Fig. 6.2 (b) for GB-diffusion.
Let us now assume these simulated profiles are experimental data. Then there is an apparent similarity as far as the two-fold character of the profiles is concerned. This prohibits an initial assignment to one or the other model available to describe the diffusion behaviour based on profile shape alone. Therefore the decision which of the two available models to choose is rather an intuitive than a quantitatively substantiated one. In the following section quantitative criteria enabling a substantiated discrimination between the GB- and the SCL-MODEL will be derived.

6.1.2 Pitfalls when interpreting tracer diffusion profiles

Conventionally two-fold diffusion profiles are described within the framework of GB diffusion in the Harrision type B regime[18,19,25]: The corrected isotope fraction n_r^* is plotted as a function of the depth $x^{6/5}$ (Fig. 6.2 (f)). From careful evaluation of one profile's slope the bulk as well as the GB diffusion coefficient can be obtained. This kind of analysis principally works as long as the behaviour in a n_r^* versus $x^{6/5}$ is clearly linear, which is also the case for

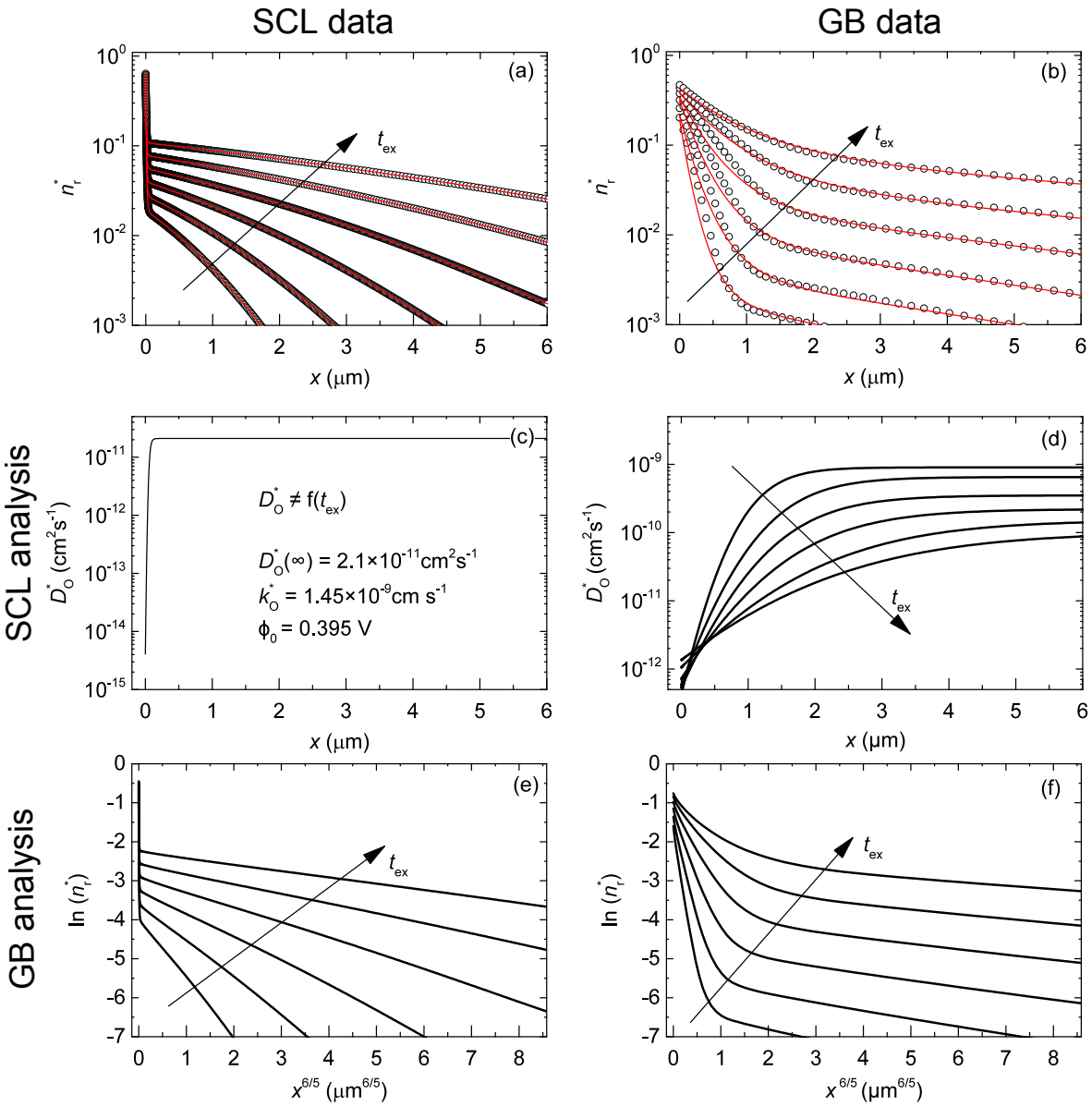

Figure 6.2: Simulated tracer diffusion profiles resulting from (a) diffusion through a surface SCL with bulk-diffusion, (b) coupled GB and bulk diffusion. In both cases the red lines are fits assuming the SCL-MODEL.
Spatial variation of the local diffusion coefficient determined (c) to describe the profiles shown in (a); and (d) to describe the profiles shown in (b). Analysis of the GB-MODEL data with the SCL-MODEL yields a behaviour that is a function of t_{ex}; this is not the case for the SCL-MODEL.
Data processing according to the framework for Harrison type B diffusion behaviour. The corrected isotope fraction is plotted versus $x^{6/5}$. For both models, this way of processing results in straight lines as a function of $x^{6/5}$, as the plots in (e) and (f) indicate.

profiles obtained by the SCL-model (Fig. 6.2 (e) and (f)). A second requirement for such an analysis to be valid is that these slopes have to follow a specific (exchange) time dependence

on

$$\frac{\partial \ln(n_r^*)}{\partial x^{6/5}} = \left(\frac{1.322}{\delta} \cdot \frac{\sqrt{D_{\mathrm{O}}^*(\mathrm{bulk})}}{D_{\mathrm{O}}^*(\mathrm{GB})} \right) t_{\mathrm{ex}}^{-0.3} \tag{6.1}$$

This relation (Eq. (6.1)) yields two salient consequences regarding a plot of $\frac{\partial \ln(n_r^*)}{\partial x^{6/5}}$ versus $t_{\mathrm{ex}}^{-0.3}$, which can be formulated as the following conditions:

C1. The overall behaviour has to be linear

C2. The line has to go through the origin

As a prerequisite, the condition **C0** say, $\ln(n_r^*)$ has to be linear in $x^{6/5}$ so that the above analysis can be conducted. Only if these two conditions are fulfilled a further analysis of diffusion tails following the procedure proposed for example in Ref. [18] is valid and meaningful. This means that a linear behaviour of $\ln(n_r^*)$ with $x^{6/5}$ is a necessary condition, but it is insufficient for the GB-MODEL to yield a valid description of the diffusion profiles. Only the fulfillment of all three conditions **CO**, **C1** and **C2** provice sufficient arguments to assume the GB-MODEL to be valid. Thus a time dependent investigation of the diffusion behaviour is indispensable.

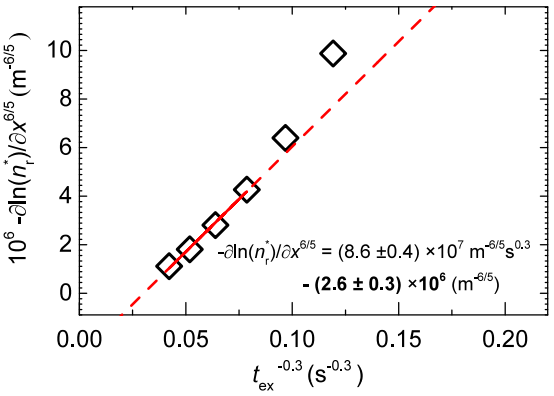

Figure 6.3: Values for the GB diffusion tail slopes extracted from Fig. (6.2) (e) are plotted as a function of $t_{ex}^{-0.3}$. There is no clear linear trend of the overall behaviour discernible. All potential lines that can be drawn through the data points do not go through the origin.

In Fig. 6.3 slopes extracted from Fig. 6.2 (e), that is profiles from the SCL-MODEL analysed in terms of fast GB diffusion, are plotted as a function of $t_{ex}^{-0.3}$. Generally the behaviour of $\ln(n_r^*)$ versus $x^{6/5}$ depicted in Fig. 6.2 (e) can be regarded as linear. Thus the prerequite condition **C0** for assuming the GB-MODEL is fulfilled. The dependence of the slope-value with $t_{\mathrm{ex}}^{-0.3}$, however, is not linear. This contradicts the condition **C1**. Assuming further that the condition for Harrison-type B diffusion only holds in a certain restricted time regime, one can draw a straight line using only some of the data points. In all conceivable cases, however, the fitted lines do not go through the origin, which means that condition **C2** is violated.

Because both neccessary conditions **C1** and **C2** are not fulfilled, we have a clear discrepancy that demonstrates the inadequacy of the GB-MODEL to describe diffusion profiles resulting from SCL-MODEL diffusion.

For the aforementioned reasons only the SCL-MODEL yields a valid description of the diffusion behaviour in cases a surface space-charge layer is present. Simulations resulting from the SCL-model are shown in Fig. 6.2 (a) as red lines. In Fig. 6.2 (c) the corresponding spatial

variation of the diffusion coefficient is shown. It should be noted that the spatial variation of the diffusion coefficient is independent of the exchange time t_{ex}. This implies that a stable distribution of defects is probed, which is the purpose of an isotope exchange experiment as it is defined in Sec. 3.3.

In a similar fashion as the SCL profiles, profiles resulting from GB with coupled bulk diffusion can be misinterpreted. As depicted in Fig. 6.2 (b), it is in principle possible to describe the obtained data with the SCL-MODEL. The spatial variation of the tracer diffusion coefficient D^*_O for each profile is depicted in Fig. 6.2) (d) and the corresponding model parameters are listed in Table 6.1. From the listed values, as well as from their visualization as D^*_O, it is clear that all model parameters depend on the exchange time t_{ex}. This is in fundamental contradiction to the assumption that an equilibrium space charge-layer is probed. The fact that the variation in model coefficients only becomes apparent when a set of diffusion profiles corresponding to different t_{ex} is analysised, again emphasises the importance of a time dependent investigation of the diffusion behaviour.

Table 6.1: Parameters used in the SCL-MODEL to describe the profiles depicted in Fig. 6.2 (b). For each diffusion time t_{ex} a different set of parameters is required for a successful description of the data.

Constant	$t_{ex} = 300\,s$	$t_{ex} = 1200\,s$	$t_{ex} = 2400\,s$	$t_{ex} = 9600\,s$
$10^{11} \times D^*_O(\infty)$ / $cm\,s^{-2}$	$(90 \pm 5) \times 10^{-11}$	(35 ± 5)	(22 ± 2)	(10 ± 1)
$10^{14} \times k^*_O$ / $cm\,s^{-1}$	(11 ± 1)	(13 ± 1)	(13 ± 1)	(15 ± 1)
ϕ_0 / mV	(355 ± 5)	(300 ± 5)	(265 ± 5)	(200 ± 5)
$10^{14} \times c_{dop}$ / cm^{-3}	(15 ± 1)	(5.0 ± 0.1)	(3.0 ± 0.1)	(1.0 ± 0.1)

6.1.3 Consistent analysis and validation of the GB-Model

In the last section the importance of a time dependent investigation of the diffusion behaviour was emphasised in the context of falsifying an assumed diffusion model. In this section it will be shown that the same kind investigation can also be used to validate the assumed GB-MODEL. Moreover the limits regarding the amount of information the classical analysis can provide will become apparent.

These limits are a consequence of the surface incorporation reaction, which causes strong deviations from the classically expected erfc or Gaussian diffusion behaviour in the first few µm of a diffusion profile (see Fig. 6.2 (b) and also Refs. [26,27]).

At large penetration depth, however, the classical dependence [28] on $x^{6/5}$ still holds. [26] This fact can be also illustrated in countourplots depicting the lateral distribution of diffusant after selected exchange times (Fig. 6.6). For the simulations resulting in Fig. 6.6 (a) – (c) a limiting surface exchange reaction was assumed; for those results depicted in Fig. 6.6 (d) – (f) the concentration of diffusant at the sample surface was assumed to be constant . One can clearly see that the total amount of tracer incorporated into the sample is much higher in Fig. 6.6 (d) – (f), the cases no surface exchange reaction is limiting the tracer incorporation. Furthermore the tracer concentration contours differ significantly in the first few µm away

from the diffusant's source. At larger penetration depths, however, the diffusion behaviour with or without surface limitation does not differ. This fact is also be demonstrated in Fig. 6.4. Here the corresponding tracer diffusion profiles for one specific t_{ex} are depicted. It is obvious that only the magnitude of tracer fraction, but not qualitative behaviour with $x^{6/5}$ changes. Extracting now values for the slope $\partial \ln(n_r^*)/\partial x^{6/5}$ from such plots as a function of t_{ex} yields Fig. 6.5 (a) and (b).

By first looking at Fig. 6.5 (a) and (b) it is striking that the absolute values as well as the trends for both cases, without k_O^* and with k_O^*, are identical. This again confirms that the qualitative diffusion behaviour, that is the interaction of grain-boundary and bulk diffusion, is not influenced by the surface incorporation reaction at large penetration depths.

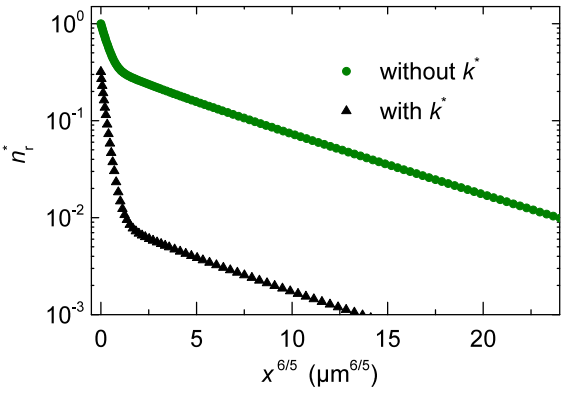

Figure 6.4: Diffusion profiles resulting from coupled bulk and grain-boundary diffusion with and without the assumption of a surface incorporation reaction limiting the amount of tracer being incorporated into the sample.

Furthermore two these plots provide two additional insights: First, there is a certain time regime, where the derived value for $\partial n_r^*/\partial x^{6/5}$ form a straight line which indeed goes through the origin. This means that the two conditions, **C1** and **C2**, are both fulfilled. Second, for values of the GB slope obtained outside of the Harrison type B regime conditions **C1** and **C2** are no longer fulfilled. This can be recognised by the fact that values for the GB slope obtained at long diffusion times, that is small values for $t_{ex}^{-0.3}$, no longer lie on the straight line going through the origin as the values obtained in the Harrison type B regime. As a delimiter of the Harrison

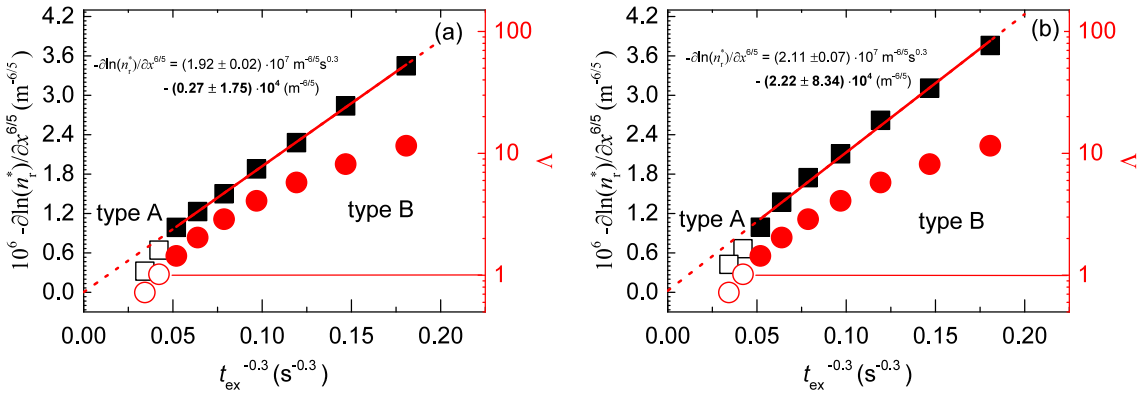

Figure 6.5: Values for $\partial \ln(n_r^*)/\partial x^{6/5}$ as a function of $t_{ex}^{-0.3}$ for (a) constant source conditions and (b) assuming an oxygen surface incorporation reaction with a rate constant $k_O^* = 1.45 \times 10^{-9}\,\mathrm{cm\,s^{-1}}$. In both cases essentially the same behaviour is observed. (see text)

type B regime the dimensionless parameter $\Lambda = \frac{Y}{\sqrt{D^*_{\mathrm{O}}(\mathrm{bulk}) \cdot t_{\mathrm{ex}}}}$ is used.[19,25] With Y being the distance between two grain-boundaries, here 2 µm (cf. Fig. 6.1). As soon as the diffusion fringes resulting from coupled GB and bulk diffusion are in the order of the distance between two grain-boundaries the diffusion fringes start overlapping. This is the case as soon as $\Lambda \approx 1$. Such a behaviour is characteristic for the Harrison type A regime.[25] Therefore the deviations from the linear behaviour with $t_{\mathrm{ex}}^{-0.3}$ and thus violations of condition **C1** and **C2** are to be expected for values of $\Lambda \leq 1$.

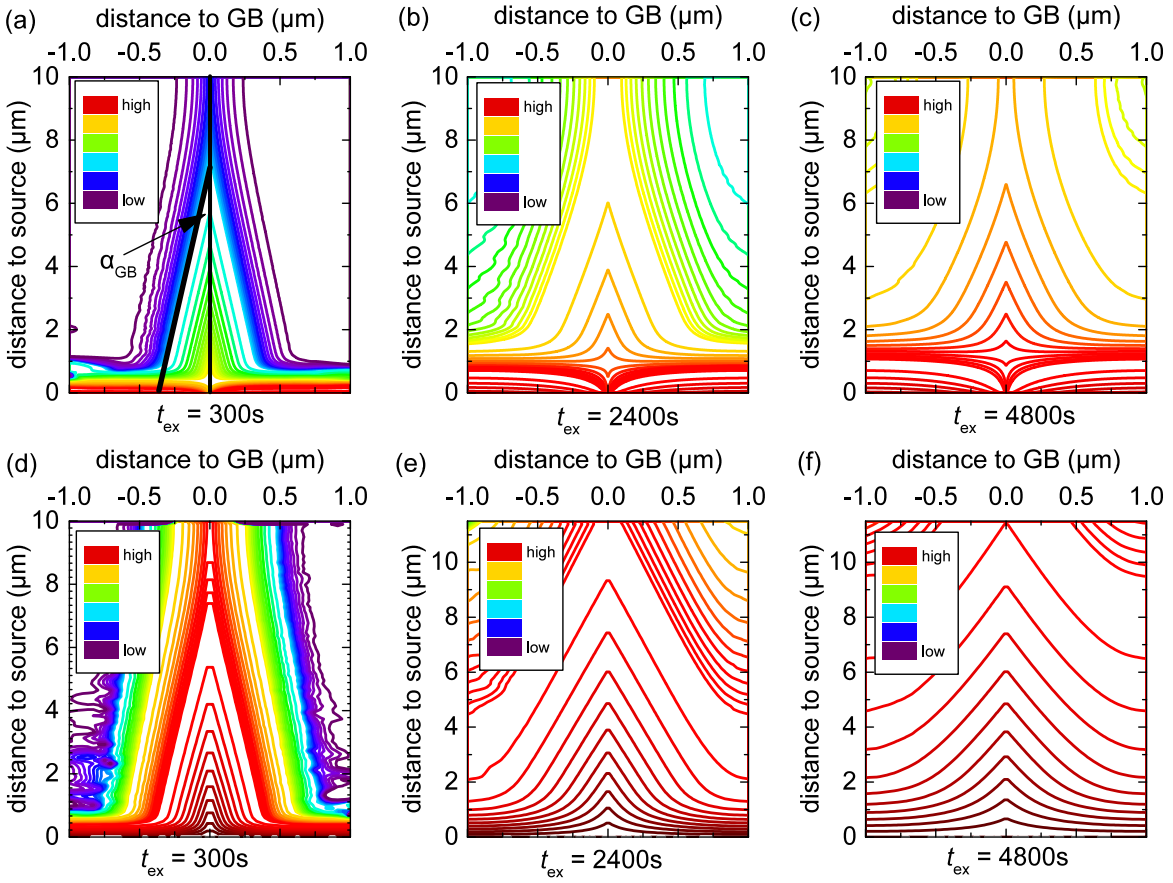

Figure 6.6: Contour plots of the 2-dimensional tracer distribution after diffusion through a grain-boundary (GB) ($D^*_{\mathrm{GB}} = 10^{-7}\,\mathrm{cm^2\,s^{-1}}$) and the adjacent bulk material ($D^*_{\mathrm{bulk}} = 10^{-12}\,\mathrm{cm^2\,s^{-1}}$). In the middle of the abscissa, the GB is situated. The diffusion source is located at the zero-line of the ordinate. In plots (a)– (c) a surface-exchange coefficient of $k^*_{\mathrm{O}} = 1.45 \times 10^{-9}\,\mathrm{cm\,s^{-1}}$ was assumed. Plots (d) – (f) correspond to constant source conditions. In the first 2 µm significant differences between the two series due to the influence of k^* are discernible. At larger penetration depth, however, the contours coincide in shape in both cases.

6.2 Impact of dislocation loops : Appearance of third feature

In the following we take the existence of SCL at the sample surfaces for granted and the SCL-Model being valid in describing this phenomenon as demonstrated in $SrTiO_3$ single

crystals[16]. In most commercially available $SrTiO_3$ single crystals there is however a high density of dislocations present,[29] particularly in the near-surface area.[30] It will be shown, that these dislocations and arrays thereof can also influence the diffusion behaviour and impede the interpretation of tracer diffusion profiles.

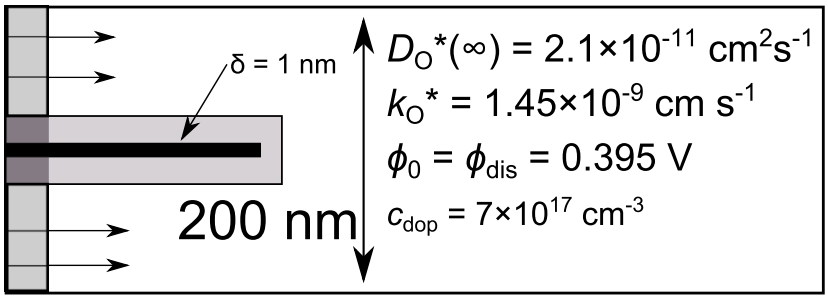

Figure 6.7: DIS-MODEL A dislocation loop at the surface represented as a region of suppressed diffusion inside the dislocation core $D^*(DIS)$ (dark grey area) with a space-charge-layer attached to it (light grey area). The parameters used are given as well. For both the surface and the dislocation core were assumed to posses the same potential relative to the bulk material. In most of the cases (see text) the assumed diffusion coefficient inside the dislocation loop was $D_O^*(\mathrm{DIS}) = 5 \times 10^{-10}\,\mathrm{cm}^2\,\mathrm{s}^{-1}$

A way how dislocations near the surface might influence the diffusion profiles is that space-charge layers around them result in regions where oxygen vacancies are strongly depleted. These depletion regions would effectively block the tracer when diffusing into the crystal as oxygen diffusion is mediated by oxygen vacancies (cf. Sec. 2.5). To model this the influence of these blocking regions we assumed dislocation loops to be present with a highly increased density in the first micrometer below the sample surface, as observed by transmission electron microscopy.[30]

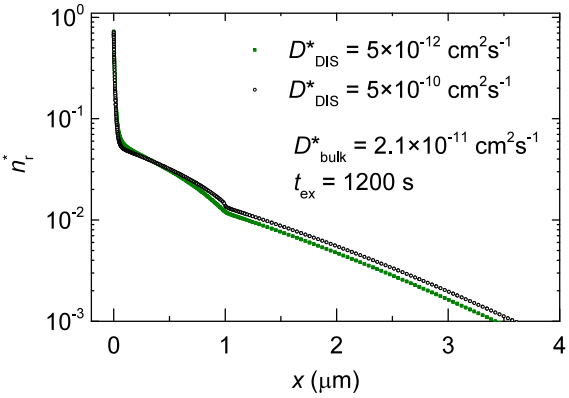

Figure 6.8: Simulated oxygen tracer diffusion profiles resulting from diffusion through a SCL at a surface with an additional SCL around dislocations. (Model depicted in Fig. 6.7). Here different diffusion coefficients inside the dislocation core are assumed. It is evident, that a change in $D_O^*(\mathrm{DIS})$ by two orders of magnitude has no significant impact.

A simple schematic model of these dislocation loops with a surrounding SCL is depicted in Fig. 6.7. It has to be emphasised that dislocations do not end in the bulk and thus the picture used is an oversimplification. Nonetheless, the gray shaded, perturbed area in Fig. 6.7 can as well be regarded as a section of an entire dislocation loop or an array of several dislocations around which the oxygen vacancy concentration is strongly depleted.

In the following it is further assumed that diffusion inside the dislocation core is slower than in the surrounding bulk material.

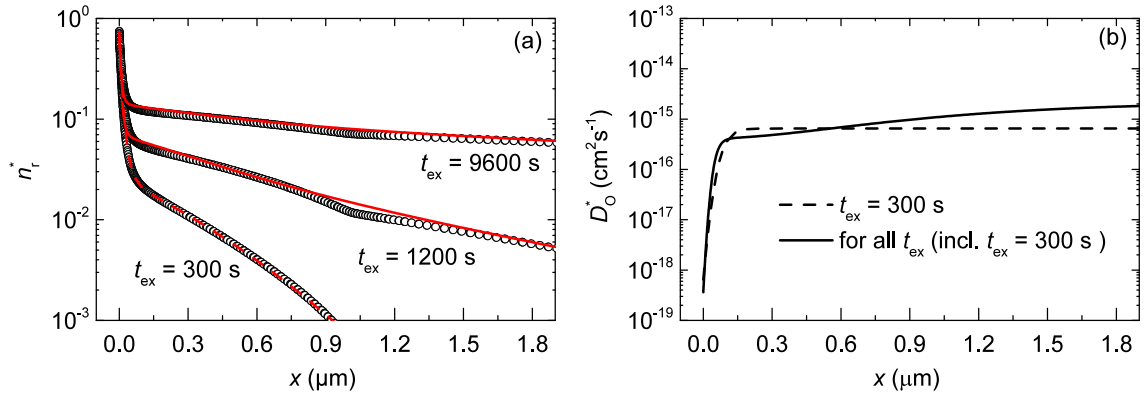

Figure 6.9: (a) Simulated oxygen tracer diffusion profiles for different t_{ex}. The impact of the SCL around the dislocations at the sample surface only becomes apparent at long diffusion time. For the shortest diffusion time it seems that only two and not three features are present. (b) This is also reflected in the spatial variation of the assumed tracer diffusion coefficient. A $D^*_O(x)$ exhibiting an additional reduction in the first µm has to be assumed for the longer diffusion profiles. This model is also valid for the shortest profile at $t_{ex} = 300$ s.

It can be shown, however, that upon inverting the the diffusion constants, that means faster diffusion inside the dislocation than in the adjacent bulk material, the shape of the resulting profiles changed only marginally (cf. Fig. 6.8). For this reason it is concluded that the SCL surrounding the dislocation dominates the overall behaviour. For this reason only profiles resulting from the first type of analysis will be further discussed. Profiles simulated for different exchange times t_{ex} are depicted in Fig. 6.9.

In these profiles three features can be discerned after long exchange times, whereas for shorter times corresponding to profile length of less than one micron only two features are visible.

So again the introduction of extended defects into the material causes the resulting profile-shape to be time dependent. Characterization of this dependence can be realized by describing the profiles with a position dependent diffusion coefficient $D^*_O(x)$. For the shortest profile applying the SCL-Model is sufficient to achieve an excellent description of the data. This does not hold true for the longer profiles (Fig. 6.9). By measuring a diffusion profile at a very short exchange time one would thus misinterpret the underlying diffusion mechanism in a sense that the impact of dislocation loops remains unrevealed.

Again, as the time dependent diffusion behaviour is important, for the longer profiles we have to introduce an additional feature resulting in the reduction of the diffusion coefficient at intermediate depth below the sample surface; exactly the behaviour we expect the dislocation loops to cause. This behaviour can be described by superposing an additional Gaussian shaped reduction to $D^*_O(x)$ resulting from the space-charge layer model. This reduction can be expressed as:

$$D^*_O(x) = D^*_O(\infty) e^{-2e\phi(x)/(k_B T)} (1 - \chi e^{x^2/(2\nu^2)}) \tag{6.2}$$

With χ indicating the magnitude of reduction and ν its spatial extend (Fig. 6.9). This intuitive approach can be comprehended by recalling that the dislocation density on polished single

Table 6.2: The SCL-Model works just for the shortest times, the model taking dislocation loops into account works for all profiles. It is especially striking that by not taking the dislocation loops into account and measuring only a short diffusion profile, the value of the bulk diffusion coefficient is drastically underestimated.

-	SCL-Model	Dis-Model
$D^*(\infty)$ (cm^2s^{-1})	$(0.65 \pm 0.05) \times 10^{-11}$	$(2.10 \pm 0.05) \times 10^{-11}$
k^*(cm s^{-1})	$(1.45 \pm 0.05) \times 10^{-8}$	$(1.45 \pm 0.05) \times 10^{-8}$
ϕ_0 (V)	(0.32 ± 0.05)	(0.32 ± 0.05)
$c_{dop}(cm^{-3})$	$(0.25 \pm 0.05) \times 10^{17}$	$(0.70 \pm 0.05) \times 10^{17}$
χ	-	800 nm
ν	-	0.82

crystals typically follows an exponential decay into the bulk.[30] Assuming an exponential decay in vacancy concentration is, however, inexpedient in describing the experimental data. This is because at the interface a far too excessive reduction in vacancies would result. The overlap of space-charge zones as a result of the increased dislocation density at the surface will rather result in the oxygen vacancy concentration to level off towards the surface. To describe such a behaviour the assumption of a Gaussian seems most qualified.
As in our model system the dislocation density is a time-independent variable, it is imperative that the constants used in Eq. (6.2) to describe this influence are time-invariant as well. Therefore one general criterium can be postulated concerning the validity of the description of a diffusion profile

C1′ This model should work for a set of diffusion profiles recorded after different diffusion times.

In our specific case this means that the alternative description solely based on the pure, unmodified SCL-model does not work for the longer profiles. This description violates the condition **C1′** and thus directs to wrong conclusions concerning two aspects: First a far too slow bulk diffusion coefficient $D^*_O(\infty)$ will be assumed, because the profile is dominated by the depletion layers around the dislocation loop in the first micron. For the same reason the reliable extraction of the surface potential ϕ_0 is averted. It is thus of pivotal importance to extract diffusion parameters only from profiles exceeding the length of influence of extended defects such as dislocation loops.
This can only be the case if one is able to extract the same diffusion parameters from profiles recorded after different diffusion times. For this reason again a time-dependent investigation is of paramount importance in order to reliably determine model parameters of the diffusion behaviour in the material.

6.3 Experimental Application

This section is devoted to exemplifying the aforementioned theoretically illustrated aspects. Here the model system employed throughout this work, the $SrRuO_3|SrTiO_3$ heterostructure,

is used.

All data presented in this section were obtained after conducting isotope exchange experiments at a temperature of $T = 1073\,\mathrm{K}$ and at an oxygen partial pressure of $pO_2 = 500\,\mathrm{mbar}$. These experiments were conducted for different exchange times and SIMS profiles were measured at different positions on the sample.

The discussion of defect redistribution phenomena occurring at the $SrRuO_3|SrTiO_3$ will be reserved for a detailed elaboration in Chapter 7.

Here we will rather focus on the phenomenological character of the data presented and primarily discuss the bulk-diffusion behaviour. It will be shown to what the GB-model discussed in Sec. 6.1 fails to describe the bulk diffusion behaviour. It is, however, the model presented in Sec. 6.2 that yields in a valid description of oxygen tracer diffusion in $SrTiO_3$.

6.3.1 GB diffusion

The first question one has to answer when interpreting diffusion profiles exhibiting more than one feature is whether the "diffusion tail", which is the feature extending the furthest into the bulk, can be assigned to fast diffusion along extended defects. In order to check this, diffusion profiles recorded after different exchange times are needed. A set of such diffusion data is depicted in Fig. 6.10 (a). Further processing of these data reveals that a plot of $\ln(n_r^*)$ versus

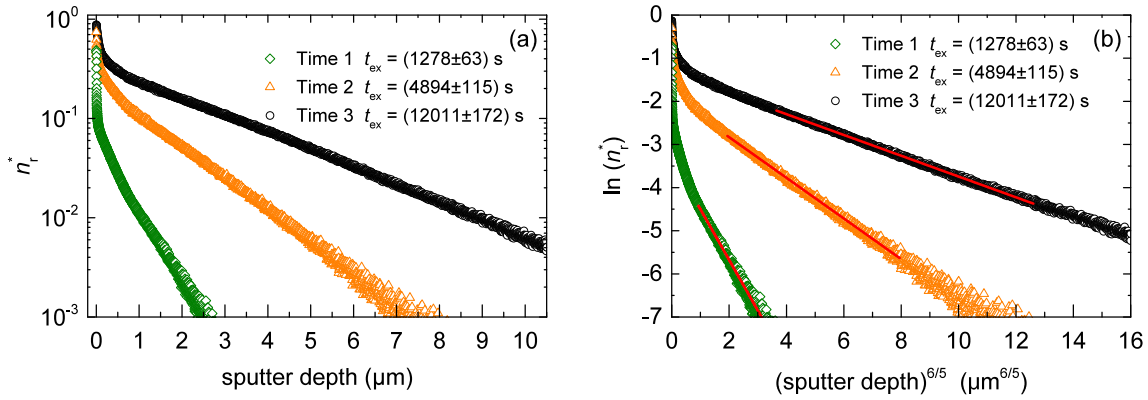

Figure 6.10: (a) Oxygen tracer diffusion profiles measured after different exchange times on a $SrRuO_3|SrTiO_3$ hetero-structure sample. The exchanges were conducted at $T = 1073\,\mathrm{K}$ and $pO_2 = 500\,\mathrm{mbar}$ (b) The same profiles processed according to the procedure outlined in Sec. 6.1.3. The red lines are linear fits to the diffusion tail. The value of the slope extracted from these fits is shown in Fig. 6.11

$x^{6/5}$. (sputter depth) yields straight lines with distinct slopes, as illustrated in Fig. 6.10 (b). The values of these slopes are shown in Fig. 6.11. For the sake of comparison the values for slopes obtained in a similar study by Szot *et al.*[15] are shown as well.

In both cases the dependence of the value with t_{ex} is linear and thus the condition **C1** formulated in Sec. 6.1 is fulfilled. Potential reasons for the discrepancy as far as the absolute values for is concerned are:

1. The difference in dopant concentration in two set of samples investigated, which results in differences in the oxygen vacancy concentration. Here the difference in oxygen partial pressure between the experiments is negligible as the oxygen vacancy concentration can be regarded as independent of this quantity.[3]
2. The absence of an $SrRuO_3$ thin-film, which results in a different surface exchange kinetics.
3. Differences in the pre-anneal procedure of the isotope exchange experiment. In this study the sample was annealed under the *same* conditions as the subsequent isotope exchange, whereas Szot *et al.*[15] exposed their samples to *reducing* conditions prior to the isotope anneal. Their experiment is therefore not a pure tracer diffusion experiment as both chemical diffusion and tracer diffusion (cf. Sec. 2.5) will occur.

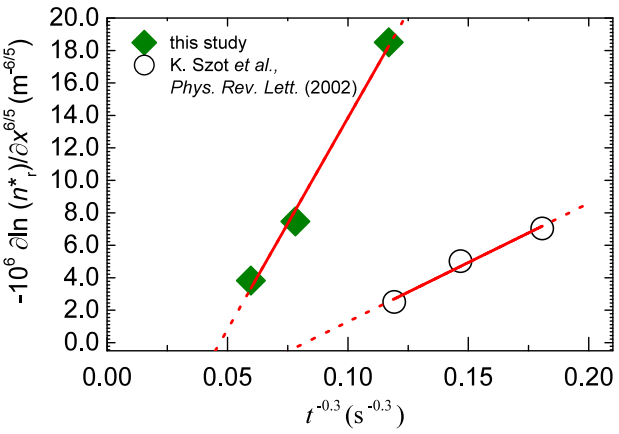

Figure 6.11: Values of the slope for a potential GB diffusion tail extracted after different t_{ex}. Here values for this studies as well as from a comparable study are shown. Both time dependences exhibit a linear behaviour when plottes as a function of $t_{ex}^{-0.3}$. Neither of the fitted lines, however, goes through the origin of the plot. For this reasons the above stated condition **C2** is violated.

Despite these differences in experimental procedure, similarities between both studies are striking and it seems that a similar diffusion behaviour is probed. It is, however, unreasonable to assume that fast diffusion along preferential diffusion paths represents a model for this behaviour. This is because in both above described cases the lines shown in Fig. 6.11 do not go through the origin. Hence condition **C2** is not fulfilled and data processing assuming Harrison type B diffusion behaviour is inappropriate.

6.3.2 Blocking dislocations

As the application of the data processing routine for GB led to inconsistencies, a different model is needed to conclusively explain the observed behaviour.
By close inspection of the profiles shown in Fig. 6.10 (a) three features can be distinguished in the part of the profile corresponding to diffusion in $SrTiO_3$. The first feature could be a consequence of defect redistribution in a space-charge layer at the $SrRuO_3|SrTiO_3$ interface (This phenomenon will receive further attention in Chapter 7). The second feature, extending approx. 1 µm into the bulk, could be induced by space-charge layers around dislocations, which are depleted of oxygen vacancies and thus slightly retard oxygen tracer diffusion diffusion . The third feature would then correspond to unperturbed bulk diffusion of oxygen.
In the here investigated $SrRuO_3|SrTiO_3$ hetero-structure sample an enhanced presence of dislocations in the first 1 µm below the surface of the $SrTiO_3$ substrate can be expected.[30] Unlike the $SrTiO_3$ single crystals used in Ref. [3], the substrates employed for thin-film

Table 6.3: Model parameters employed to describe the diffusion behaviour in the presence of dislocations at the sample surface. (for a detailed description see text) $D^*_O(\infty)$ is the tracer diffusion coefficient far away from the interface; ϕ_i is the interface potential; c_{dop} the assumed dopant concentration; χ and ν describe the magnitude and spatial extend of the blocking effect of the surface dislocation loops.

Constant	Position 1	Position 2	Position 3
$D^*_O(\infty)$ / $cm\,s^{-2}$	$(1.25 \pm 0.05) \times 10^{-11}$	$(1.10 \pm 0.05) \times 10^{-11}$	$(1.10 \pm 0.05) \times 10^{-11}$
ϕ_i / V	(0.257 ± 0.005)	(0.187 ± 0.005)	(0.185 ± 0.005)
$10^{18} \times c_{dop}$ / cm^{-3}	(0.70 ± 0.05)	(0.70 ± 0.05)	(0.70 ± 0.05)
χ	(0.64 ± 0.05)	(0.84 ± 0.05)	(0.83 ± 0.05)
ν / µm	(0.80 ± 0.10)	(0.75 ± 0.10)	(0.76 ± 0.10)
Constant	$t_{ex} = (1257 \pm 57)$ s	$t_{ex} = (4894 \pm 115)$ s	$t_{ex} = (12\,011 \pm 172)$ s
$D^*_O(\infty)$ / $cm\,s^{-2}$	$(1.10 \pm 0.05) \times 10^{-11}$	$(1.00 \pm 0.05) \times 10^{-11}$	$(1.18 \pm 0.05) \times 10^{-11}$
ϕ_i / V	(0.185 ± 0.005)	(0.155 ± 0.005)	(0.185 ± 0.005)
c_{dop} / cm^{-3}	(0.70 ± 0.05)	(0.70 ± 0.05)	(0.70 ± 0.05)
χ	(0.83 ± 0.05)	(0.86 ± 0.05)	(0.91 ± 0.05)
ν / µm	(0.76 ± 0.10)	(0.88 ± 0.10)	(0.91 ± 0.10)

growth in this study did not receive an extended heat treatment apart from the standard procedure described in Sec. 3.2.2. Extended exposure of $SrTiO_3$ to temperatures is known to significantly reduce the dislocation density.[31] Therefore it seems reasonable that here an effect of dislocations is observed and in Ref. [3] a similar obervation is missing. In the present case it was refrained from additional heat treatment, as the vicinal step-structure, indispensable for successful $SrRuO_3$ growth, would be altered as well.

A model taking all three above described phenomena into account is that of a spatially varying diffusion coefficient $D^*_O(x)$ as presented in Sec. 6.2.

In order to test this model first, diffusion profiles recorded at different positions on the $SrRuO_3|SrTiO_3$ sample are compared. As shown in Fig. 6.12 (a), profiles recorded at three different positions could be successfully described with the proposed model. The corresponding profile of the assumed tracer diffusion coefficient is depicted in Fig. 6.12 (c).

When taking a closer look at the values depicted in Table 6.3 the values for $D^*_O(\infty)$ agree very well within their error margin. This is particularly important as $D^*_O(\infty)$ represents a true bulk value and is independent of surface properties.

It is the model parameters describing these surface properties that vary more significantly between the different positions on the surface (see Table 6.3). In light of the widely accepted assumption that extended defects are inhomogeneously distributed especially close to the sample surface,[30,31] this observation is rather an indication of the assumed model's validity than an inconsistency.

To further confirm that the assumption of inhomogeneously distributed extended defects having a blocking effect on oxygen diffusion, tracer diffusion profiles were recorded as a function of exchange time. If the proposed model was valid, then the variation of model parameters describing the spatial variation in $D^*_O(x)$ with time has to be of similar magnitude than the scatter in model parameters with position. This corresponds to condition **C1′**

formulated in Sec. 6.2, only taking spatial inhomogeneities into account as well.

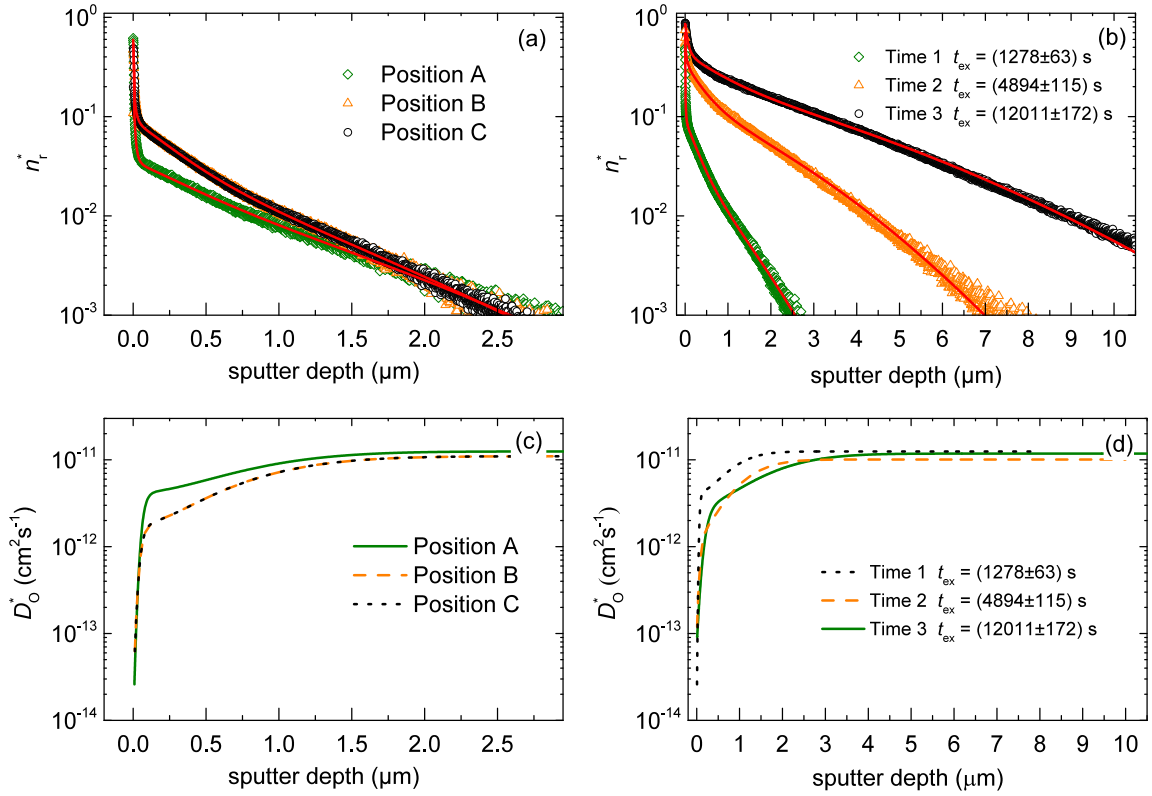

Figure 6.12: Tracer diffusion profiles recorded (a) at different positions on a $SrRuO_3|SrTiO_3$ heterostructure sample and (b) obtained after different exchange times and at different positions on the same sample. in (c) and in (d) the corresponding $D^*_O(x)$ assumed to fit the profiles (red lines in (a) and (b)) are shown.

In Fig. 6.12 (b) diffusion profiles corresponding to different exchange times are shown. All profiles could again be described with the model of a spatially varying diffusion coefficient. This spatial variation is shown in Fig. 6.12 (d).
A comparison of Fig. 6.12 (c) and Fig. 6.12 (d) (the same hold when comparing the values in Table and Table) reveals that the scatter $D^*_O(x)$ due to differences in probing position is approximately the same as the scatter occurring with exchange time. Therefore we can conclude that inhomogeneously distributed dislocations surrounded by space charge layers depleted of oxygen vacancies induce a blocking effect on oxygen diffusion.

6.4 Conclusions

In this chapter tracer diffusion profiles for different conceivable scenarios of complex diffusion behaviour in oxide ceramics were simulated. In all cases the importance to investigate the time dependence of the diffusion behaviour became apparent. In brief, it can be summarised that

1. Successful description of a tracer-diffusion profile with a solution to the diffusion equa-

tion is a neccessary, but insufficient criterion to asses the quality of a diffusion model.

2. Only a time-dependent investigation can provide the neccessary confirmation of a model's validity in describing the envisioned diffusion behaviour.

3. Successful application of the theoretically derived criteria to experimental data reveals the blocking effect of regions depleted of oxygen vacancies around dislocations on oxygen tracer diffusion.

These criteria can be generalised and are applicable to all kind of models proposed as a solution to the diffusion equation. A time-dependent investigation might be dispensable in cases a lot is known about the material and the diffusion profiles clearly exhibit the classically expected behaviour. It is however indispensible in all cases deviations from this classic behaviour occur. This is particularly the case for diffusion in thin film heterostructures, through space-charge layers and diffusion involving grain boundaries and dislocations.

Bibliography

[1] P. Fielitz and G. Borchardt, *Solid State Ionics*, 2001, **144**, 71–80.
[2] R. A. De Souza and M. Martin, *MRS Bulletin*, 2009, **34**, 907–914.
[3] R. A. De Souza, V. Metlenko, D. Park and T. E. Weirich, *Phys. Rev. B*, 2012, **85**, 174109.
[4] R. A. De Souza, M. J. Pietrowski, U. Anselmi-Tamburini, S. Kim, Z. A. Munir and M. Martin, *Phys. Chem. Chem. Phys.*, 2008, **10**, 2067–2072.
[5] H. Schraknepper, C. Baumer, R. Dittmann and R. De Souza, *Phys. Chem. Chem. Phys.*, 2014, –.
[6] P. Fielitz, G. Borchardt, M. Schmücker and H. Schneider, *Solid State Ionics*, 2003, **160**, 75 – 83.
[7] R. A. De Souza and J. A. Kilner, *Solid State Ionics*, 1998, **106**, 175–187.
[8] R. A. De Souza and M. Martin, *Phys. Chem. Chem. Phys.*, 2008, **10**, 2356–2367.
[9] P. C. McIntyre, *J. Am. Ceram. Soc.*, 2000, **83**, 1129–1136.
[10] T. Frömling, H. Hutter and J. Fleig, *J. Am. Ceram. Soc.*, 2012, **95**, 1692–1700.
[11] T. Frömling, J. Hou, W. Preis, W. Sitte, H. Hutter and J. Fleig, *J. Appl. Phys.*, 2011, **110**, 043531.
[12] R. Meyer, R. Waser, J. Helmbold and G. Borchardt, *Phys. Rev. Lett.*, 2003, **90**, 105901.
[13] R. A. De Souza, C. Voisin, H. Schraknepper, M. Teusner, M. Kessel, P. Dufour, C. Tenailleau and S. Guillemet-Fritsch, *Phys. Chem. Chem. Phys.*, 2014, **16**, 2568–2575.
[14] M. Burriel, G. Garcia, J. Santiso, J. Kilner, R. Chater and S. Skinner, *J. Mater. Chem.*, 2007, **18**, 416–422.
[15] K. Szot, W. Speier, R. Carius, U. Zastrow and W. Beyer, *Phys. Rev. Lett.*, 2002, **88**, 75508.
[16] R. A. De Souza, *Phys. Chem. Chem. Phys.*, 2009, **11**, 9939–9969.
[17] J. C. Fisher, *J. Appl. Phys.*, 1951, **22**, 74–77.
[18] Y.-C. Chung and B. J. Wuensch, *J. Appl. Phys.*, 1996, **79**, 8323–8329.
[19] H. Mehrer, *Diffusion in solids: fundamentals, methods, materials, diffusion-controlled processes*, Springer, 2007, vol. 155.
[20] *Diffusion in Condensed Matter*, ed. P. Heitjans and J. Kärger, Springer, 2005.
[21] R. A. De Souza and J. F. Kilner, J. A .and Walker, *Mater. Lett.*, 2000, **43**, 43–52.
[22] M. Leonhardt, J. Jamnik and J. Maier, *Electrochem. Solid-State Lett.*, 1999, **2**, 333–335.
[23] J. Jamnik and J. Maier, *Ber. Bunsenges. Phys. Chem.*, 1997, **101**, 23–40.
[24] J. Jamnik and J. Maier, *J. Phys. Chem. Solids*, 1998, **59**, 1555 – 1569.
[25] L. G. Harrison, *Trans. Faraday Soc.*, 1961, **57**, 1191–1199.
[26] W. Preis and W. Sitte, *J. Appl. Phys.*, 2005, **97**, –.
[27] W. Preis and W. Sitte, *Solid State Ionics*, 2006, **177**, 3093 – 3098.
[28] H. S. Levine and C. J. MacCallum, *J. Appl. Phys.*, 1960, **31**, 595–599.
[29] B. Stäuble-Pümpin, B. Ilge, V. Matijasevic, P. Scholte, A. Steinfort and F. Tuinstra, *Surf. Sci.*, 1996, **369**, 313 – 320.
[30] R. Wang, Y. Zhu and S. M. Shapiro, *Phys. Rev. Lett.*, 1998, **80**, 2370–2373.
[31] A. Paladino, L. Rubin and J. Waugh, *J. Phys. Chem. Solids*, 1965, **26**, 391 – 397.

Chapter 7

The $SrRuO_3|SrTiO_3$ interface: A SIMS approach

Metal-semiconductor interfaces are of pivotal importance to the operation of classical semiconductor devices.[1] The desire to optimise these devices has led to numerous experimental studies and has fueled the development and refinement of a theoretical framework allowing for the prediction of interface properties.[2–4] In the emerging field of oxide electronics the situation is different: Despite theoretical considerations based on classical semiconductor concepts,[5–7] there is a lack of experimental data that could be used to validate and adjust these models.[8,9] As outlined in Sec. 2.4, the quantity used to characterize a metal-semiconductor contact is the difference in electrochemical potential of electrons between the materials: the Schottky barrier height (SBH). This value is traditionally determined by various methods[2]:

1. Current/voltage characteristics
2. Capacitance measurements
3. Photoelectric measurements
4. Photoelectron emission spectroscopy

The common ground of all four methods is that electrons are employed to probe the interface properties. In the first three cases this requires that both involved materials possess a sufficient electronic conductivity. In case of photoelectron emission spectroscopy the heterostructure under investigation cannot exceed a certain thickness, as the emission depth of photoelectrons is restricted to a few nm.[9] Geometrical constraints also complicate less widespread scanning probe methods used to reveal electrochemical properties of all-oxide interfaces.[10] Here typically available probe dimensions restrict the lateral resolution to about 20 nm.[10–12] An additional problem is that unlike in traditional semiconductor materials, in oxides the composition varies with temperature (cf. Sec. 2.3.1). In $SrTiO_3$, for instance, variations in composition with temperature induce non-trivial changes in charge carrier concentration and thus their electrochemical potentials (e.g. the Fermi level as shown in Sec. 2.3.3).
The underlying idea of the study presented in the following is not to probe electrons, but ions to determine the properties of an all-oxide metal semiconductor interface.

Here again the prototype system of this thesis, the $SrRuO_3|SrTiO_3$ heterostructure, will be used. In this particular case the redistribution of oxygen ions at the $SrRuO_3|SrTiO_3$ interface can be revealed by isotope exchange experiments and subsequent SIMS depth profiling.
In the first part of this chapter the experimental procedure used and the results obtained are presented. Subsequently these results will be discussed with particular emphasis on assessing the reliability of the presented method.

7.1 Procedure and results

Properties of the $SrRuO_3|SrTiO_3$ interface will be derived from oxygen isotope diffusion profiles. Such an isotope profile along with the parameters of the exchange experiment is exemplary depicted in Fig. 7.1. Here the corrected isotope fraction n_r^* is plotted versus the sputter depth. The position of the interface was determined from sharp rise in Ti-intensity in the SIMS profiles (not shown); the film thickness was measured by means of XRR and the crater depth by means of profilometry. In the following first the details of the data evaluation procedure are described. Subsequently the results of this evaluation are presented. Finally, an Arrhenius type investigation of the bulk diffusion coefficient in $SrTiO_3$ is compared to literature data in order to provide a consistency check of the presented analysis.

7.1.1 Data processing

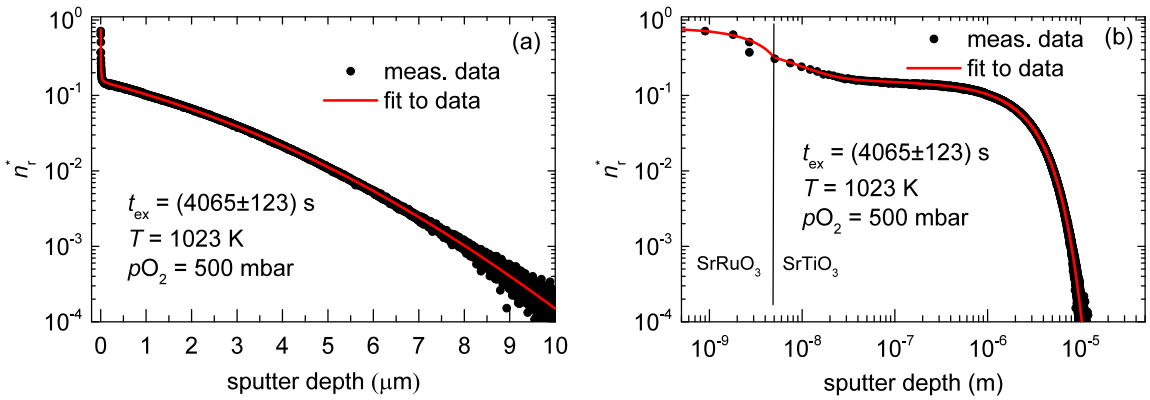

Figure 7.1: Measured tracer diffusion profiles obtained on a $SrRuO_3|SrTiO_3$ heterostructure sample (a) in the conventional and (b) in a log-log representation. The red line is the fit obtained by applying the here discussed interface model to fit the obtained data.

Inspecting the tracer diffusion profile shown in Fig. 7.1, three main features can be discernined: First, a profile in the $SrRuO_3$ film close to the surface of the entire structure. Second, a feature close to the $SrRuO_3|SrTiO_3$ interface. This feature extends several tens of nm into the $SrTiO_3$. Third, a long tracer diffusion profile extending several microns into the $SrTiO_3$ crystal.
Description of this three-fold n_r^*-profile is done by numerically solving the diffusion equation in the film and in the substrate. The film-substrate structure is implemented into the finite

element simulation package COMSOL Multiphysics v. 4.3 (COMSOL AB, Stockholm, Sweden). In order to obtain agreement between simulated and experimental data, three issues were considered:

1. As all films were exposed to comparably long pre-anneal and exchange times, it became necessary to consider both already observed and characterized diffusion mechanisms in thin-film $SrRuO_3$, An_{sl} and An_{sl} (see Chapter 4), to describe the diffusion profile in the structure.In order to account for both mechanisms the free parameters $D^*_O(An_{sl})$, $k^*_O(An_{sl})$ and $D^*_O(An_{fa})$, $k^*_O(An_{fa})$ are used.

2. The second feature was described with a local spatial variation of D^* in the $SrTiO_3$. $D^*(x)$ was obtained by assuming the existence of a space-charge layer in $SrTiO_3$ induced by the $SrRuO_3|SrTiO_3$ interface. The theoretical background and details of this procedure were described in Sec. (2.5). Here it shall be emphasised that the main variable characterising the interface is the interface potential ϕ_i. The dopant concentration $c_{dop} = (7.0 \pm 0.5) \times 10^{17}\,cm^{-3}$ was assumed constant for all samples investigated.

3. The diffusion in bulk $SrTiO_3$ far away from the interface is characterised by a bulk diffusion coefficient D^*_∞. In some cases, however, the diffusion process is altered by dislocations and additional space-charge layers around them. Here the modeling process was adapted according to the procedure detailed in Chapter (6). Profiles resulting from this kind of analysis are depicted in Fig. 7.2.

Fitting of a solution to experimental data is done by variation of the diffusion and electrostatic parameters and visual comparison of computed and measured profile; parameters are varied iteratively until an agreement between measured and computed profile is obtained. At each temperature investigated several profiles were recorded. In all cases at least two exchange experiments were conducted, resulting in different penetration depth of the tracer into the substrate. In some cases the tracer diffusion profiles were recorded at different sample positions as well. A more detailed discussion of the profile analysis in bulk $SrTiO_3$ was

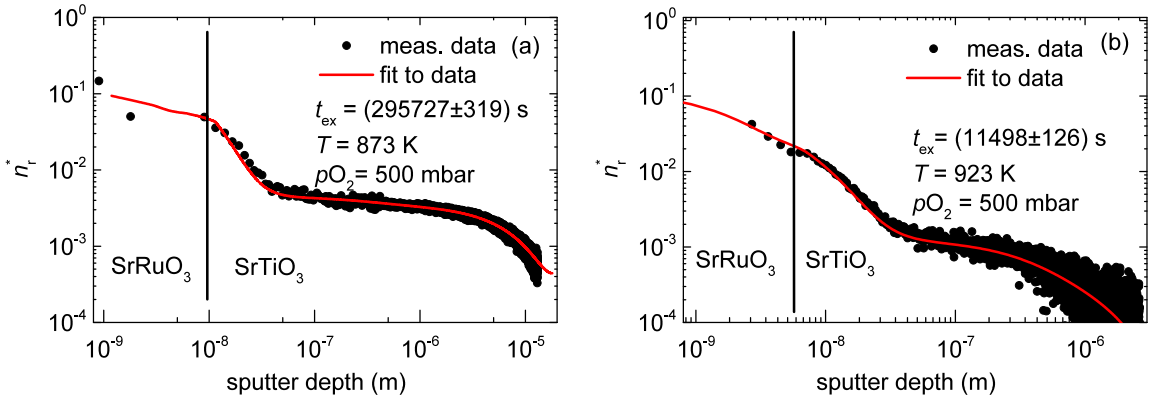

Figure 7.2: Measured tracer diffusion profiles obtained on two different $SrRuO_3|SrTiO_3$ heterostructure samples (a) at $T = 873\,K$ and (b) at $T = 923\,K$. In both cases the blocking impact of dislocation, as described in Sec. 6.2, was considered when fitting the data.

given in Chapter 6. As the validity of the model used here was confirmed there as well, in the following the focus will lie on the interface potential ϕ_i. Values for $D_O^*(\infty)$ will also be presented. These values will be compared with previously obtained results. This comparison provides an excellent consistence check of the conducted analysis.

7.1.2 Interface potential

Values for ϕ_i obtained are depicted as a function of temperature in Fig. 7.3. These values exhibit a slight dependence on the temperature with a temperature coefficient $\kappa = (3.64 \pm 1.65) \times 10^{-4}\,\mathrm{K}^{-1}$. It is noteworthy that this coefficient is of the same order of magnitude as the temperature dependence of the optical band-gap E_{gap} as reported in Ref. [13] ($\kappa = 6 \times 10^{-4}\,\mathrm{K}^{-1}$).

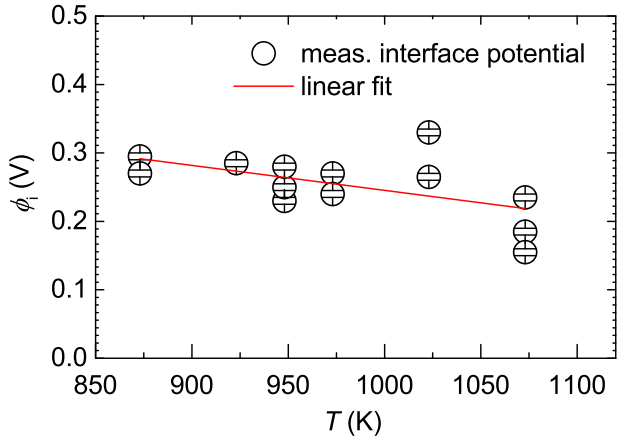

Figure 7.3: Values of the interface potential ϕ_i as a function of temperature. The values depend on the temperature with $\kappa = (3.64 \pm 1.65) \times 10^{-4}\,\mathrm{K}^{-1}$.

The fitting procedure described above is very sensitive to ϕ_i, hence this value is determined with a low fitting error. Measurements at different sample positions and after different exchange times, however, show larger scatter. The reason for this scatter is the fact that we employed a homogeneous interface model to obtain ϕ_i, but the potential barrier at metal-semiconductor contact is generally inhomogeneous.[14–16] Therefore measurements of ϕ_i at different positions on a sample will reflect these inhomogeneities.

7.1.3 Bulk diffusion : A consistency check

Since many defect properties of $SrTiO_3$ where deduced from oxygen diffusion measurements conducted on bulk $SrTiO_3$, values for D_O^* are abundantly available in literature (see Ref. [17], Sec. (2.3.3) and references therein). Particularly the diffusion study presented in Ref. [17] was conducted on single crystal $SrTiO_3$ from the same supplier as the substrates used in this study . Hence similar properties can be expected. Especially the impurity level, which stipulates the oxygen vacancy concentration and the magnitude of D_O^*, be expected expected to be comparable.

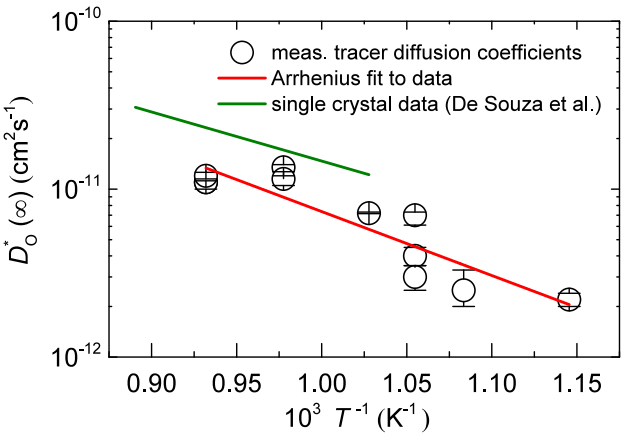

Figure 7.4: Arrhenius analysis of the measured tracer diffusion coefficients yields an activation enthalpy of $\Delta H_{D^*_O} = (0.76 \pm 0.12)$ eV. For comparison the Arrhenius analysis of tracer diffusion coefficients measured in Ref. [17] is shown. Here the activation enthalpy was determined to $H_{D^*_O} = (0.58 \pm 0.08)$ eV

For this reason the results for D^*_O presented here shall not be regarded as novel, though the temperature range could be slightly extended towards lower values. Rather the comparison of the here obtained data with those from Ref. [17] provides a consistency check of the above described analysis. The determined values for D^*_O are shown along with the corresponding Arrhenius fit and literature data in Fig. (7.4). From our data an activation enthalpy for oxygen tracer diffusion of $\Delta H_{D^*_O} = (0.76 \pm 0.12)$ eV can be determined. This value is in reasonable aggreement with previous reports of this value, which settle in the range of $\Delta H_{D^*_O} = 0.60$ eV to 0.70 eV (cf. Ref. [17] and references therein). This shows that the applied method of profile-fitting is consistent with other diffusion studies on $SrTiO_3$ and the observed local variations in the diffusion coefficient occur as a consequence of the $SrRuO_3|SrTiO_3$ interface.

7.2 Discussion

7.2.1 Validity of interface description

Discussing charge carrier redistribution at the $SrRuO_3|SrTiO_3$ interface, the first intriguing question is: To what extend does Poisson's equation reduces to Laplace equation in the metallic oxide $SrRuO_3$ (as the relative static permittivity $\epsilon_r \to \infty$ holds in a metal); or is there a measurable redistribution of charges in $SrRuO_3$?

In the classical picture a metal is field free and as Laplace equation holds, which means that the electric potential in the metallic bulk $SrRuO_3$ would be constant. Any charges would be screened within a infinitesimal δ-layer at the metal-semiconductor interface.

In a realistic scenario, however, charges are screened within a finite screening length λ_S penetrating into the metal. The details of this phenomenon and its technological implications particularly for the occurrence of dead-layers in capacitors have been discussed elsewhere.[18,19] The theory of Dawber and Scott[19] yields a value for the screening length $\lambda_S \approx 0.4$ nm, a value experimentally confirmed by Sinnamon *et al.*.[20] This implies that the redistribution of oxygen vacancies does not exceed one unit cell of $SrRuO_3$. Considering that the depth-resolution of SIMS of lies in the order of 1 nm, this means that we won't be able to resolve any charge carrier redistribution in $SrRuO_3$.

As a consequence the above used Schottky-model describing the charge carrier redistribution

at the $SrRuO_3|SrTiO_3$ can be regarded as sufficiently accurate.

7.2.2 Assessment of the used method and the model system

As already stated, the charge carrier redistribution and as a consequence the tracer diffusion coefficient is decisively influenced by the drop in electric potential ϕ_i across the interface.
In light of the fact that the here presented method of measuring ϕ_i is novel and thus not well established, one needs to be certain that indeed different interfaces give different results for the extracted potentials. In this study the derived interface potentials were of the order of $\phi_i \approx 0.25\,V$. Values for the gas-solid interface of oxygen and $SrTiO_3$ are significantly higher, in the order of $\phi_{0\,surface} \approx 0.5\,V$.[17]
Both, interface as well as surface potentials, were obtained by analysing oxygen isotope diffusion profiles. Therefore one can concluded that a $SrRuO_3$ thin film indeed alters the defect behaviour at the $SrRuO_3|SrTiO_3$ interface and the observations are not due to methodical artifacts.
In the following, the here measured values for the interface potential will be compared to reference values obtained by other means. This is of particular importance, as the way of sample preparation and annealing can decisively determine the material and thus the interface properties.[21,22]
As the $SrRuO_3|SrTiO_3$ has been characterized by a variety of different techniques, we will now compare these values with with one obtained by means of XPS on $SrRuO_3|SrTiO_3$ reference samples. These $SrRuO_3|SrTiO_3$ reference samples were prepared in exactly the same manner as those used in the diffusion studies (cf. Sec. 3.2.3).
To facilitate a comparison, we have to take into account that in most studies donor doped $SrTiO_3$ was used, which implicitly indicates that Φ^n_{SB} was measured. In all interface models, Φ^p_{SB} and Φ^n_{SB} are related with the bandgap E_{gap} via (see Sec. 2.4 or Refs. [1,2,23]):

$$E_{gap} = \Phi^n_{SB} + \Phi^p_{SB} \tag{7.1}$$

Applying Eq. (7.1) to our own and so far reported values for the SBH yields values listed in table Tab. 7.1. The first conclusion of this comparison is that the experimentally obtained value from XPS measurements for Φ^p_{SB} aggrees well with those converted via Eq. (7.1) from several previous studies. Thus it can be concluded that the XPS room temperature values for Φ^p_{SB} and Φ^n_{SB} can be regarded as reference values a further discussion of the values obtained by SIMS profile analysis can be based on. As the the samples used in the XPS analysis w, it can be further concluded that the prepared heterostructure samples represent an excellent reference system to explore the rather novel method of tracer diffusion analysis to extract SBHs.

7.2.3 Schottky barrier heights determined by means of SIMS

In order to be able to compare the measured values for ϕ_i with above listed SBHs and further classify these values within the existing theoretical framework, we have to convert ϕ_i into

Table 7.1: Values of the Schottky barrier heights for the $SrRuO_3|SrTiO_3$ interface obtained by means of different methods and on differently doped $SrTiO_3$ substrates. The bold values represents the measured value of the SBH. The corresponding value for either Φ^{n}_{SB} or Φ^{p}_{SB} was calculated assuming a value for the band-gap for $SrTiO_3$ of $E_{gap} = 3.1\,eV$ ($T = 300\,K$)

Φ^{p}_{SB} (eV)	Φ^{n}_{SB} (eV)	Reference
(**1.90 ± 0.10**(	(1.20 ± 0.10)	this study XPS by A. Klein
1.90	**1.20**	[24], electrical
(1.63 ± 0.01)	(**1.47 ± 0.01**)	[25], optical
(1.75 ± 0.10)	(**1.35 ± 0.10**)	[25], electrical
(1.90 ± 0.10)	(**1.20 ± 0.10**)	[26], optical

SBHs. Here the following relation holds (cf. Sec. 2.4):

$$\Phi^{p}_{SB} = \phi_i + (E_f - E_v) \tag{7.2}$$

with $(E_f - E_v)$ being the valence band offset depending on temperature T and dopant concentration c_{dop} as shown in Sec. (2.3.3). The measured values for ϕ_i, the derived SBHs Φ^{p}_{SB} as well as the valence band offset $(E_f - E_v)$ are shown as a function of temperature in Fig. 7.5.

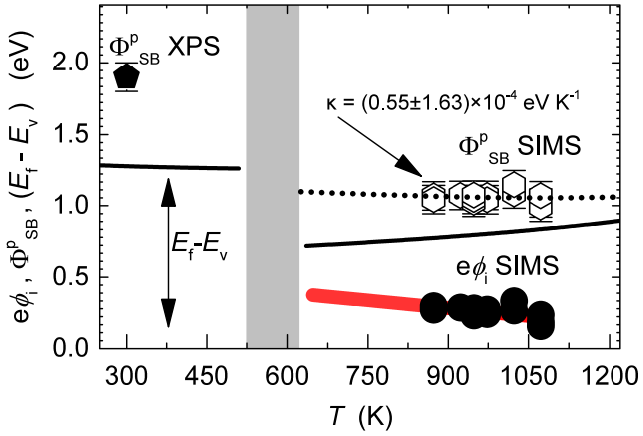

Figure 7.5: Measured quantities and derived values characterising the $SrRuO_3|SrTiO_3$ interface. $e\phi_i$ are the measured interface potentials, from which the values for the SBH $e\Phi^{p}_{SB}$ (SIMS) were derived. For these calculations the valence band offset $(E_f - E_v)$ was used. $e\Phi^{p}_{SB}$ (XPS) is the interface potential directly measured by means of XPS at room temperature. The dotted lines represent interpolations to lower and higher temperatures using the temperature dependences of $(E_f - E_v)$ and $e\phi_i$. No potentials are drawn in the gray shaded area, as here the oxygen incorporation reaction becomes increasingly slower and the defect behaviour depends on kinetics (e.g. cooling/heating rate). It is noteworthy that at high temperatures the Fermi-level is below $e\Phi^{p}_{SB}$ (SIMS), whereas at low temperatures it is slightly above the energy level defined by these values.

When first focusing on the values derived for Φ^{p}_{SB} in the temperature regime above $T > 650\,K$, it is apparent that the Φ^{p}_{SB} is independent of temperature (temperature coefficient $\kappa = -(0.55 \pm 1.63) \times 10^{-4}\,eV\,K^{-1}$). This behaviour strongly suggests that the Fermi level E_f at

the interface is pinned relative to the valence band edge E_v. A similar behaviour has been observed for different Si-metal junctions.[27–30] Assuming the same behaviour for $SrRuO_3|SrTiO_3$, the position of E_f at the interface would be $\Phi_{SB}^p = 1\,eV$ above the valence band edge E_v.

Ab-initio calculations that could help to understand the electronic interface structure are scarce. Albina *et al.*[31] suggested the existence of metal induced gap states (MIGS) and calculated values for the SBH in the range of 1.1 eV to 1.4 eV. Values in the same range were obtained by Stengel and Spaldin (1.49 eV)[18], as well as for the comparable $SrRuO_3|BaTiO_3$ interface (1.4 eV).[32]

Since these results were obtained by first principle DFT calculations, it is obvious that these values represent the electronic interface structure and thus are comparable to the measured SBH of $\Phi_{SB}^p = 1\,eV$. One should, however, keep in mind that the here drawn comparison is afflicted with several uncertainties. First, all calculations correspond to 0 K energies. This means that in any case a temperature difference of at least 300 K between values derived from *ab-initio* calculations and measured quantities exists. Second, ideal interfaces and no point-defects are included in the *ab-initio*. Therefore differences between calculations and experiments are to be expected.

Despite these systematic drawbacks, Klein[8] pointed out that values for SBHs derived from *ab-initio* super cell calculations are prone to give more accurate results than any other computational method can provide.[33]

Among the most frequently non-first-principle methods the tight-binding model is the one that finds considerable application in calculating interface and surface states. In a series of studies Robertson *et al.*[5–7,34] provide explanations for measured SBH of various different systems. For $SrTiO_3$ a charge neutrality level (CNL) of 2.6 eV above E_v is suggested. In the Bardeen limit of strong Fermi level pinning this would advocate a SBH of $\Phi_{SB}^p = 2.6\,eV$, a value clearly far out of experimentally supported bounds.

The experimentally determined Φ_{SB}^p presented, however, clearly are independent of temperature and thus a pinning of the Fermi-level to interface states is suggested. Therefore further reasoning of the CNL derived by Robertson*et al.*assuming slope parameters as introduced in Sec. 2.4.2 is inexpedient at this point.

We thus conclude that Fermi level pinning at interface states approx. 1 eV above the valence band edge is the reason for the observation of a temperature independent SBH of $\Phi_{SB}^p = 1\,V$ in the temperature regime above $T \geq 650\,K$. (cf. Fig. 7.5)

Comparing the high-temperature SBHs with the abundantly available, well ascertained room temperature values of $\Phi_{SB}^p \approx 1.9\,V$, a striking difference is apparent.

Assuming now that for the above stated reasons, the SBHs were reliably determined in both, the high- as well as the low-temperature regime, this discrepancy has to stem from an inherent behaviour of the system.

The only property changing between high- and low temperature regime is the position of the Fermi-level above the valence band edge, which varies depending on the surface exchange reaction and the rate of cooling and heating in the temperature regime 500 K–650 K(see behaviour of $(E_f - E_v)$ in Fig. 7.5).

This means that in the high- and low temperature regime different Fermi levels align and therefore different barrier heights are to be expected in the respective regimes. Such a behaviour is, however, only to be expected if the SBH depends on the position of the Fermi level. As this is only the case when the Fermi level is pinned (to a certain degree) at the metal-semiconductor interface, we can regard this as an additional indication for strong Fermi level pinning.

For many systems it is known that interface states are discontinuous and can be thought of as donor- or acceptor bands with a certain width, present at the interface. (Fig. 7.6)

Assuming a similar behaviour for $SrRuO_3|SrTiO_3$ would make the discrepancy between the high and the low temperature regime comprehensible: By freezing the the oxygen incorporation reaction, the Fermi level is shifted above the donor-type interface states. Therefore these states can no longer pin the Fermi level and the net interface charge would be zero and the behaviour would correspond to the Mott-Schottky limit. Such a behaviour was observed for and is described in more detail in the textbook by Rhoderick and Williams (pages 20 *ff.*).[2]

An indication that such this suggestion could be indeed valid is that when employing the appropriate constants and with the Mott-Schottky rule, we get:

$$e\Phi_{SB}^{p} = E_g + e\chi_{SrTiO_3} - e\Phi_{SrRuO_3} = 3.1\,\text{eV} + 4.1\,\text{eV} - 5.2\,\text{eV} = 2.0\,\text{eV} \tag{7.3}$$

Considering the simplistic nature of the Mott-Schottky rule, this is in excellent agreement with room-temperature data for Φ_{SB}^{p} listed in Table 7.1.

In brief the high temperature behaviour of the $SrRuO_3|SrTiO_3$ interface is dominated by interface states pinning the Fermi level at a position approximately 1 eV relative to the valence band edge. At low temperatures, on the other hand, the Fermi level is shifted above these interface states and the behaviour is governed by the work function of the metal, in this case $SrRuO_3$.

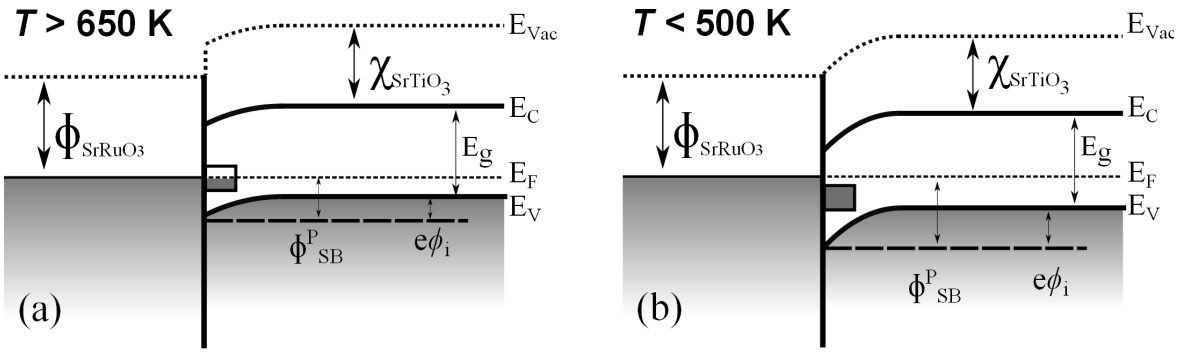

Figure 7.6: Assumed model for the electronic behaviour at the $SrRuO_3|SrTiO_3$ interface. (a) In the high temperature regime, the Fermi level is pinned to interface states exciting approx. 1 eV above the valence band edge. (b) In the low temperature remige, the Fermi level is above the interface states and the behaviour is thus determined by the differences in between the work-function of $SrRuO_3$ and electron affinity of $SrTiO_3$

7.3 Conclusion

In this chapter it was shown, how interface potentials can be determined by interpreting oxygen tracer diffusion profiles measured on $SrRuO_3|SrTiO_3$ heterostructure samples.
On the basis of the derived interface potentials, Schottky barrier heights were calculated and a model for electronic bahviour of the interface was established.
In the high temperature regime ($T > 650\,K$),the Schottky barrier height is temperature independent and thus the Fermi level of $SrTiO_3$ is pinned to interface states.
For lower temperatures $T < 500\,K$, interface states are negligible and the overall behaviour is determined by the difference in work functions of $SrRuO_3$ and electron affinity of $SrTiO_3$.

Bibliography

[1] S. M. Sze and K. K. Ng, *Physics of semiconductor devices*, John Wiley & Sons, 2006.
[2] E. H. Rhoderick and R. Williams, *Metal-semiconductor contacts*, Clarendon Press Oxford, 1988, vol. 2.
[3] H. Lüth, *Solid surfaces, interfaces and thin films*, Springer, 2001, vol. 4.
[4] R. T. Tung, *Mater. Sci. Eng., R*, 2001, **35**, 1 – 138.
[5] J. Robertson, *J. Vac. Sci. Technol., A*, 2013, **31**, –.
[6] J. Robertson, *J. Vac. Sci. Technol., B*, 2000, **18**, 1785–1791.
[7] J. Robertson and C. W. Chen, *Appl. Phys. Lett.*, 1999, **74**, 1168–1170.
[8] A. Klein, *Thin Solid Films*, 2012, **520**, 3721 – 3728.
[9] A. Klein, *J. Am. Ceram. Soc.*, 2013, **96**, 331–345.
[10] S. S. Nonnenmann, R. Kungas, J. Vohs and D. A. Bonnell, *ACS nano*, 2013, **7**, 6330–6336.
[11] J. Seidel, L. W. Martin, Q. He, Q. Zhan, Y.-H. Chu, A. Rother, M. Hawkridge, P. Maksymovych, P. Yu, M. Gajek *et al.*, *Nat. Mater.*, 2009, **8**, 229–234.
[12] J. M. R. Weaver and D. W. Abraham, *J. Vac. Sci. Technol. B*, 1991, **9**, 1559–1561.
[13] T. Bieger, J. Maier and R. Waser, *Solid State Ionics*, 1992, **53-56, Part 1**, 578 – 582.
[14] J. H. Werner and H. H. Güttler, *J. Appl. Phys.*, 1991, **69**, 1522–1533.
[15] H. Kim, C. Park, S. Lee and D.-W. Kim, *J. Phys. D: Appl. Phys.*, 2009, **42**, 055306.
[16] T. Shimizu and H. Okushi, *J. Appl. Phys.*, 1999, **85**, 7244–7251.
[17] R. A. De Souza, V. Metlenko, D. Park and T. E. Weirich, *Phys. Rev. B*, 2012, **85**, 174109.
[18] M. Stengel and N. A. Spaldin, *Nature*, 2006, **443**, 679–682.
[19] M. Dawber and J. Scott, *Jpn. J. Appl. Phys.*, 2002, **41**, 6848.
[20] L. J. Sinnamon, R. M. Bowman and J. M. Gregg, *Appl. Phys. Lett.*, 2001, **78**, 1724–1726.
[21] F. Roccaforte, F. La Via, V. Raineri, P. Musumeci, L. Calcagno and G. Condorelli, *Appl. Phys. A*, 2003, **77**, 827–833.
[22] A. Hartmann, M. Neilson, R. Lamb, K. Watanabe and J. Scott, *Appl. Phys. A*, 2000, **70**, 239–242.
[23] C. R. Grovenor, *Microelectronic materials*, CRC Press, 1989.
[24] T. Fujii, M. Kawasaki, A. Sawa, Y. Kawazoe, H. Akoh and Y. Tokura, *Phys. Rev. B*, 2007, **75**, 165101.
[25] Y. Hikita, Y. Kozuka, T. Susaki, H. Takagi and H. Y. Hwang, *Appl. Phys. Lett.*, 2007, **90**, –.
[26] M. Minohara, I. Ohkubo, H. Kumigashira and M. Oshima, *Appl. Phys. Lett.*, 2007, **90**, –.
[27] C. R. Crowell, S. M. Sze and W. G. Spitzer, *Appl. Phys. Lett.*, 1964, **4**, 91–92.
[28] M. O. Aboelfotoh, A. Cros, B. G. Svensson and K. N. Tu, *Phys. Rev. B*, 1990, **41**, 9819–9827.
[29] M. Aboelfotoh, *Solid-State Electron.*, 1991, **34**, 51 – 55.
[30] J. Y. Duboz, P. A. Badoz, F. A. d'Avitaya and E. Rosencher, *Phys. Rev. B*, 1989, **40**, 10607–10610.
[31] J.-M. Albina, M. Mrovec, B. Meyer and C. Elsässer, *Phys. Rev. B*, 2007, **76**, 165103.
[32] J. Junquera, M. Zimmer, P. Ordejón and P. Ghosez, *Phys. Rev. B*, 2003, **67**, 155327.
[33] M. Peressi, N. Binggeli and A. Baldereschi, *J. Phys. D: Appl. Phys.*, 1998, **31**, 1273.
[34] P. W. Peacock and J. Robertson, *J. Appl. Phys.*, 2002, **92**, 4712–4721.

Chapter 8

Concluding remarks

The objective of this thesis was to investigate the behaviour of point defects in $SrRuO_3$ thin films deposited on single-crystal $SrTiO_3$. The means used to investigate the defect-chemistry and interface properties in the $SrRuO_3|SrTiO_3$ heterostructure was diffusion.

In the first part of this work, oxygen-tracer diffusion was thoroughly investigated in $SrRuO_3$ thin films. The oxyge- tracer diffusion coefficients obtained are among the lowest ever measured in perovskite oxides, which implies that oxygen vacancies are of minor importance in $SrRuO_3$. Despite the low concentration of oxygen vacancies, their behaviour indicates a surprisingly complex defect-chemistry of $SrRuO_3$ thin films. Here the postulation of a metastable defect structure was essential to understand the observed phenomena. Among these phenomena were the observation of Ti diffusion into the $SrRuO_3$ thin films as well as the formation of SrO precipitates at the sample surface. Here it is remarkable that both processes involve cation diffusion and occur at temperatures below $T < 1000\,\mathrm{K}$. It was concluded that these processes are a consequence of the metastable defect structure relaxing to thermodynamic equilibrium.

In the second part of this thesis, the metastable nature of the investigated thin films was further investigated. It was shown that the non-equilibrium state of $SrRuO_3$ thin films is an inherent feature of the sample preparation method pulsed laser deposition. By adjusting the kinetics of the pulsed laser deposition process, the nature of the metastable defect structure can be changed. This provides a unique chance for rapid prototyping of thin-film samples with different cation stoichiometry, namely different degrees of Ru deficiency. These variation in Ru deficiency are a consequence of the formation of volatile Ru species during the deposition process. The formation of these volatile species primarily depends on the adatom kinetics on the substrate surface, which and can be controlled by varying the deposition frequency. Variation of the deposition frequency thus allowed for systematically investigating the impact of Ru vacancies on the defect-chemistry of $SrRuO_3$. Here an increase in both the oxygen tracer diffusion and the oxygen surface exchange coefficient with increasing Ru deficiency was observed. Moreover the overall electrical conductivity, the Curie temperature as well as disorder induced phenomena systematically changed with the Ru deficiency.

In the third part of this work, theoretical considerations emphasising the importance of a time-dependent investigation of diffusion processes were presented. It was shown that only

a time-dependent investigation of the diffusion behaviour provides sufficient information to discriminate between diffusion through a space-charge layer present at a sample surface and coupled diffusion through a grain boundary and adjacent bulk material. In addition, the effects of space-charge layers around dislocations depleted of oxygen vacancies were theoretically investigated. The diffusion model derived from these considerations could be validated experimentally with diffusion data obtained on $SrRuO_3|SrTiO_3$ heterostructure samples. Here the focus was on the diffusion behaviour in the bulk of $SrTiO_3$.

With the knowledge gained on the diffusion processes in thin film $SrRuO_3$ as well as in bulk $SrTiO_3$, the focus of the fourth part of this study was directed towards an investigation of the $SrRuO_3|SrTiO_3$ interface. Oxygen-tracer diffusion profiles were used to indirectly determine the behaviour of the electric potential across the investigated interface. A temperature-dependent examination of the behaviour allowed for drawing conclusions about the electronic interface properties. The importance of interface states and differences caused by the defect chemistry of $SrTiO_3$ between high and low temperatures became apparent.

Finally I want to point out that thin-film heterostructures are ideally suited to investigate the defect chemistry of perovskite oxides. The possibility to deliberately adjust the defect state of the material by the controlling the preparation method paves the way for countless possibilities for defect-chemical investigations. Particularly the focus on the defect behaviour at interfaces of these thin-film structures will provide useful insights and help further developing the rapidly emerging field of all-oxide electronics.

List of Figures

List of Tables

Acknowledgements

First of all, I am indebted to Priv.-Doz. Dr. Roger A. De Souza for giving me the opportunity to work on this interesting and challenging topic. Discussions with him, his advise and encouragement were essential for obtaining the results presented and for shaping the final version of this thesis.

I want to thank Prof. Dr. Regina Dittmann for the fruitful collaboration and for allowing me to use the experimental infrastructure at the PGI-7, Forschungszentrum Jülich. I am indebted for her advice on film-growth topics and for always sharing her valuable perspective on the project.

Prof. Dr. Rüdiger-Albert Eichel and Prof. Dr. Ulrich Simon are gratefully acknowledged for reviewing this thesis.

Prof. Dr. Manfred Martin is gratefully acknowledged for accepting me as a member of his work group.

The experimental work conducted would not have been possible without help and support from technically highly qualified colleagues. Here I am deeply indebted to: The entire Ion-ToF Service team for their prompt help and their quick maintenance of the SIMS machine at all times; Thorsten Marioneck and Guido Kirf as representatives of the mechanical workshop as well Bernd Huppertz and his team from the elctronic workshop for their steady support; Dr. Paul Meuffels, René Borowski and Georg Pickartz for flawlessly maintaining the labs at the Forschungszentrum Jülich.

Parts of this thesis are a result of fruitful collaborations: Here I want to thank Prof. Dr. Andreas Klein (Technische Universität Darmstadt) for investigating the interface by means of XPS; Dr. Felix Gunkel (PGI-7, Forschungszentrum Jülich) for the temperature dependent conductivity measurements. I am also grateful to Christoph Bäumer (PGI-7, Forschungszentrum Jülich) for conducting various PEEM and XPS measurements and not loosing track of various different samples and their classification systems.

Furthermore I am deeply indebted to numerous (former) colleagues for introducing me into various experimental methods and helping me to improve my skills. Here I want to mention particularly Dr. Felix Gunkel and Dr. Anja Herpers for introducing me to all thin -film related technologies. I am particularly grateful to Markus Teusner for being my “SIMS-mate” for the past years. Working and discussing with him was always a great pleasure and helped me a great deal to increase the quality of measurements while loosing gratuitous fear of the instrument.

Thanks are due to all colleagues accepting the arduous task of proofreading parts of the manuscript: Amr Ramadan, Stefan Beschnitt and especially Annalena Schriever.

I am grateful to all my colleagues in both Aachen and Jülich for the great work atmosphere, their support and help was very valuable. Especially entertaining lunch and coffee breaks helped getting through the day sometimes.
If more distraction was necessary I could always count on friends from in- and outside of academia. Thank you for your support!

Lastly I want to thank my parents and my sister for their support and for cheering me up throughout my studies and the subsequent PhD time.